

Using Machine Learning to Discover Parsimonious and Physically-Interpretable Representations of Catchment-Scale Rainfall-Runoff Dynamics

Yuan-Heng Wang^{1,2} and Hoshin V. Gupta¹

¹Department of Hydrology and Atmospheric Science, The University of Arizona, Tucson, AZ

²Earth and Environmental Science Area, Lawrence Berkeley National Laboratory, Berkeley, CA

Contact: yhwang0730@gmail.com | hoshin@arizona.edu

Submitted to **arXiv**

Abstract

Despite the excellent real-world predictive performance of modern machine learning (ML) methods, many scientists remain hesitant to discard traditional physical-conceptual (PC) approaches due mainly to their relative interpretability, which contributes to credibility during decision-making. In this context, a currently underexplored aspect of ML is how to develop “*minimally-optimal*” representations that can facilitate better “*insight regarding system functioning*”. Regardless of how this is achieved, it is arguably true that parsimonious representations better support the advancement of scientific understanding. Our own view is that ML-based modeling of geoscientific systems should be based in the use of computational units that are fundamentally interpretable by design.

This paper continues our exploration of how the strengths of ML can be exploited in the service of better understanding via scientific investigation. Here, we use the Mass Conserving Perceptron (MCP) as the fundamental computational unit in a generic network architecture consisting of nodes arranged in series and parallel to explore several generic and important issues related to the use of observational data for constructing input-state-output models of dynamical systems. In the context of lumped catchment modeling, we show that physical interpretability and excellent predictive performance can both be achieved using a relatively parsimonious “*distributed-state*” multiple-flow-path network with context-dependent gating and “*information sharing*” across the nodes, suggesting that MCP-based modeling can play a significant role in application of ML to geoscientific investigation.

Plain Language Summary

Models must be interpretable to be credible during decision-making. Accordingly, excellent real-world predictive performance is not enough, due to which scientists remain hesitant to discard traditional physical-conceptual (PC) approaches in favor of purely data-based machine learning (ML) methods. Since parsimonious representations better support the advancement of scientific understanding, there is a need for methods that facilitate discovery of “*minimally*” representations that provide good predictive performance while also facilitating better “*insight regarding system functioning*”. We believe that such methods should be based in the use of computational units that are fundamentally interpretable by design. This work uses the Mass Conserving Perceptron (MCP) as the fundamental unit in a generic network architecture to explore several issues related to the development of dynamical systems models. For lumped catchment systems, we show that parsimonious and physically-interpretable models with excellent predictive performance can be achieved using a “*distributed-state*” multiple-flow-path representation with context-dependent gating and “*information sharing*” across the nodes. Our results suggest that MCP-based modeling can play a significant role in geoscientific investigation.

1. Introduction, Background and Scope

1.1. Introduction

[1] The system theoretic (so-called “*black box*”) approach to catchment-scale rainfall-runoff (RR) modeling can represent the dynamical behaviors of such systems without the need to incorporate prior knowledge regarding their internal form and functioning (*Bunge, 1963*). In fact, the Kolmogorov neural network existence theorem states that a three-layer feed-forward Artificial Neural Network (ANN) meets the requirements to be a universal function mapping, so that any multivariate function can be closely approximated by an ANN having only a finite number of nodes in the hidden layer (*Kolmogorov, 1957; Hecht-Nielsen, 1987*). In this regard, modern machine-learning (ML) provides a viable alternative to Physical/Conceptual (PC) modeling for simulating RR process, and can do this without explicitly representing the internal hydrologic structures of watersheds, while instead focusing primarily on achieving high predictive accuracy (*Sorooshian, 1983*).

[2] However, despite the excellent predictive performance of modern ML methods in real-world applications, many scientists remain hesitant to replace/discard traditional PC-based approaches due mainly to their relative *interpretability* (model transparency), which contributes to credibility during decision-making (*Rudin, 2019*). This issue has prompted recent research into “*explainable AI*” using methods such as Local Interpretable Model-Agnostic Explanations (LIME; *Althoff et al., 2021*), Shapley Additive Explanations (SHAP; *Yang & Chui 2021*), and the feature-importance-based Expected Gradient and Additive Decomposition method (*Jiang et al., 2022*). Meanwhile, Knowledge Guided Machine Learning (KGML; *Willard et al., 2022*) also provides a potential approach to enhanced interpretability (see detailed summary in *Varadharajan et al., 2022*) by transforming the “*black box*” models into “*glass (clear) box*” models (*Rai, 2020*), with the goal of achieving physically consistent and generalizable predictions at minimal model development cost.

[3] In this context, it is our opinion that a currently underexplored aspect is the investigation of “*minimally-optimal*” network architectures that can facilitate better “*insight regarding system functioning*”. This is in contrast to models that are based in poorly-interpretable computational units and generic architectures. One approach is to implement methods for network pruning/compression that can help to identify efficient low-rank sub-networks (*Schotthöfer et al., 2022; Zangrando et al., 2023*) thereby facilitating the quantification of information content (*Tishby & Zaslavsky, 2015; Shwartz-Ziv & Tishby, 2017*) and potentially enhancing the interpretability, and hence credibility, of ML-based approaches used for decision making. An alternative is to construct progressively more complex, but still architecturally generic, minimal description length representations until a satisfactory level of performance is achieved (*Stanley & Miikkulainen, 2002*). Our own view is that a more productive approach is to base the entire ML-based modeling approach in the use of computational units that are fundamentally interpretable by design (*Wang & Gupta, 2024a,b*). Regardless of which strategy is adopted, it is arguably true that parsimonious representations better support the advancement of scientific understanding (*Weijs & Ruddell, 2020*), based on which network architectures can be progressively augmented (as necessary and appropriate) during training (*Hsu et al., 1995; Chen & Chang, 2009*).

[4] This paper is third in a series that seeks to explore how the strengths of machine learning can be exploited in the service of achieving better understanding via scientific investigation. In Section 1.2, we provide some foundational background, after which we discuss the goals and scope of the studies reported here (Section 1.3), and the organization of this paper (Section 1.4).

1.2. Background

[5] There is a long history to the development of hydrologic models (see *Singh, 1988; Clark et al., 2008; Fenicia et al., 2011; Gupta et al., 2012*). In this regard, ANNs have been used for hydrologic prediction since at least the 1990’s (*Daniell, 1991; Halff et al., 1993; Hsu et al., 1995; Smith & Eli, 1995*) and have consistently been shown to outperform PC-based models as evaluated by a variety skill metrics (*Hsu et al., 1995*). Such

performance can be attributed to the fact that, whereas the architecture of a knowledge-based PC models must be pre-specified/defined to be consistent with physical principles/laws (such as mass and energy conservation), a data-driven model can “learn” an effective representation of the appropriate internal architectural features, via iterative adjustment/training of model weights so as to extract the relevant information from data (Xu & Liang, 2021).

[6] The past few years has seen extremely rapid development and application of machine/deep learning (ML/DL) artificial intelligence (AI) by the hydro-geo-scientific community (Shen, 2018). In particular, since its early application to RR modeling in the 1990’s (Hsu et al., 1995), the recurrent neural network (RNN) architecture has gained considerable attention and popularity. This is particularly true of the Long Short Term Memory network (LSTM; Hochreiter & Schmidhuber, 1997) which can learn to model the long-term dependencies that characterize storage effects such as snowpack accumulation and melt (Kratzert et al., 2018). In terms of predictive accuracy, as well as ability to provide predictions in ungauged basins, the standard LSTM formulation remains the “state-of-the-art” for catchment-scale RR modeling (Kratzert et al., 2019b), although the recently developed transformer neural network (TNN; Vaswani et al., 2007) also shows promise for hydrological applications (Li et al., 2022; Liu et al., 2024b; Koya & Roy, 2024).

[7] Notably, the LSTM-based approach has consistently been shown to outperform PC-based models for RR modeling (Kratzert et al., 2019a; Mai et al., 2022; Arsenault et al., 2023), and to be a viable surrogate for traditional data assimilation (Nearing et al., 2022), while enabling the leveraging of multiple sources of data regarding various meteorological variables (Kratzert et al., 2021) at multiple time scales (Gauch et al., 2021; Feng et al., 2020). Combined with time-efficient computation, these capabilities make LSTM-based modeling highly attractive for operational hydrologic forecasting (Harrigan et al., 2023; Sabzipour et al., 2023), especially at the global scale (Nearing et al., 2023; Kratzert et al., 2024).

[8] The exponential rate of development and widespread access to ML technology (and especially the power of differentiable programming; Baydin et al., 2018), has spawned considerable innovation in the development of modeling strategies and tools that combine physical principles with AI (Shen et al., 2023). One major research thread involves the use of data-driven methods for postprocessing the outputs of PC-based models (Nearing et al., 2020b; Frame et al., 2021). Post-processing is a relatively simple way to improve predictive accuracy in cases where the PC-based model encodes information provided by human knowledge that the ML algorithm is unable to extract from data.

[9] A second major thread aims to enhance model behavioral expressivity by adding functional complexity to the PC-based model (Jiang et al., 2020; Feng et al., 2022; Bennett & Nijssen, 2021). The model is improved by implementing operational neural network layers to learn improvements to the existing model parameterization (Tsai et al., 2021) or to provide substitutes for poorly understood process relationships (Höge et al., 2022; Feng et al., 2023).

[10] A third major thread involves (partially) modifying the internal neural network architecture (Nourani, 2021) for the purpose of improving the regionalization ability of the model (e.g., EA-LSTM; Kratzert et al., 2019b). This approach encodes physical principles such as mass conservation (MC-LSTM; Hoedt et al., 2021; Frame et al., 2022), together with regularization to constrain (for example) evapotranspiration loss (Wi & Steinschneider, 2024), or to add an attention mechanism that helps to identify important catchment specific features (e.g., Hydro-LSTM; De la Fuente et al., 2024a). Overall, such investigations have enlivened the community and contributed to rapid advances in the Earth, Environmental, and Geosciences (Fleming et al., 2021).

1.3. Goals and Scope

[11] This study builds upon our previous work reported in Wang & Gupta (2024a,b). In the first (Wang & Gupta, 2024a) we proposed a physically-interpretable computational unit (named the *Mass Conserving Perceptron*) to be used as a component (node) in neural networks that can directly learn the functional nature of physical processes from available data (as in machine “learning”) using off-the-shelf ML technologies, while being

regularized to obey conservation principles at the nodal level. The purpose was to explore the behavioral expressivity, interpretability, and performance achievable by a single MCP node (a single cell-state model) enabled by the learnable gating mechanism, and where all of the architectural complexity was expressed only through those gating functions. In particular, we demonstrated how prior knowledge and/or hypotheses regarding system dynamics can be progressively encoded into a simple MCP-based single-node model, thereby enabling the scientist to test different hypothesis regarding the internal functioning of the catchment ([Gong et al., 2013](#); [Nearing et al., 2020a](#)).

[12] Next, in [Wang & Gupta \(2024b\)](#) we showed that the MCP can be used as a building block for constructing more complex, but parsimonious, directed graph architectures consisting of node (state variable) and link (flow path) subcomponents ([Gupta & Nearing, 2014](#)), that obey conservation principles and are conceptually-interpretable in the traditional PC sense, while achieving comparable performance to purely data-based models. The purpose was to show how ML can be used to effectively combine theory-based prior information with novel information extracted from data, thereby enabling hypotheses testing regarding appropriate system architecture (numbers of dynamical state variables and their interconnectedness) and an examination of how information is increased, decreased, or altered during stagewise model development ([Fenicia et al., 2008](#); [Kavetski & Fenicia, 2011](#); [Nearing & Gupta, 2015](#); [Gharari et al., 2021](#)).

[13] In this work, we seek to explore a number of generic and important issues related to the use of time series data for the construction of dynamical input-state-output models. Accordingly, instead of using physical-conceptual principles and/or theory to guide specification of the form of the directed graph network architecture, wherein the nodes (cell states) and links (pathways) are pre-emptively assigned conceptual meaning at the time of model specification based on physical-conceptual understanding/theory (e.g., as was done in [Wang & Gupta, 2024b](#)), we follow the function approximation paradigm employed by modern ML wherein a generic network architecture is implemented consisting of “*basis function nodes*” arranged in series and parallel. By using the MCP node as the fundamental computational unit, we are able to explore (in the context of a lumped catchment system) several generic and important modeling issues such as:

- 1) How many network “*layers*”, “*nodes*” (cell-states) and “*links*” (flow pathways) are potentially necessary/sufficient to accurately model the input-state-output dynamics of a given system?
- 2) Is a “*distributed-input*” or a “*distributed-state*” representation (or some hybrid combination of the two) a more suitable approach to network regularization?
- 3) Consistent with physical understanding that water balance closure at the overall catchment-scale is typically impossible to assert with any degree of confidence, is there potential benefit to relaxing mass conservation at the overall “*network*” level while maintaining mass-conservation at the “*nodal*” level?
- 4) Is there benefit to allowing the nodal “*gates*” to be informed about the entire distribution of “*moisture*” across the system when determining what the time-varying (context-dependent) output and loss gate conductivities should be at each time step?
- 5) How much interpretability can be achieved/maintained by such a network while permitting it to pursue the aim of optimal predictive performance?
- 6) How does such predictive performance compare to that obtained using “*purely data-based*” and/or conventional “*physical-conceptual*” models?
- 7) Are there potential benefits to “*training*” and then “*pruning*” such MCP-based machine-learning networks?

[14] To our knowledge, no similar efforts have been made in this regard. While generic RNN-based networks ([Nearing et al., 2021](#); [Kratzert et al., 2024](#)) are capable of very high levels of predictive performance, we follow Occam’s Second Razor ([Domingos, 1998](#)) in suggesting that it is sensible to “*think twice*” before abandoning interpretability in favor of non-understandable complexity. As with our previous work ([Wang & Gupta,](#)

2024a,b), our scope here remains restricted to an examination of interpretable architectural complexity at a single location, rather than universal applicability across large samples of catchments. Combined with our previous findings, the results reported here form the necessary pre-requisite for broader application to multiple hydro-climatic regimes (work in progress), and to eventually tackling the problem of interpretable ML-based modeling for prediction in ungauged basins (PUB; *Sivapalan et al., 2003; Hrachowitz et al., 2013*).

1.4. Organization of the paper

[15] In Section 2 we briefly recap relevant details regarding the physically-interpretable Mass-Conserving Perceptron and its analogical relationship to the fundamental computational component of the data-based LSTM network. Section 3 outlines the data, methods, and MCP-based network architectures explored in this study, and discusses the “overall interpretability” associated with such network architectures. Sections 4 and 5 discuss our findings and results. In particular Section 5 explores the value of “information sharing” across nodes of the network, a feature that is built-in to the standard LSTM architecture but is not commonly found in PC-based representations of geoscientific (e.g., hydrological) systems. Section 6 presents a benchmark comparison against both MCP-based models introduced in *Wang & Gupta (2024b)* and the standard LSTM networks, while Section 7 illustrates the interpretability of MCP-based neural networks. Finally, in Section 8, we conclude with a discussion of implications and directions for future work.

2. Methodology

2.1 The Mass-Conserving Perceptron (MCP)

[16] In *Wang & Gupta (2024a)*, we proposed the mass-conserving perceptron (MCP) as an ML-based physically-interpretable computational unit that is isomorphically similar to a single node of a generic gated recurrent neural network, but is different in that it enables mass flows to be conserved at the nodal level. *Figure 1b* illustrates the architecture of the MCP node. The node represents mass-conservative system dynamics via the discrete time update equation:

$$X_{t+1} = X_t - O_t - L_t + U_t \quad (1)$$

whereby the mass state X_{t+1} of the system (node) at time step $t + 1$ is computed by adding the mass of input flux U_t that enters the node, and subtracting the masses of output fluxes O_t and L_t that leave the node, during the time interval from t to $t + 1$. For example, in the context of spatially-lumped catchment-scale RR modeling, U_t can represent the precipitation mass input flux, and L_t and O_t can represent the evapotranspirative and streamflow mass output fluxes from the system control volume represented by the node.

[17] It is assumed that O_t and L_t depend on the value of the state X_t through the process parameterization equations $O_t = G_t^O \cdot X_t$ and $L_t = G_t^L \cdot X_t$, where G_t^O and G_t^L are context-dependent (see later) time-varying “output” and “loss” conductivity gating functions respectively, so that Eqn (1) can be rewritten as:

$$X_{t+1} = X_t - G_t^O \cdot X_t - G_t^L \cdot X_t + U_t \quad (2a)$$

$$X_{t+1} = G_t^R \cdot X_t + U_t \quad (2b)$$

where G_t^R is the “remember” gate, represents the fraction of the state X_t that is retained by the system from one time step to the next. To ensure physical realism, we require that the time-evolving values of each of these gates (G_t^O , G_t^L and G_t^R) remain both non-negative and less than or equal to 1.0 at all times. Further, to ensure conservation of mass we require that $G_t^R + G_t^O + G_t^L = 1$, which means that the remember gate is computed from knowledge of the output and loss gates as $G_t^R = 1 - G_t^O - G_t^L$; this of course places a strict constraint on the relative values that G_t^O and G_t^L can take on. Now, assuming knowledge of the initial mass state of the system X_0 , and given the time history of inputs U_1, \dots, U_t , Eqn (2) can be used to sequentially update the state X_t of the system if the time-evolving values of the gating functions G_t^O and G_t^L (and therefore G_t^R) are also provided.

[18] Given this nodal architecture, it is clear that the time evolving nature of the gating functions G_t^O and G_t^L determines the dynamical response of the system to inputs. Since the precise forms of these gating functions are, in general, not known a priori, [Wang & Gupta \(2024a\)](#) proposed to parameterize these functions using machine learning (ML) architectures so that their functional forms can be learned directly from available data. In this study, we begin by parameterizing the output and loss gates as $G_t^O = f_{ML}^O(X_t)$ and $G_t^L = f_{ML}^L(PE_t)$ respectively, where $f_{ML}^O(\cdot)$ and $f_{ML}^L(\cdot)$ are implemented as ML architectures that can ‘learn’ the functional forms of the dependence of G_t^O on the system state X_t and the dependence of G_t^L on potential evapotranspiration PE_t . For simplicity, we assume here that these functional forms are simple monotonic non-decreasing sigmoid functions. However more complex functional forms can also be learned, as discussed by [Wang & Gupta \(2024a\)](#).

[19] Specifically, the output and loss gates are initially represented as $G_t^O = \kappa_O \cdot \sigma(S_t^O)$ and $G_t^L = \kappa_L \cdot \sigma(S_t^L)$ respectively, where $S_t^O = a_O + b_O X_t$ and $S_t^L = a_L + b_L PE_t$, and where σ can be any appropriate ML activation function (here chosen to be the sigmoid activation function $\sigma(S) = 1/(1 + \exp(-S))$), and $\kappa_O, a_O, b_O, \kappa_L, a_L,$ and b_L are trainable parameters. Further, to ensure that G_t^O, G_t^L and G_t^R each remain on $[0,1]$ and also that $G_t^O + G_t^L + G_t^R = 1$, we actually set $\kappa_O = \exp(c_O)/\Psi$ and $\kappa_L = \exp(c_L)/\Psi$ where $\Psi = \exp(c_O) + \exp(c_L) + \exp(c_R)$ (which is equivalent to implementing the *SoftMax* function on the gates) and instead train on the set of seven parameters $\{a_O, b_O, c_O, a_L, b_L, c_L, c_R\}$ all of which can vary on $(-\infty, +\infty)$. Further, we constrain the computed (“actual”) evapotranspirative loss ($L_t = G_t^L \cdot X_t$) to be less than or equal to the “potential” evapotranspirative loss D_t by replacing the “unconstrained” loss gate G_t^L described above with the “physically-constrained” loss gate defined as $G_t^{L^{con}} = G_t^L - \text{ReLU}(G_t^L - \frac{D_t}{X_t})$. For more details, please see [Wang & Gupta \(2024a\)](#).

[20] Overall, this basic MCP unit has several desirable features that make it suitable for interpretable physical-conceptual modeling of dynamical systems such as are of interest in hydrology (i.e., rainfall-runoff modeling). These features include:

- 1) Recurrence, enabling the dynamical evolution of the system state (memory) to be represented.
- 2) The ability to impose conservation principles at the nodal level, as constraints on system evolution.
- 3) The ability to represent and learn the dynamics of unobserved gains/losses of mass from the system.
- 4) The ability to learn the forms of the process parameterization equations (gating functions) that govern the dynamical behaviors of the system based on context (current and past conditions).
- 5) Ease of implementation using off-the-shelf ML technology such as PyTorch in Python ([Paszke et al., 2019](#)).

[21] In summary, we use the MCP node ([Figure 1](#)) as the basic unit for building the various interpretable neural networks discussed in this study.

2.2 Long Short-Term Memory Network (LSTM)

[22] As a data-driven benchmark to evaluate performance of the MCP-based networks tested in this study ([Nearing et al, 2020](#)) we use the LSTM network, adapted from code provided by [Kratzert et al. \(2019\)](#). The LSTM network is a type of recurrent neural network that includes memory cells that can store information over long periods of time, and that uses three gating operations (input, forget, output) as shown in [Figure 1c](#). The mathematical formulation of the LSTM network is provided in the supplementary materials.

[23] Given an input sequence $x = [x[1], x[2] \dots \dots, x[T]]$ with T time steps, where each element $x[t]$ is a vector containing input features (model inputs) at time step t ($1 \leq t \leq T$), Eqns (3-8) specify a single forward pass through the LSTM:

$$i[t] = \sigma(b_i x[t] + w_i h[t-1] + a_i) \quad (3)$$

$$f[t] = \sigma(b_f x[t] + w_f h[t-1] + a_f) \quad (4)$$

$$g[t] = \tanh(b_g x[t] + w_g h[t-1] + a_g) \quad (5)$$

$$o[t] = \sigma(b_o x[t] + w_o h[t-1] + a_o) \quad (6)$$

$$c[t] = f[t] \odot c[t-1] + i[t] \odot g[t] \quad (7)$$

$$h[t] = o[t] \odot \tanh(c[t]) \quad (8)$$

where $i(t)$, $f(t)$, $o(t)$ are the input, forget and output gates respectively, $g(t)$ is the cell input, $x(t)$ is the network input at time step t ($1 \leq t \leq T$), and $h(t-1)$ is the recurrent input. The terms $c(t)$ and $c(t-1)$ indicate the cell states at the current and previous time step. At the first-time step, the hidden and cell states are initialized as vectors of zeros. The terms a , w and b are learnable parameters for each gate, with subscripts referring to which gate the particular weight matrix, or bias vector corresponds to. The sigmoid activation function $\sigma(\cdot)$ outputs a value between 0 and 1, while the hyperbolic tangent activation function $\tanh(\cdot)$ outputs a value between -1 and 1. The symbol \odot indicates element-wise multiplication.

[24] The values of the cell states can be modified by the forget gate $f(t)$, which can delete states. The cell update $g(t)$ can be interpreted as information that is added, while the input gate $i(t)$ controls into which cells new information is added. The output gate $o(t)$ controls which of the information, stored in the cell states, is output. Note that the cell states $c(t)$ characterize the memory of the system, and its simple linear interaction with the remaining LSTM cell helps to prevent the issue of exploding or vanishing gradients during the back-propagation step of network training (Hochreiter & Schmidhuber, 1997). The output of the final LSTM layer $h(t)$ is connected through a dense layer to a single output neuron, which computes the final output $y(t)$ prediction, as indicated by Eqn 9:

$$y = b_d h_n + a_d \quad (9)$$

where b_d and a_d are learnable weights and bias terms of a dense output layer.

2.3 Isomorphic Relationship Between Architectures

[25] As discussed above (Section 2.1), the MCP unit is structurally isomorphic to the representation of a simple physical RR system expressed as an RNN. Eqns (10-16) show how the MCP unit is isomorphically similar to that of the LSTM:

$$i(t) = G_t^U = 1.0 \quad (10)$$

$$f(t) = G_t^R = 1.0 - G_t^O - G_t^L \quad (11)$$

$$g(t) = U_t \quad (12)$$

$$o(t) = G_t^O = \kappa_o \odot \sigma(b_o c(t) + a_o) \quad (13)$$

$$l(t) = G_t^L = \kappa_L \odot \sigma(b_L PET_t + a_L) \quad (14)$$

$$c(t+1) = X_{t+1} = f(t) \odot X_t + i(t) \odot g(t) \quad (15)$$

$$O(t) = o(t) \odot X_t \quad (16)$$

[26] Note that whereas the input gate $i(t) = G_t^U$ (Eq 10) is set to 1.0, thereby indicating that all of the input mass enters the cell state, one can also create a “bypass” gate by defining $G_t^B = 1 - G_t^U$ that allows some quantity of the input mass to bypass the unit. The LSTM forget gate $f(t)$ is re-interpreted (Eqn 11) as a “remember gate” G_t^R since its value (which varies between 0 and 1) indicates the extent to which the system retains water at each time step. Accordingly, the cell update $g(t)$ is equal to the mass input U_t to the unit at any given time (Eqn 12). The output gate $o(t) = G_t^O$, and the newly proposed loss gate $l(t) = G_t^L$, are simply parameterized here as being dependent on the current timestep cell state and potential evapotranspiration respectively (Eqns 13-14); more complex dependencies could also be envisioned and implemented. The mass output $O(t)$ is computed as a fraction $o(t) = G_t^O$ of the current timestep internal state X_t (Eq 16). Finally, the cell state $c(t+1) = X_{t+1}$ is updated to represent how much of the mass is retained by the unit, and

augmented by the incoming input mass at the current time step (Eq 15). As such, given the constraints imposed on the values of its gating functions ($G_t^R + G_t^O + G_t^L = 1$ and $0 \leq G_t^O, G_t^L, G_t^R \leq 1$), each node of an MCP-based network can be understood to function like a mass-constrained version of a node of an LSTM network.

[27] It is important to note that, compared to the Nash linear reservoir tank (*Nash, 1957*), the MCP can be viewed as a non-linear reservoir with evapotranspirative loss, where the time-constant conductivity parameter is replaced by a time-variable gating function. In this context, the mathematical structure of the simple mass-balance linear reservoir model is isomorphically similar to the MCP (and by extension, LSTM), with adjustments to the remember gate (Eq 17) and output gate (Eq 18), and by removing the loss gate. These relationships are clearly illustrated in *Figure 1a*.

$$\begin{aligned} f(t) &= G_t^R = 1.0 - G_t^O & (17) \\ o(t) &= G_t^O = \kappa_o & (18) \end{aligned}$$

3. Experimental Setup

3.1 Study Catchment and Data Set

[28] All of the experiments reported in this study use the Leaf River data set (compiled by the US National Weather Service), consisting of 40 years (WY 1949-1988) of daily data from the humid, 1944 km², Leaf River Basin (LRB) located near Collins in southern Mississippi, USA. The dataset consists of cumulative daily values of observed mean areal precipitation (*PP*; mm/day), potential evapotranspiration (*PET*; mm/day), and watershed outlet streamflow (*QQ*; mm/day). The dataset has been widely used for model development and testing by the hydrological science community.

3.2 Data Splitting

[29] As discussed by *Shen et al. (2022)*, it is important to use only a portion of the available data \mathcal{D} for making decisions about the model representation (choices regarding model structure and parameter values), while retaining a separate portion for testing the validity of those choices. Here, we follow the data-splitting procedure reported in *Wang & Gupta (2024a)* and adopt the robust data allocation method developed by (*Zheng et al., 2022*) that partitions the data (\mathcal{D}) to ensure distributional consistency of the observational streamflow records across three subsets of the data to be used for *training* (\mathcal{D}_{train}), *selection* (\mathcal{D}_{select}), and *testing* (\mathcal{D}_{test}). This contributes to ensuring that model performance is relatively consistent across each of three independent sets (*Chen et al., 2022; Maier et al., 2023*), and enables us to reasonably neglect the need for procedures such as k-fold cross validation.

[30] For all experiments, we set the $\mathcal{D}_{train} : \mathcal{D}_{select} : \mathcal{D}_{test}$ partitioning ratio to be 2:1:1 respectively. The data splitting procedure first sorts the streamflow data based on magnitude. Next, the timestep associated with the largest streamflow magnitude is paired with the timestep associated with the smallest streamflow value, continuing with the next largest and smallest values and so on, until all time steps have been paired. These pairs are then sequentially allocated, in the abovementioned ratio, to the three independent sets (following the sequence of $\mathcal{D}_{train} \rightarrow \mathcal{D}_{test} \rightarrow \mathcal{D}_{select} \rightarrow \mathcal{D}_{train}$ etc.) until all pairs have been assigned. Overall, given 14,610 time-steps/days in the 40-year LRB dataset, this results in a training subset consisting of 7,306 timesteps, and selection and testing subsets consisting of 3,652 time-steps each.

3.3 Metrics Used for Training and Performance Assessment

[31] The metric used for model training was the *Kling-Gupta Efficiency* (*KGE*; Eqn. 19) (*Gupta et al., 2009*). As in *Wang & Gupta (2024a,b)*, each model architecture was trained 10 times with random initialization of the parameters, from which the one having the highest scaled *KGE* score (KGE_{ss} ; Eqn. 20) (*Knoben et al., 2019*) computed on the *selection* set was retained. Performance assessment was conducted using KGE_{ss} and the components of *KGE* (Eqns 21-23):

$$KGE = 1 - \sqrt{((\rho^{KGE} - 1)^2 + (\beta^{KGE} - 1)^2 + (\alpha^{KGE} - 1)^2)} \quad (19)$$

$$KGE_{ss} = 1 - \frac{(1-KGE)}{\sqrt{2}} \quad (20)$$

$$\alpha^{KGE} = \frac{\sigma_s}{\sigma_o} \quad (21)$$

$$\beta^{KGE} = \frac{\mu_s}{\mu_o} \quad (22)$$

$$\rho^{KGE} = \frac{Cov_{so}}{\sigma_s \sigma_o} \quad (23)$$

where σ_s and σ_o are the standard deviations, and μ_s and μ_o are the means, of the corresponding data-period simulated and observed streamflow hydrographs respectively and, similarly, Cov_{so} is the covariance between the simulated and observed values. Note that KGE (and therefore KGE_{ss}) is maximized when α^{KGE} , β^{KGE} and ρ^{KGE} are all 1.0.

[32] Although α^{KGE} and β^{KGE} are both optimal at 1.0, their values can be larger or smaller than this optimal value which lead to ambiguity when conducting model comparisons using these metrics. Here, we define α_*^{KGE} and β_*^{KGE} as shown in Eqns (24-25) to circumvent this problem through allowing 1.0 to be upper bound value.

$$\alpha_*^{KGE} = 1 - |1 - \alpha^{KGE}| \quad (24)$$

$$\beta_*^{KGE} = 1 - |1 - \beta^{KGE}| \quad (25)$$

3.4 Training Procedures, Algorithm and Hyperparameter Selection

[33] The training procedures were also adopted from [Wang & Gupta \(2024a,b\)](#). To initialize the model cell-states, we used a “three-year” spin-up period that sequentially repeats the first water year data (WY 1949) three times at the start of the overall 40-year simulation period. This helps to minimize the potential effects of state initialization errors ([De la Fuente et al., 2023](#)). The gradient-based ADAM optimization algorithm ([Kingma & Ba, 2014](#)) was used for model training (i.e., to determine optimal values for the parameters of the gating functions). The training metric and its gradient were computed using the streamflow values/timesteps assigned to the training subset.

3.5 Basic Network Architectures Tested

[34] [Wang & Gupta \(2024a\)](#) explored the expressive power of a single MCP node (cell-state) while enabling the gating operations to be represented with various levels of functional complexity. We showed that the basic mass-conserving node, represented as $MC\{O_\sigma L_\sigma^{con}\}$, is able to provide the bare minimum amount of complexity/flexibility required to achieve good predictive accuracy while also being physically-interpretable. This unit uses simple sigmoid activation functions (indicated by subscript σ) for the construction of the output and loss gates (O_σ and L_σ respectively), while constraining (indicated by superscript *con*) the evapotranspirative loss flux to be less than or equal to PET.

[35] Subsequently, [Wang & Gupta \(2024b\)](#) showed how the MCP unit can be used as a basic building block for constructing and testing a variety of multi-node (multi-cell-state) conceptually-interpretable representational hypotheses (architectures) for the spatially-lumped catchment-scale Leaf River system. As in [Wang & Gupta \(2024a\)](#), the models were constructed and trained using readily-available ML technologies.

[36] Here, we explore the predictive performance achievable by use of basic MCP units as the building blocks of “interpretable neural networks” (INN), where the network architectures consist of layers of fully-connected “nodes” as is common, for example, when building LSTM models, and where the main hyperparameters to be tuned are the numbers of layers and the numbers of nodes in each layer. To achieve additional expressive power, we modified the loss gate L_σ^{con} so that (in addition to PET) it is also informed by the value of the cell-state, and refer to this unit using the notation $MC\{O_\sigma L_{\sigma+}^{con}\}$, where the additional + symbol indicates this augmentation. Hereafter, unless otherwise mentioned, all nodes in the MCP-based networks are of the

augmented $MC\{O_\sigma L_{\sigma+}^{con}\}$ type. In Section 4, we show that this modification results in a significant performance improvement.

[37] To describe the resulting MCP-based fully-connected network architectures, we will use ℓ to refer to the “layer number” (where $\ell = 1$ indicates the hidden layer closest to the system inputs) and use N_ℓ to refer to the number of (augmented) MCP nodes in hidden layer ℓ . All nodes in layer ℓ are fully-connected to the nodes in the previous layer ($\ell - 1$) in the sense that they receive inputs from all of those nodes, except for the first layer which is only connected to the system inputs. To refer to such architectures we will use the notation $MN(N_1, N_2, \dots)$ so that $MN(3)$ indicates a single-layer network consisting of 3 MCP nodes, while $MN\{3,3,2\}$ indicates a three-layer network consisting of 3 nodes in each of the first and second layers and 2 nodes in the third layer. Clearly, therefore, $MN(1) \equiv MC\{O_\sigma L_{\sigma+}^{con}\}$.

[38] Further, whenever the first hidden layer has more than one node, we need to incorporate a mechanism for distributing/allocating the system inputs (here, the incoming precipitation) across the nodes of the layer. Similarly, we need a mechanism for aggregating the system outputs from the final layer to obtain the prediction of the system output (here, streamflow). To identify these different mechanisms, we will use the notation $MN^{NType}(N_1, N_2, \dots)$ where superscript *NType* indicates the network type (based on the type of input distribution and output aggregation mechanism used), as explained below.

[39] Overall, we consider five types of networks (see [Figure 2](#)) as described below – (i) Distributed-Input, (ii) Distributed-State, (iii) Distributed-Input Relaxed, (iv) Distributed-State Relaxed, and (v) ML Benchmark.

3.5.1 Distributed-Input (DI) Network

[40] We use the notation $MN^{DI}(\dots)$ to indicate a network where the input distribution weights w_j^{in} are constrained to all be positive and sum to one (i.e., $\sum_j w_j^{in} = 1, w_j^{in} \geq 0$ for all j), while the output aggregation weights are all identically equal to one (i.e., $w_k^{out} = 1$ for all k).

[41] This architecture can be interpreted as allocating the total system input (here precipitation) in different fractions along different flow paths. For example, we might imagine that different fractions of the rain fall on impermeable ground, grassland, and forested portions of the catchment. Accordingly, the nodal cell-states in the first layer represent different degrees of surface “wetness” or “moisture storage” associated with each of these fractional portions. By setting all the output weights to equal one, we simply aggregate together the outputs (flow components) generated by each flow path. Overall, this network type ensures mass conservation at both the individual nodal level and the overall network level.

3.5.2 Distributed-State (DS) Network

[42] The notation $MN^{DS}(\dots)$ indicates a network where the input distribution weights w_j^{in} are set to all be identically equal to one (i.e., $w_j^{in} = 1$ for all j), while the output aggregation weights are constrained to be positive and sum to one (i.e., $\sum_k w_k^{out} = 1, w_k^{out} \geq 0$ for all k).

[43] This can be interpreted as a crude way of modeling the system in a probabilistic manner, where the “lumped overall average” (single statistic) value of surface “moisture” is inadequate to describe the “state” of the system and instead a “distributional description” is required to better represent the dynamics of the system. This concept is analogous to that encoded by the Probability Distributed Store component ([Moore, 2007](#)) used in versions of the HyMod and other conceptual hydrological models ([Liang et al., 1994](#); [Boyle et al., 2000](#)). By passing the same (total) amount of precipitation to each node of the first layer, a discrete distribution of different magnitudes of surface “moisture” states can be simulated. However, unlike the PDM, the network gives rises to a discrete distribution of “flow” magnitudes leaving those nodes, for further processing by subsequent layers. By setting the output aggregation weights to be positive and sum to one, we again ensure mass conservation at the overall network level.

3.5.3 Distributed-Input-Relaxed (DIR) Network

[44] The notation $MN^{DIR}(\dots)$ indicates a network similar to the DI type, but where the input distribution weights w_j^{in} are not constrained to sum to one, while still being required to be positive (i.e., $\sum_j w_j^{in} \neq 1$, $w_j^{in} \geq 0$ for all j).

[45] This can be interpreted as allowing for “bias” correction of the magnitude of incoming precipitation, thereby relaxing the requirement for mass conservation at the overall network level.

3.5.4 Distributed-State-Relaxed (DSR) Network

[46] The notation $MN^{DSR}(\dots)$ indicates a network similar to the DS type, but where the output aggregation weights w_k^{out} are not constrained to sum to one, while still being required to be positive (i.e., $\sum_k w_k^{out} \neq 1$, $w_k^{out} \geq 0$ for all k).

[47] This can be interpreted as allowing for “bias” correction of the magnitude of outgoing flow, thereby relaxing the requirement for mass conservation at the overall network level.

3.5.5 ML-Benchmark (MLB) Network

[48] Finally, the notation $MN^{MLB}(\dots)$ indicates a network where neither the input distribution weights w_j^{in} or the output aggregation weights w_k^{out} are constrained to sum up to one, but are only required to be positive (i.e., $\sum_j w_j^{in} \neq 1$, $w_j^{in} \geq 0$ for all j and $\sum_k w_k^{out} \neq 1$, $w_k^{out} \geq 0$ for all k). In addition, learnable bias weights w_{0j}^{in} are included at the input distribution level (so that the input u_j to node j of the first hidden layer is given by $u_j = w_j^{in} \cdot u + w_{0j}^{in}$ where u is the system input) and a learnable bias weight w_0^{out} is included at the output aggregation level (so that the system output o is given by $o = w_k^{out} \cdot o_k + w_0^{out}$).

[49] This can be interpreted as a network where conservation still occurs at each node, but where the requirement for mass conservation is completely relaxed at the overall network-level.

3.6 Additional Network Architectures Tested

[50] In addition to these five network types, we also explored variations in the kinds of information that are provided to the output and loss gates (O_σ and L_σ respectively). Recall that the aforementioned MCP-based architectures are designed such that the output gate $G_t^O = f_{ML}^O(X_t)$ and loss gate $G_t^L = f_{ML}^L(PE_t, X_t)$ of any node in the network have access to only information regarding the magnitude of the cell-state X_t of that same node, and not to the magnitudes of the cell-states of other nodes in the network. This property was maintained when designing and testing the various multi-node “conceptual” architectural hypotheses tested in [Wang & Gupta \(2024b\)](#).

[51] In contrast, the LSTM architecture typically provides the gating functions at each node with access to the cell-state magnitudes of all of the nodes in the same layer. We will refer to such a situation as the “sharing” of cell-state information across nodes of a hidden layer. We therefore also considered the following four types of *cell-state-information-sharing* in our MCP-based networks, to assess their relative value in determining performance of the five network types discussed above.

- a) **No Sharing (Sharing type “None”):** Notation $MN_{None}^{NType}(\dots)$ is used to indicate that the output and loss gates at each node are not provided with access to the cell-state-magnitudes of other nodes.
- b) **Sharing-Augmented Loss Gates (Sharing type “SAL”):** Notation $MN_{SAL}^{NType}(\dots)$ is used to indicate that the loss gates at each node in a layer are provided with access to the cell-state-magnitudes of other nodes in that layer (and potential evapotranspiration), while each output gate is only given access to the magnitude of its own cell-state.
- c) **Sharing-Augmented Output Gates (Sharing type “SAO”):** Notation $MN_{SAO}^{NType}(\dots)$ is used to indicate that the output gates at each node in a layer are provided with access to the cell-state-magnitudes of

other nodes in that layer, while each loss gate is only given access to the magnitude of its own cell-state (and potential evapotranspiration).

- d) **Sharing-Augmented Loss & Output Gates (Sharing type “SALO”)**: Notation $MN_{SALO}^{NType}(\dots)$ is used to indicate that *both* the loss and output gates at each node in a layer are provided with access to the cell-state-magnitudes of other nodes in that layer.

[52] Accordingly, with five network types and four information-sharing types, we have a total of $5 \times 4 = 20$ MCP-based network cases that will be tested. In all cases, the weights associated with contextual information accessible by the gates are permitted to be either positive or negative and will typically be close to zero, where a zero value means that the associated information is not being used (is not useful) to determine the value of the gate-state.

3.7 Comments about Information Flows and Network Training

[53] Note, importantly, that in all of these cases (listed in [Table 1](#)), while the networks are fed with the *same* area-averaged catchment precipitation as input, they differ in: (i) the manner by which that “input mass” is routed through the system, and (ii) the manner by which “information” flows between the gating components of that system.

[54] For training the single hidden layer MCP networks, we initialized all nodes to the same parameter (weight) values that were obtained for the single node MCP architecture ($MC\{O_{\sigma}L_{\sigma}^{con}\}$) and then added different levels of Gaussian random noise to all of the weights. In other words, the trained parameters of the single node architecture were treated as “mean” values, and the magnitude (standard deviation) of the noise was chosen to be between 2.5% and 20% of that mean value (the actual percentage was selected based on how significantly the gating functions changed when altering the associated parameters). Further, for the cases with information sharing, the $N_{\ell} \times 1$ vectors of weights associated with the output or loss gates become $N_{\ell} \times N_{\ell}$ matrices, where the diagonal values control information provided by the same node. Accordingly, following the same initialization rule mentioned above, the off-diagonal values were randomly initialized with a zero mean and 0.025 standard deviation (very close to zero). We found that this training approach converges more efficiently than a stagewise approach.

[55] However, the approach did not perform well for training the multi-layer networks, likely because the hidden layer nodes function more as “routing” tanks than as “soil-moisture storage” tanks, leading to incorrect parameter initialization. Therefore, we instead followed the [Wang & Gupta \(2024a,b\)](#) approach and progressively increased the numbers of nodes in a stagewise manner (on top of the trained single layer network) so that only the weights associated with “newly added” nodes were initialized to random values (between -1 to 1), while the weights associated with previously trained nodes were initialized to their optimal values previously obtained.

[56] Each network architecture was trained 10 times, from different random initializations of the weights, for 1000 to 3000 epochs using KGE as the objective function. Results are reported for the model that obtained the highest selection-period KGE_{ss} . See supplementary materials for a detailed summary of the performance of single-layer cases ([Table S1-S7](#)).

4. Results for MCP-Based Architectures without Information Sharing

4.1 The Baseline Single-Layer MCP-Based Architectures

[57] To begin, we restrict our attention to the five basic single-hidden-layer network architectures – distributed input (DI), distribute state (DS), distributed input relaxed (DIR), distribute state relaxed (DSR), and machine learning benchmark (MLB), described in Section 3.5 – where information-sharing between nodes is not permitted, and network complexity is varied by progressively increasing the number N_1 of nodes in the layer. Of these, the first two (DI and DS) conserve mass at both nodal and network level, while the latter three (DIR ,

DSR, and MLB) conserve mass only at the nodal level. We varied N_1 from 1 to 5. Results are presented in **Figures 3a-f** as distributions (over forty-years) of annual KGE_{ss} performance.

[58] The leftmost sub-plot (**Figure 3a**) shows results for the original (dark grey) and augmented (blue) versions of a single MCP node. Recall that the loss gate of the augmented version \underline{I}_s provided with access to magnitude of the cell-state whereas the original is not. Overall (distributional) performance of the augmented node is clearly superior to that of the original. Although median year performance improves only slightly, the interquartile range is significantly reduced, mainly due to performance improvements in the lower-quantile (drier) years. Further, KGE_{ss} performance for the worst (driest) year improves dramatically from $0.3 \rightarrow 0.57$. Accordingly, all subsequent network architectures are based on use of the augmented MCP node.

[59] **Figure 3b** shows results for the distributed input (DI) case, with number of nodes (N_1) varying from 1-5. This case corresponds to the situation where an adequate description of the dynamics by which precipitation is partitioned into storage, evapotranspirative loss, and streamflow output requires that different *fractions* of incoming precipitation be routed along different flow paths. Increasing N_1 corresponds to increasing numbers of nodes in parallel, corresponding to different fractional distributions of precipitation to different flow paths. **Figure 3c** shows complementary results for the distributed state (DS) case, which corresponds to the situation where an adequate description of the “soil moisture state” of the system requires more than one summary statistic (the values of the cell-states). In this case the total amount of incoming precipitation provided to each node of the hidden layer is the same. Note that the DI and DS cases with only one node ($N_1 = 1$; colored blue) are equivalent to the case of a single augmented MCP node.

[60] **Figures 3d&e** correspond to the above-mentioned two cases, but where mass-conservation is relaxed at the network level. **Figure 3d** shows results for the distributed input relaxed (DIR) case, where total input mass can be adjusted, while **Figure 3e** shows results for the distributed state relaxed (DSR) case, where total output mass can be adjusted. Finally **Figure 3f** corresponds to the MLB case where the network-level constraint on mass-conservation is relaxed both at the input layer and the output layer.

[61] For all of these subplots (**Figures 3b-f**), the dashed blue line indicates median performance of a single (augmented) MCP node, while the dashed red line indicates best median performance over all the architectures being compared at this stage. As can be seen, while all of the networks with more than one node obtain better median performance (above the blue dashed line), that improvement is not large. For the DI case (**Figures 3b**), no median improvement is obtained beyond two nodes, whereas for the DS case there are fewer outlier years (indicated by the dark red + symbols) and worst year performance (indicated by the yellow-filled circle symbols) is significantly improved with increasing N_1 .

[62] In contrast, for the DIR case where bias correction of the input is permitted, we see considerable improvement in performance for the drier years in the catchment history. And for the DSR case the performance distributions become less skewed (fewer outlier years, indicated by the dark red + symbols) and worst year performance (indicated by the yellow-filled circle symbols) is significantly improved. Notably, worst year performance progressively improves as the number of nodes generally increased. Overall, these dry-year improvements persist into the MLB case, where both the input and output can be bias corrected, and best median performance is obtained by the MLB case when the number of nodes $N_1 = 3 - 5$. Note, however, that removing the input and output mass conservation constraints on the single MCP node (case $MN_{None}^{MLB}(1)$) results in a considerable deterioration in performance.

[63] Overall, these results suggest that the “distributed-state” (DS) architecture should be preferred over the “distributed-input” (DI) architecture, but that network-level mass relaxation at both input and output layers (MLB) is beneficial to overall model performance. Of course, when adopting the MLB architecture, the ability to interpret what is happening is diminished, and the machine-learning benchmark can be interpreted as incorporating input and output bias corrections along with a hybrid “distributed-input-state” architecture in which the distinction between these notions is made fuzzy. Arguably, this might make sense since it

simultaneously allows for both spatial distribution (and bias correction) of input mass and a distributional notion for the state of “moisture” in the system.

[64] **Figure 4a** shows the best cases from each of these architectures selected based on median year, below median years, and worst year performance, compared with the baseline single-augmented-node case (blue). Overall, these cases show some improvement compared to the baseline case. However, drawing upon notions of parsimony (minimum description length) to impose an inductive bias on model selection, we might select the MLB architecture with three nodes ($MN_{None}^{MLB}(3)$; green color) as displaying the “best” overall distributional KGE_{ss} performance, with $KGE_{ss}^{min} = 0.67$ and $KGE_{ss}^{50\%} = 0.87$.

[65] **Figures 4b-d** show dry, medium and wet year (note the differing y-axis scaling) hydrograph comparisons against observations (red circles) for the DS with 5 nodes ($MN_{None}^{DS}(5)$; orange lines) and MLB with 3 nodes ($MN_{None}^{MLB}(3)$; yellow lines) cases, selected for their better performance under dry year conditions (most ML approaches tend to demonstrate robust performance under wet year conditions). Note that both models (and particularly $MN_{None}^{MLB}(3)$) demonstrate improved ability to capture high flow peaks compared to the baseline single-node model (blue lines), while the DS model ($MN_{None}^{DS}(5)$) tends to perform better under low-flow conditions, such as during the recession period from January to February of 1952 (see also log-y-axis plots shown in **Figure S1** in the supplementary materials). These results suggests that some more flexible combination of the two strategies – a distributed state representation (for its improved low-flow performance) with varying degrees of mass relaxation under different wetness conditions (for its high-flow performance) might prove to be beneficial in future investigations. Arguably this might make sense given that input data errors (at least for this catchment) tend to be more significant at higher magnitudes.

4.2 The Multi-Layer MCP-Based Architectures

[66] Results from the previous section suggest that the distributed-state (DS) approach is better suited than the distributed-input (DI) approach for representing the hydrologic system of the Leaf River catchment. For this next part of the study, we therefore only pursued the DS approach (input weights all equal to 1.0) when investigating the performance of a multi-layer network.

[67] One reason for not pursuing the DI approach further is that adding more layers could be considered analogous to creating a more complex representation of flow routing, whereas our experience with the Leaf River Basin, supported by decades of modeling, suggests that a fairly simple representation of routing is sufficient. In contrast, the DS approach aligns better with the idea of learning a more complex representation for functional approximation. For now, we choose to leave further exploration of such complexities for future work.

[68] In pursuing the DS approach, we next considered three possible configurations for the linear output layer – the MN_{None}^{DS} case where the (positive valued) output weights sum to 1.0, the MN_{None}^{DSR} case where the (positive valued) output weights are not constrained to sum to 1.0, and the MN_{None}^{DS-MLB} case where the output weights are neither constrained to be positive or sum to 1.0, and where an additional bias term is included in both the transformation and output layers. In theory, the added flexibility permitted in the latter architecture should increase the learning capability of the network and allow it to better capture the complex dynamics of the system. For each of these cases, we examined 36 networks by varying the number of layers from 1 to 3 and the number of nodes per layer from 1 to 3 (**Table S8**).

[69] **Figure 5** presents box plots summarizing all of these cases, along with the corresponding single-layer cases where node counts ranged up to 5. The leftmost set of figures corresponds to single layer networks, the middle set corresponds to networks with two hidden layers, and the rightmost set corresponds to networks with three hidden layers. The top row corresponds to the mass-conserving DS architectures (MN_{None}^{DS}), the middle row to the DS-relaxed architectures (MN_{None}^{DSR}), and the bottom row to the least constrained MN_{None}^{DS-MLB} architectures. To facilitate comparison of network complexity, across the top of the Figure we report the numbers of cell-states for each network.

[70] For the single-layer networks, all three cases lead to the same conclusion, which is that there is marginal utility in increasing the number of nodes beyond 2, with best performance (median $KGE_{SS} = 0.84$) achieved by the $MN_{None}^{DS-MLB}(2,0,0)$ architecture. For the two-layer networks, performance noticeably improves when the first layer contains more than one node. Of these, the (2,1,0) architectures with three cell-states can be viewed as analogous to the physical-conceptual HYMOD-like architecture where the subsurface flow path merges with the surface flow path before channel routing occurs. This observation supports previous findings (see [Wang & Gupta \(2024b\)](#)) that an adequate representation of Leaf River Basin rainfall-runoff dynamics requires more than one flow path (quick and slow). Overall, the (3,3,0) architectures with 3 cell states in each layer provide the best overall two-layer network performance, supporting the notion that three distributional statistics in each layer are required to adequately model this system. Finally, the three-layer network results show a clear and significant drop in performance.

[71] Dry, medium and wet year hydrographs for the different (3,3,0) architectures are included in the supplementary materials ([Figure S2](#)). Small improvements were found in reproduction of timing and flow peak. These multi-layer cases were also found to be less biased in their representations of low-flow. In general, the MLB case can be removed from consideration due to the fact that it can permit the flow values to become negative.

5. Results for MCP-Based Architectures with Information Sharing

5.1 Single-Layer MCP-Based Architectures with Information Sharing

[72] In the *DI*, *DS*, *DIR*, *DSR* and *MLB* architectures tested above, the value of the output gate (at each node in a layer) depends only on the magnitude of its own cell-state. And similarly, the value of the loss gate (at each node in a layer) depends only on that same cell-state, in addition to the magnitude of PET. In other words, there is no direct communication of cell-state information between nodes, so that the dynamic behavior of that node cannot be *directly* influenced by the dynamic behavioral of other nodes, and each node operates independently when computing output and loss fluxes.

[73] In principle, however, one can imagine that the dynamical behavior of a given node could be (at least in part) influenced by what is happening at (some or all of the) other nodes in the network. In other words, the nodes would *not* operate independently when computing output and loss fluxes, which would require some form of “*sharing*” of information between nodes. For example, in the case of the output gates this conceptually corresponds to the output conductivities of the system being dependent (in some complex fashion) on the “*overall description*” of the soil moisture state of the system (as characterized by the cell-state values of all the nodes). Just as the set of cell-states can be thought of as representing an approximate discrete representation of the distribution of soil moisture storages in the catchment (a set of “*almost sufficient*” statistics), the set of output conductivities can be considered to represent a corresponding approximate discrete representation of the (cell-state conditional) distribution of mass-flow conductivities. A similar conceptual idea applies to the loss gates.

[74] To investigate the potential benefits of such information sharing, we modified the output and loss gating functions of all of the nodes in such a manner that they have access to the cell state values of all other nodes in the same layer (in addition to their own cell-state value). As with the original gating functions (see Section 2.1), this cell-state information from the nodes is combined in a linear weighted fashion, such that the output gate for the i^{th} node in layer ℓ can be written as $G_t^{o_{i\ell}} = \kappa_{o_{i\ell}} \cdot \sigma(b_{o_{i\ell}} + \sum_{j=1}^N a_{ij\ell}^o \cdot \tilde{X}_t^{j\ell})$, and the loss gate is written as $G_t^{L_{i\ell}} = \kappa_{L_{i\ell}} \cdot \sigma(b_{L_{i\ell}} + \sum_{j=1}^N a_{ij\ell}^L \cdot \tilde{X}_t^{j\ell})$ where $a_{ij\ell}^o$, $b_{o_{i\ell}}$, $\kappa_{o_{i\ell}}$, and $a_{ij\ell}^L$, $b_{L_{i\ell}}$, $\kappa_{L_{i\ell}}$ are trainable parameters.

[75] In the rest of this section, we test the benefits of information sharing for the five basic network single-layer architectures (*DI*, *DS*, *DIR*, *DSR* and *MLB*) discussed in Section 3.5. Since we have two kinds of gates – output and loss – we consider three cases: (i) *SAO*: information sharing at the output gates only, (ii) *SAL*:

information sharing at the loss gates only, and (iii) *SALO*: information sharing at both output and loss gates. The results, for different numbers of nodes in the hidden layer, are presented in [Figures 6-8](#).

5.1.1 Information Sharing at the Output Gate Only

[76] [Figure 6](#) shows results for the *SAO* case where information sharing is permitted at the output gate only. Across the board, regardless of architecture type (*DI*, *DS*, *DIR*, *DSR* and *MLB*), information sharing at the output gate improves performance (compare with [Figure 3](#)), with overall best median and above median (wet) year KGE_{ss} performance achieved by the *DSR* architecture ($N_1 = 5$) and overall best distributional and below median (dry) year performance achieved by the *MLB* architecture ($N_1 = 5$).

[77] Performance improvement for the distributed input (*DI*) architecture ([Figure 6a](#)) saturates at about $N_1 = 2$ with the median and minimum KGE_{ss} values reaching 0.87 and 0.65 respectively. Permitting input-mass-adjustments to the *DI* architecture (*DIR*) does tend to help a bit ([Figure 6c](#)), with narrowing of the distribution and performance generally improving for above-median years.

[78] Performance for the distributed state (*DS*) architecture ([Figure 6b](#)) continues to improve till $N_1 = 4$ with the median and minimum KGE_{ss} values reaching 0.91 and 0.72 respectively. But when output-mass-adjustments are permitted (*DSR*: [Figure 6d](#)), we see progressive improvement till $N_1 = 5$, (median $KGE_{ss} = 0.92$) with significant improvements extending into below median years with minimum KGE_{ss} reaching 0.70.

[79] For the *MLB* architecture ([Figure 6e](#)) where mass-adjustments are permitted to both inputs and outputs, although single node performance – where the concept of information sharing does not exist – is rather poor (see [Figure 3](#)), increasing N_1 up till 5 results in progressive overall improvement with the minimum (driest year) KGE_{ss} reaching 0.76, the best achieved by any of the architectures tested so far.

5.1.2 Information Sharing at the Loss Gate Only

[80] [Figure 7](#) shows similar results for the *SAL* case where information sharing is permitted only at the loss gate. In this case, we see almost no improvement, which is perhaps not surprisingly given that runoff fluxes strongly dominate over evapotranspirative fluxes in this basin. The main improvement is when input-mass adjustments are allowed (*DIR*; [Figure 7c](#)), when we get noticeable improvements in the minimum KGE_{ss} (reaches 0.77) especially for $N_1 = 5$.

5.1.3 Information Sharing at both Output and Loss Gates

[81] [Figure 8](#) shows results for the *SALO* case where information sharing is permitted at both the output and loss gate. For all architectural cases (*DI*, *DS*, *DIR*, *DSR* and *MLB*), we see performance improvements (particularly on the below median years) compared with *SAO*, where sharing is only at the output gates. Once again, the best overall KGE_{ss} performance is achieved for the distributed state (*DS*; median $KGE_{ss} = 0.92$) and mass-relaxed distributed state (*DSR*; median $KGE_{ss} = 0.92$) cases with $N_1 = 5$, with the latter being slightly better (similar median, but tighter distribution, better below median performance, and overall best worst year performance $KGE_{ss} = 0.76$).

5.2 Multi-Layer MCP-Based Architectures with Information Sharing

[82] Next, we repeated the multi-layer MCP network experiments summarized in Section 4.2, but allowed the cell states to share information at the gates (see [Figure 9](#)). For brevity, we report only results for the *SALO* case where cell-state information is shared at both the output and loss gates. Note that this is analogous to modern recurrent neural networks, such as LSTMs, where sharing occurs across all gates.

[83] Unlike in the non-sharing case ([Figure 5](#)), overall network performance declines as the number of layers is increased, in the sense that no 2-layer network outperforms the best single-layer network, and, no 3-layer network outperforms the best 2-layer network. Overall, best performance is obtained by the single-layer 5 node case ($N_1 = 5$) with median $KGE_{ss} = 0.92$ for the distributed state *DS*, *DSR* and *MLB* architectures. This

suggests that information-sharing helps the model achieve greater architectural parsimony, and is more important than increasing network depth.

5.3 Summary and Discussion

[84] In summary, incorporating cell-state information sharing at the gates results in significant performance improvements.

- 1) The distributed state (DS) architectural hypothesis generally performs better than the distributed input (DI) hypothesis, supporting the idea that more than one “soil-moisture” statistic is required to adequately model the input-state-output dynamics of the Leaf River Basin.
- 2) Consistent with conceptual understanding, incorporating sharing at the output gates tends to more significantly improve performance on the above median years (which tend to be wetter) while incorporating sharing at the loss gates tends to more significantly improve performance on the below median years (which tend to be drier).
- 3) Further, although mass is conserved at the nodes, there appears to be some (relatively small) benefit to allowing for mass-relaxation at the overall network level. However, most stable performance seems to be achieved using the more strongly regularized *DSR* architecture (where input weights are all constrained to be one and all output weights are constrained to be positive) rather than the *MLB* architecture where both the input and output weights are allowed to vary freely.
- 4) Overall, best performance is obtained by a relatively parsimonious single-layer distributed state (*DS*) or mass-relaxed distributed state (*DSR*) architecture when information sharing across the nodes is permitted.

6. Benchmarking against Physical-Conceptual Models and the LSTM Network

6.1 Benchmark Models

[85] To complete this part of the investigation, we compare the performance of models developed using the proposed MCP-network-based strategy against that obtained using (i) purely data-driven LSTM-based models that are not required to conserve mass at either the nodal or network levels, and (ii) several physical-conceptual mass-conserving model architectures (hereafter referred to as MAs; [Wang & Gupta, 2024b](#)) that are required to conserve mass at both the nodal and overall architectural levels.

[86] The latter (physical-conceptual) MA models span four progressively more complex conceptual architectural hypotheses regarding system structure, referred to as MA_3 , MA_4 , MA_5 , and MA_6 . The MA_3 model consists of one flow-path with two cell-states in series, the first interpreted as a lumped-average catchment soil moisture storage and the second interpreted as a routing store. The MA_4 model consists of two flow-path with two cell-states in parallel, with one interpreted as a lumped-average catchment soil moisture storage that generates (near)surface flow, and the second interpreted as a subsurface (groundwater) store that can sustain baseflow. The MA_5 model consists of three cell-states and two flow-paths. It essentially extends the MA_4 architecture to include surface/channel routing. The MA_6 model extends the MA_5 architecture to include an overland flow path that routes overland flow directly to the catchment outlet.

[87] Given the previous findings of this study that access to information about *all* of the cell states can improve the estimation of hydraulic conductivities computed by the output gates, and thereby the overall performance of the model, we investigate two versions of the aforementioned physical-conceptual $MA_3 - MA_6$ models. In the first, we retain the traditional strategy used in catchment-scale hydrological modeling where the output fluxes at each moisture tank (cell-state) *do not draw upon* on knowledge of the overall distribution of soil moisture throughout the system – i.e., information remains local. In the second, we *do allow* the output fluxes at each moisture tank to depend on the overall distribution of soil moisture throughout the system – i.e., information is shared globally.

[88] For the purely data-driven LSTM-based models, we extend upon the results reported in [Wang & Gupta \(2024a\)](#) and examine LSTM networks ([Hochreiter & Schmidhuber, 1997](#)) with up to 5 nodes per layer and up to three layers. Overall, the numbers of trainable parameters for the most complex (three-layer 15-cell-state) LSTM network reaches 486. Note that, due to the lack of any physically-conceptual regularizing restrictions on its architectural form, the performance of the *LSTM* network represents an approximate upper benchmark on precipitation-to-streamflow conversion performance achievable using the Leaf River data set ([Nearing et al., 2020](#)).

6.2 Results of Benchmark Comparisons

[89] Results of the benchmarking study are summarized by [Figure 10](#). The results are grouped into five sets, where the pink color represents the traditional physical-conceptual modeling approach (architectures $MA_3 - MA_6$) where there is no global sharing of cell-state information, the red color represents the same architectures but where cell-state information is shared globally, the light green color represents various selected MCP-based network architectures without sharing of cell-state information, the dark green color represents selected MCP-based network architectures with sharing of cell-state information, and the blue color represents selected LSTM-based networks.

[90] The MCP-based networks reported here, with or without information sharing, were selected based on overall best performance as reported in the previous sections. The LSTM-based networks reported here were also based on overall best performance as reported in the supplementary materials ([Table S9-10](#)).

[91] In summary, we notice the following:

- 1) Best overall distributional, median year, and worst year performance is achieved by the single-layer, 5-node MCP-based mass-conserving networks with cell-state information sharing (dark green) tested in this paper.
- 2) For the physical-conceptual modeling approach (pink and red), cell-state information sharing results in some degree of performance improvement, suggesting that this strategy might be beneficial to adopt more generally in physically-based modeling.
- 3) The distributed-state MCP-based mass-conserving networks (light green) tend to provide better below-median and worst-year performance, than the traditional physical-conceptual architectures, suggesting that we might be able to learn something from the network-based approach about how to construct better physical-conceptual hypotheses. In particular, the notion of a distributed-state (multiple-statistic) surface moisture storage might be worth exploring ... this would be an extension of the probability distributed moisture (PDM; [Moore, 2007](#)) store concept already successfully adopted by models such as HyMod ([Boyle et al., 2000](#)) and the variable infiltration capacity model (VIC; [Liang et al., 1994](#)), etc.
- 4) The single-layer, 5-node MCP-based mass-conserving networks with cell-state information sharing (dark green) performs comparably to the purely data-driven LSTM-based models (which do not incorporate any mass-conservation restrictions) tested here. This is encouraging given that the *LSTM* network can be assumed to represent an approximate upper performance benchmark. Interestingly, the more regularized architecture of the MCP-based network tends to result in better performance on the below-median and drier years, suggesting that the mass-conserving regularization tends to result in more stable model performance.

7. Network Interpretability

7.1 Internal Functioning of Single-Layer Distributed-State Network

[92] A major premise of this work is that catchment-scale models constructed using MCP-based networks are more readily interpretable than ones constructed using conventional machine learning strategies. **Figures 11 & 12** illustrate the interpretability of the single-layer distributed-state (DS) models reported in Section 4.1.

[93] **Figures 11a-e** show the forms of the output-gate conductivity functions learned by the single-layer DS models as the number of MCP nodes is progressively increased from 1 to 5. Notice that each gate remains “closed” when the cell-state is below some level (e.g., $< \sim 700$ mm in **Figure 11a**), and then rapidly “opens” till it reaches some maximum conductivity level (e.g., ~ 0.045 mm/mm in **Figure 11a**); recall that the minimum and maximum possible conductivity levels are 0.0 and 1.0 mm/mm respectively. To facilitate interpretability, we have color coded the gating functions according to their maximum conductivity values (y-axis) such that blue $<$ red $<$ orange $<$ purple $<$ green.

[94] Meanwhile **Figure 12** shows plots of dynamically evolving time series values for a dry-year (WY 1952; left column), median-year (WY 1953; middle column), and wet-year (WY 1974; right column). Here, for brevity, we focus our discussion primarily on the specific case of the three-node DS architecture ($MN_{None}^{DS}(3)$). Corresponding results for all five cases ($MN_{None}^{DS}(1)$ to $MN_{None}^{DS}(5)$) are presented in the supplementary materials (**Figures S4-S11**).

[95] Each row of **Figure 12** shows a different variable. The top row shows the observed streamflow hydrograph. The second, fourth and sixth rows show the corresponding cell states, output gate states, and the accumulated components of streamflow, color coded to correspond to **Figure 11c** (blue, red and orange for the nodes with lowest, intermediate and largest maximum output conductivity values respectively). Meanwhile, the third, fifth and seventh rows show the same values as in rows two, four and six, but plotted as fractions of their total values.

[96] **Wang & Gupta (2024a)** previously discussed the behavioral expressivity of the single-node case ($MN_{None}^{DS}(1)$) in great detail; its cell state value varies between $\sim 375 - 700$ mm (**Figures S4d-i**), and the output gate activates when the cell state reaches ~ 600 mm. In contrast, the two-node $MN_{None}^{DS}(2)$ case has two cell states and two flow-paths. From **Figure 11b** we see that the output gate for the first node (blue) activates at a smaller cell state value (~ 577 mm) than for the second node (red; ~ 707 mm), and is therefore a more active contributor to streamflow during the dry periods. In contrast, the second node activates during wetter periods, when the cell-state value is larger, whereupon it becomes the more dominant contributor to total streamflow (**Figures S10g-i**).

[97] In several ways, however, the $MN_{None}^{DS}(3)$ case is more interesting (**Figures 11c & 12**) because the three flow paths can be loosely interpreted as representing a slowly responding groundwater flow path (blue color; lower maximum conductivity), moderately responding interflow path (red color; intermediate maximum conductivity), and quickly responding surface flow path (orange color; higher maximum conductivity). Node 1 (blue) can be interpreted as representing the behavior of the groundwater system and storing the largest fraction of water in the system (**Figures 12d-i**). Its output gate activates at ~ 585 mm but reaches a relatively low maximum output conductivity value of 0.055 mm/mm (**Figure 11c**), so that it contributes the smallest total volume to streamflow ($\sim 12\%$; **Figures 12p-u**), but remains active during the non-raining periods and thereby sustains baseflow throughout the year.

[98] Meanwhile, given that the LRB is a perennial stream, the second (red) and third (orange) nodes can be interpreted as both generating significant rapid contributions to streamflow in response to pulses of rainfall. The second node (red) starts to generate contributions to streamflow when its cell-state becomes larger than ~ 496 mm, while the third node (orange) activates when its cell-state becomes larger than ~ 226 mm (**Figure 11c**). Overall, these two nodes correspond to smaller cell-state values but generate the largest proportions

(~44% each) of overall streamflow by becoming active/responsive during the rainfall-driven periods, consistent with an interpretation of corresponding to shallower depths of soil-moisture storage located closer to the surface.

[99] Finally, it is interesting to note that Node 1 of the four-node $MN_{None}^{DS}(4)$ case also behaves in a manner representing a groundwater flow path (**Figure S4m-o**) in that it contributes to streamflow only during very dry periods (**Figures S10m-o**), with its cell state exhibiting only very mild variations. Meanwhile, the other three output gates behave very similarly to those of the three-node $MN_{None}^{DS}(3)$ case. This suggests the possibility that two groundwater flow components – faster and slower – may be required in the Leaf River Basin (a feature that is built into the SACSMA conceptual rainfall-runoff model used by the National Weather Service for streamflow forecasting). However, when investigating the five-node case (subplots p to r in **Figures S4-11**), although “metric-based” performance clearly improves, interpretability becomes increasingly more ambiguous/difficult, with the results allowing for multiple possible explanations.

7.2 Pruning Flow Paths

[100] The analysis conducted in Section 7.1 indicates that the five-node $MN_{None}^{DS}(5)$ network may contain redundant flow paths. This hypothesis is supported by two observations: (1) multiple gating functions (red and orange in **Figure 11e**) exhibit very similar functional behavior, and (2) several flow paths make very similar contributions to total streamflow (**Figures S10p-r**). To gain further insight into how these internal mechanisms may be functioning, we investigated how the predictive performance of the “five-node” models is affected by successive pruning (removing) of nodes from the networks. We do this for the single-layer distributed state $MN_{None}^{DS}(5)$ network, as well as the single-layer distributed state $MN_{SALO}^{DS}(5)$ network that has been enhanced to incorporate Sharing-Augmented Loss and Output (SALO) into the gates (**Table S11**).

[101] The strategy for removing nodes that we followed was to systematically prune different numbers of nodes (1, 2, 3 and 4) from the optimized 5-node configuration and, for each pruning case, identify the pruned case having the best possible performance. Note that, at this stage, no further re-training (fine-tuning) of the networks was conducted. So, to be clear, pruning one node results in five different cases, from which the case with the best median KGE_{SS} performance was selected. Similarly, pruning two, three, and four nodes yields ten, ten, and five possible cases, respectively. For each pruning scenario, we select and report only the case having the best median KGE_{SS} performance (without re-training).

[102] For ease of comparison, **Figure 13a** presents the results (KGE_{SS} boxplots) showing how performance of the “non-information sharing” $MN_{None}^{DS}(N)$ networks varies for $N = 1 \rightarrow 5$, while **Figure 13b** shows the (best) results obtained as successive numbers of nodes (from one to four) were pruned from the $MN_{None}^{DS}(5)$ architecture. So, the results labeled as $MN_{None}^{DS}(5) - D1(P)$ correspond to removing one node from $MN_{None}^{DS}(5)$, and so on, where the notation “P” indicates that the corresponding flow “paths” have been removed from the output layer of the network.

[103] It is interesting to note that some aspects of the distribution of KGE_{SS} skill have improved when comparing the “pruned” four-cell-state $MN_{None}^{DS}(5) - D1(P)$ case to its parent “un-pruned” five-cell-state $MN_{None}^{DS}(5)$ case. Specifically, we note a small increase in KGE_{SS}^{max} (from 0.93 \rightarrow 0.94), and a larger increase in $KGE_{SS}^{25\%}$ (from 0.78 \rightarrow 0.82) and in the lower quartiles, while $KGE_{SS}^{50\%}$ remains essentially unchanged (at 0.86). This improvement is also observed when compared to the four-cell-state $MN_{None}^{DS}(4)$ case. Meanwhile, a small loss in performance is observed for the very “driest” (outlier) year. However, when more than one node is removed from $MN_{None}^{DS}(5)$, performance significantly declines.

[104] Similarly, **Figures 13c & d** presents corresponding results for the “information sharing” cases. Note, as reported before (Section 5.1), that overall performance improves (**Figure 13c**) compared to the non-sharing case (**Figure 13a**) for $N \geq 3$. However, as “flow paths” (not nodes, see discussion below) are progressively pruned (**Figure 13d**), removing 1 or 2 paths has little or no apparent impact on distributional performance, while removing 3 paths has a small impact and removing 4 paths has a significant impact. Specifically, removing

1 and 2 paths (cases $MN_{SALO}^{DS}(5) - D1(P)$ and $MN_{SALO}^{DS}(5) - D2(P)$) results in only small declines of $KGE_{SS}^{50\%} = 0.92 \rightarrow 0.91$ and $KGE_{SS}^{min} = 0.73 \rightarrow 0.71$ compared to the un-pruned $MN_{SALO}^{DS}(5)$ network. Meanwhile the pruned two-path $MN_{SALO}^{DS}(5) - D3(P)$ network maintains very similar predictive accuracy to the unpruned $MN_{SALO}^{DS}(5)$ network.

[105] To be clear, in these “*information-sharing*” cases (and unlike in the “*non-sharing*” cases), removal of *output flow paths* does *not* correspond to removal of *nodes*. In fact, the corresponding cell-states remain active and continue to provide (discrete distributional) cell-state information that is used by the output and loss gates of the nodes corresponding to the “*non-pruned*” flow pathways. Again, these results support the hypothesis that three flow paths are required to model the dynamics of the LRB, even though the desirable number of (information sharing) cell-states may be larger (as many as 5). Since there is no obvious need to account for snow accumulation and melt dynamics in the LRB, these three flow paths can again be interpreted as corresponding to slow, intermediate and fast flow pathways.

[106] For completeness, we finally examine an alternative approach to pruning the five-node/pathway $MN_{SALO}^{DS}(5)$ network, wherein we effectively remove *both* the “*pathway*” and its associated “*node*”, so that the information regarding cell-state of node corresponding to the removed pathway is not shared with the gating functions of the other (non-pruned) nodes. This is easily done by setting the associated “*weights/parameters*” to zero. Results are shown in [Figure 13e](#), where “*F*” refers to “*Full*” (as opposed to partial) removal of shared information. Clearly, performance declines significantly as flow paths and associated cell-states (nodes) are removed.

[107] Overall, from these experiments, we can conclude that maintaining sufficiently many cell-states (here 3 – 5) to represent the distributional properties (minimal sufficient statistics) of the “*moisture*” dynamics of the catchment is critical, while also ensuring that the fast, intermediate and slow flow pathways are properly represented.

8. Discussion and Future Directions

8.1. Discussion

[108] To recap, this study adopted the function approximation “*network*” paradigm employed by modern ML wherein a generic network architecture is implemented consisting of basis function nodes arranged in series and parallel. By adopting the physically-interpretable MCP computational unit as the fundamental computational unit, we were able to explore a variety of generic and important modeling issues, as listed in Section 1.3.

[109] Overall, for the humid Leaf River Basin, the results support a single-layer, three-to-five-nodes-in-parallel, “*distributed-state*” (DS) multiple-flow-path architecture with “*information sharing*” across the nodes. While mass-relaxation at the network level did slightly improve overall performance, it came with some loss in overall conceptual interpretability. Whereas adding depth (increasing from 1 to 2 layers) improved performance when nodal-information-sharing was not permitted, significantly better overall performance was achieved using a single layer with inter-nodal-information sharing. Further, a suitable balance between performance and overall conceptual interpretability was achieved by a network having three context-dependent-gating-controlled flow pathways (conceptually interpretable as slow, intermediate and fast) that “*activate*” at different times during the water year (with the slow pathway remaining active all year round) in response to different “*cell-state*” and “*hydroclimatic*” conditions. Meanwhile the results suggest that three-to-five cell states are required to adequately track the time-varying dynamics of moisture accumulation and release within the system.

[110] An interesting finding is that, as in data-based LSTM architectures, sharing of information across the gating mechanisms of the cell-states (rather than allowing them to operate in local isolation) helps to significantly improve performance across the full range of hydroclimatic conditions (dry, medium and wet

years). Sharing at the output gates enhances above-median (wetter) year performance, while sharing at the loss gates improves below-median (drier) year performance; see Section 5 for a more nuanced discussion. In this regard, by tracking, reporting and examined the “*distributions*” of annual performance metrics (rather than the conventional approach of reporting only the average performance over the entire testing period) we were able to explore better understand which aspects of model performance were sensitive to variations in network architectural design – a practice that we strongly recommend be adopted by other model development and evaluation studies. Finally, in Section 6 we show that information sharing can also be potentially beneficial if incorporated in the context of traditional physics-based models. Overall, this finding is consistent with recent advances in understanding regarding the modular processing of information (Boyd et al., 2018).

8.2. Related Work

[111] The MCP node can be considered to essentially be an enhanced version of the *Nash* linear reservoir (Nash, 1957), with the time-fixed conductivity function being replaced by time-variable gating. Alternatively, it can be viewed as a simplified form of gated recurrent unit, as forms the basis for LSTM networks (Hochreiter & Schmidhuber, 1997). Our results suggest that the distributed-state (DS) form of the network architectures examined here can potentially serve the role of a universal function approximator (Hornik et al., 1989) for geoscientific time series prediction. In contrast, the distributed-input (DI) network architecture more closely resembles conventional semi-distributed hydrological modeling wherein the incoming precipitation is partitioned into alternative flow pathways by means of an input-distribution function, in a manner analogous to the *Nash Cascade* network proposed by Frame et al. (2024). Although not explored here, MCP-based neural network architectures have the flexibility to incorporate spatially-distributed hydrologic data, allowing different aspects of the watershed to be represented with varying levels of complexity. In other words, the watershed can be treated as an interconnected system, leveraging downstream flow information to constrain and improve upstream flow estimates (Molina et al., 2024).

8.3. Future Directions

[112] Several directions towards enhanced modeling of conservative geoscientific systems suggest themselves. Future work could benefit from drawing upon ideas encoded by the recently proposed Hydro-LSTM network architecture (De la Fuente et al., 2024a) which demonstrates the value of using time-series information provided by recent hydroclimatic history to improve the performance of context-dependent gating, and by the complementary idea of latent space encoding recently proposed by Yang & Chui, (2023a,b) to facilitate the development of interpretable *regional* models (De la Fuente et al., 2024b). Another possibility is the use of Kolmogorov-Arnold Network theory combined with symbolic regression to construct/learn the forms of gating functions so as to gain additional physical interpretability (Klotz et al., 2017; Feigl et al., 2020; Udrescu & Tegmark, 2020; Liu et al., 2024b; Liu et al., 2024c).

[113] In this regard, an underutilized potential approach to improving physical interpretability of ML-based models (explored only briefly in Section 7) is through carefully designed strategies for network pruning (Blalock et al., 2020). In contrast to “*neural architecture search*”, as suggested in our previous work (Wang & Gupta, 2024b), the pruning strategy would begin with “*large*” networks and then progressively apply penalty regularization to the loss function with the goal of discovering more parsimonious “*optimal*” architectures (in the sense of balancing both performance and interpretability).

[114] In conclusion, due to its parsimonious architecture and physical interpretability (rooted in the principles and language of modern recurrent neural network theory), we believe that the interpretable Mass Conserving Perceptron can provide effective support for scientific inference and discovery. Overall, we anticipate that MCP-based modeling can play a significant role in the future of machine learning and its applications to geoscientific investigation.

Acknowledgments

The first author (YHW) would like to thank the late Thomas Meixner, as well as Jennifer McIntosh, Martha Whitaker, Eyad Atallah, Dale Ward, Ty Ferré, Jim Yeh, and Chris Castro, for their support, and to acknowledge the teaching and outreach assistantship support provided by the Department of Hydrology and Atmospheric Sciences and the University of Arizona Data Science Institute during the final two years of his Ph.D. study, which made the finalization of this work possible. We also thank University of Arizona Data Science Institute for providing HPC computation resources. YHW extends his gratitude to Derrick Zwickl and Sara Willis for their invaluable consultation on high-performance computing. The second author (HVG) acknowledges partial support by the Australian Centre of Excellence for Climate System Science (CE110001028), the inspiration and encouragement provided by members of the Information Theory in the Geosciences group (geoinftheory.org), and support for a 4-month research visit to the Karlsruhe Institute of Technology, Germany provided by the KIT International Excellence Fellowship Award program.

Open Research

The manuscript is currently being prepared for submission to peer review. The code used in this study will be made available upon acceptance of the paper.

References

- Acuña Espinoza, E., Loritz, R., Álvarez Chaves, M., Bäuerle, N. and Ehret, U., 2024. To bucket or not to bucket? Analyzing the performance and interpretability of hybrid hydrological models with dynamic parameterization. *Hydrology and Earth System Sciences*, 28(12), pp.2705-2719. <https://doi.org/10.5194/hess-28-2705-2024>
- Althoff, D., Bazame, H.C. and Nascimento, J.G., 2021. Untangling hybrid hydrological models with explainable artificial intelligence. *H2Open Journal*, 4(1), pp.13-28. <https://doi.org/10.2166/h2oj.2021.066>
- Arsenault, R., Martel, J.L., Brunet, F., Brissette, F. and Mai, J., 2023. Continuous streamflow prediction in ungauged basins: long short-term memory neural networks clearly outperform traditional hydrological models. *Hydrology and Earth System Sciences*, 27(1), pp.139-157. <https://doi.org/10.5194/hess-27-139-2023>
- Baydin, A.G., Pearlmutter, B.A., Radul, A.A. and Siskind, J.M., 2018. Automatic differentiation in machine learning: a survey. *Journal of Machine Learning Research*, 18, pp.1-43. <https://jmlr.org/papers/v18/17-468.html>
- Bennett, A. and Nijssen, B., 2021. Deep learned process parameterizations provide better representations of turbulent heat fluxes in hydrologic models. *Water Resources Research*, 57(5), p.e2020WR029328. <https://doi.org/10.1029/2020WR029328>
- Blalock, D., Gonzalez Ortiz, J.J., Frankle, J. and Gutttag, J., 2020. What is the state of neural network pruning?. *Proceedings of machine learning and systems*, 2, pp.129-146.
- Boyd, A.B., Mandal, D. and Crutchfield, J.P., 2018. Thermodynamics of Modularity - Structural Costs Beyond the Landauer Bound, *Physical Review X* 8, 031036.
- Boyle, D.P., Gupta, H.V. and Sorooshian, S., 2000. Toward improved calibration of hydrologic models: Combining the strengths of manual and automatic methods. *Water Resources Research*, 36(12), pp.3663-3674. <https://doi.org/10.1029/2000WR900207>
- Bunge, M., 1963. A general black box theory. *Philosophy of Science*, 30(4), pp.346-358. <https://doi.org/10.1086/287954>
- Chen, J., Zheng, F., May, R., Guo, D., Gupta, H. and Maier, H.R., 2022. Improved data splitting methods for data-driven hydrological model development based on a large number of catchment samples. p.128340. <https://doi.org/10.1016/j.jhydrol.2022.128340>
- Chen, Y.H. and Chang, F.J., 2009. Evolutionary artificial neural networks for hydrological systems forecasting. *Journal of Hydrology*, 367(1-2), pp.125-137. <https://doi.org/10.1016/j.jhydrol.2009.01.009>
- Clark, M.P., Slater, A.G., Rupp, D.E., Woods, R.A., Vrugt, J.A., Gupta, H.V., Wagener, T. and Hay, L.E., 2008. Framework for Understanding Structural Errors (FUSE): A modular framework to diagnose differences between hydrological models. *Water Resources Research*, 44(12), <https://doi.org/10.1029/2007WR006735>.
- Daniell, T.M., 1991. Neural networks. Applications in hydrology and water resources engineering. In *National Conference Publication- Institute of Engineers. Australia*.
- De la Fuente, L. A., Ehsani, M. R., Gupta, H. V., and Condon, L. E., 2024a: Toward interpretable LSTM-based modeling of hydrological systems, *Hydrol. Earth Syst. Sci.*, 28, 945–971, <https://doi.org/10.5194/hess-28-945-2024>.
- De la Fuente, L.A., Bennett, A., Gupta, H.V. and Condon, L.E., 2024b. A HydroLSTM-based Machine-Learning Approach to Discovering Regionalized Representations of Catchment Dynamics. *Authorea Preprints*. <https://doi.org/10.22541/essoar.172801404.45473140/v1>
- De la Fuente, L.A., Gupta, H.V. and Condon, L.E., 2023. Toward a Multi-Representational Approach to Prediction and Understanding, in Support of Discovery in Hydrology. *Water Resources Research*, 59(1), p.e2021WR031548. <https://doi.org/10.1029/2021WR031548>
- Domingos, P., 1998, August. Occam's two razors: The sharp and the blunt. In *KDD* (pp. 37-43).

- Feigl, M., Herrnegger, M., Klotz, D. and Schulz, K., 2020. Function space optimization: A symbolic regression method for estimating parameter transfer functions for hydrological models. *Water resources research*, 56(10), p.e2020WR027385. <https://doi.org/10.1029/2020WR027385>
- Feng, D., Beck, H., Lawson, K. and Shen, C., 2023. The suitability of differentiable, physics-informed machine learning hydrologic models for ungauged regions and climate change impact assessment. *Hydrology and Earth System Sciences*, 27(12). <https://doi.org/10.5194/hess-27-2357-2023>
- Feng, D., Fang, K. and Shen, C., 2020. Enhancing streamflow forecast and extracting insights using long-short term memory networks with data integration at continental scales. *Water Resources Research*, 56(9), p.e2019WR026793. <https://doi.org/10.1029/2019WR026793>
- Feng, D., Liu, J., Lawson, K. and Shen, C., 2022. Differentiable, learnable, regionalized process-based models with multiphysical outputs can approach state-of-the-art hydrologic prediction accuracy. *Water Resources Research*, 58(10), p.e2022WR032404. <https://doi.org/10.1029/2022WR032404>
- Fenicia, F., Kavetski, D. and Savenije, H.H., 2011. Elements of a flexible approach for conceptual hydrological modeling: 1. Motivation and theoretical development. *Water Resources Research*, 47(11). <https://doi.org/10.1029/2010WR010174>
- Fenicia, F., Savenije, H.H., Matgen, P. and Pfister, L., 2008. Understanding catchment behavior through stepwise model concept improvement. *Water Resources Research*, 44(1). <https://doi.org/10.1029/2006WR005563>
- Fleming, S.W., Watson, J.R., Ellenson, A., Cannon, A.J. and Vesselinov, V.C., 2021. Machine learning in Earth and environmental science requires education and research policy reforms. *Nature Geoscience*, 14(12), pp.878-880. <https://doi.org/10.1038/s41561-021-00881-3>
- Flügel, W.A., 1995. Delineating hydrological response units by geographical information system analyses for regional hydrological modelling using PRMS/MMS in the drainage basin of the River Bröl, Germany. *Hydrological Processes*, 9(3-4), pp.423-436. <https://doi.org/10.1002/hyp.3360090313>
- Frame, J.M., Bindas, T., Araki, R., Rapp, J. and Deardorff, E., Synchronization in hydrologic processes and modeling the response with concepts, physics and neural networks. *ESS Open Archive*. April 15, 2024. <https://doi.org/10.22541/essoar.171320241.14125931/v1>
- Frame, J.M., Kratzert, F., Klotz, D., Gauch, M., Shalev, G., Gilon, O., Qualls, L.M., Gupta, H.V. and Nearing, G.S., 2022. Deep learning rainfall–runoff predictions of extreme events. *Hydrology and Earth System Sciences*, 26(13), pp.3377-3392. <https://doi.org/10.5194/hess-26-3377-2022>
- Frame, J.M., Kratzert, F., Raney, A., Rahman, M., Salas, F.R. and Nearing, G.S., 2021. Post-processing the national water model with long short-term memory networks for streamflow predictions and model diagnostics. *JAWRA Journal of the American Water Resources Association*, 57(6), pp.885-905. <https://doi.org/10.1111/1752-1688.12964>
- Gauch, M., Kratzert, F., Klotz, D., Nearing, G., Lin, J. and Hochreiter, S., 2021. Rainfall–runoff prediction at multiple timescales with a single Long Short-Term Memory network. *Hydrology and Earth System Sciences*, 25(4), pp.2045-2062. <https://doi.org/10.5194/hess-25-2045-2021>
- Gong, W., Gupta, H.V., Yang, D., Sricharan, K. and Hero III, A.O., 2013. Estimating epistemic and aleatory uncertainties during hydrologic modeling: An information theoretic approach. *Water resources research*, 49(4), pp.2253-2273. <https://doi.org/10.1002/wrcr.20161>
- Gupta, H.V. and Nearing, G.S., 2014. Debates—The future of hydrological sciences: A (common) path forward? Using models and data to learn: A systems theoretic perspective on the future of hydrological science. <https://doi.org/10.1002/2013WR01509>
- Gupta, H.V., Clark, M.P., Vrugt, J.A., Abramowitz, G. and Ye, M., 2012. Towards a comprehensive assessment of model structural adequacy. *Water Resources Research*, 48(8). <https://doi.org/10.1029/2011WR011044>
- Gupta, H.V., Kling, H., Yilmaz, K.K. and Martinez, G.F., 2009. Decomposition of the mean squared error and NSE performance criteria: Implications for improving hydrological modelling. *Journal of hydrology*, 377(1-2), pp.80-91. <https://doi.org/10.1016/j.jhydrol.2009.08.003>

- Halff, A.H., Halff, H.M. and Azmoodeh, M., 1993, July. Predicting runoff from rainfall using neural networks. In *Engineering hydrology* (pp. 760-765). ASCE.
- Harrigan, S., Zsoter, E., Cloke, H., Salamon, P. and Prudhomme, C., 2023. Daily ensemble river discharge reforecasts and real-time forecasts from the operational Global Flood Awareness System. *Hydrology and Earth System Sciences*, 27(1), pp.1-19. <https://doi.org/10.5194/hess-27-1-2023>
- Hecht-Nielsen, R., 1987, June. Kolmogorov's mapping neural network existence theorem. In *Proceedings of the international conference on Neural Networks* (Vol. 3, pp. 11-14). New York, NY, USA: IEEE press.
- Hochreiter, S. and Schmidhuber, J., 1997. Long short-term memory. *Neural computation*, 9(8), pp.1735-1780. <https://doi.org/10.1162/neco.1997.9.8.1735>
- Hoedt, P.J., Kratzert, F., Klotz, D., Halmich, C., Holzleitner, M., Nearing, G.S., Hochreiter, S. and Klambauer, G., 2021, July. Mc-Istm: Mass-conserving lstm. In *International conference on machine learning* (pp. 4275-4286). PMLR.
- Höge, M., Scheidegger, A., Baity-Jesi, M., Albert, C. and Fenicia, F., 2022. Improving hydrologic models for predictions and process understanding using neural ODEs. *Hydrology and Earth System Sciences*, 26(19), pp.5085-5102. <https://doi.org/10.5194/hess-26-5085-2022>
- Hornik, K., Stinchcombe, M. and White, H., 1989. Multilayer feedforward networks are universal approximators. *Neural networks*, 2(5), pp.359-366. [https://doi.org/10.1016/0893-6080\(89\)90020-8](https://doi.org/10.1016/0893-6080(89)90020-8)
- Hsu, K.L., Gupta, H.V. and Sorooshian, S., 1995. Artificial neural network modeling of the rainfall-runoff process. *Water resources research*, 31(10), pp.2517-2530. <https://doi.org/10.1029/95WR01955>
- Jiang, S., Zheng, Y. and Solomatine, D., 2020. Improving AI system awareness of geoscience knowledge: Symbiotic integration of physical approaches and deep learning. *Geophysical Research Letters*, 47(13), p.e2020GL088229. <https://doi.org/10.1029/2020GL088229>
- Jiang, S., Zheng, Y., Wang, C. and Babovic, V., 2022. Uncovering flooding mechanisms across the contiguous United States through interpretive deep learning on representative catchments. *Water Resources Research*, 58(1), p.e2021WR030185. <https://doi.org/10.1029/2021WR030185>
- Kaplan, J., McCandlish, S., Henighan, T., Brown, T.B., Chess, B., Child, R., Gray, S., Radford, A., Wu, J. and Amodei, D., 2020. Scaling laws for neural language models. *arXiv preprint arXiv:2001.08361*.
- Karlbauer, M., Praditia, T., Otte, S., Oladyshkin, S., Nowak, W. and Butz, M.V., 2022, June. Composing partial differential equations with physics-aware neural networks. In *International Conference on Machine Learning* (pp. 10773-10801). PMLR.
- Kavetski, D. and Fenicia, F., 2011. Elements of a flexible approach for conceptual hydrological modeling: 2. Application and experimental insights. *Water Resources Research*, 47(11). <https://doi.org/10.1029/2011WR010748>
- Kingma, D.P. and Ba, J., 2014. Adam: A method for stochastic optimization. *arXiv preprint arXiv:1412.6980*. <https://doi.org/10.48550/arXiv.1412.6980>
- Klotz, D., Herrnegger, M. and Schulz, K., 2017. Symbolic regression for the estimation of transfer functions of hydrological models. *Water Resources Research*, 53(11), pp.9402-9423. <https://doi.org/10.1002/2017WR021253>
- Knoben, W.J., Freer, J.E., and Woods, R.A. (2019). Inherent benchmark or not? Comparing Nash–Sutcliffe and Kling–Gupta efficiency scores. *Hydrology and Earth System Sciences*, 23(10), 4323-4331. <https://doi.org/10.5194/hess-23-4323-2019>
- Kolmogorov, A.N., 1957. On the representation of continuous functions of many variables by superposition of continuous functions of one variable and addition. In *Doklady Akademii Nauk* (Vol. 114, No. 5, pp. 953-956). Russian Academy of Sciences.
- Koya, S.R. and Roy, T., 2024. Temporal Fusion Transformers for streamflow Prediction: Value of combining attention with recurrence. *Journal of Hydrology*, 637, p.131301. <https://doi.org/10.1016/j.jhydrol.2024.131301>

Kratzert, F., Gauch, M., Klotz, D. and Nearing, G., 2024. HESS Opinions: Never train an LSTM on a single basin. *Hydrology and Earth System Sciences Discussions*, 2024, pp.1-19. <https://doi.org/10.5194/hess-2023-275>, in review, 2024

Kratzert, F., Klotz, D., Brenner, C., Schulz, K. and Herrnegger, M., 2018. Rainfall–runoff modelling using long short-term memory (LSTM) networks. *Hydrology and Earth System Sciences*, 22(11), pp.6005-6022. <https://doi.org/10.5194/hess-22-6005-2018>, 2018

Kratzert, F., Klotz, D., Herrnegger, M., Sampson, A.K., Hochreiter, S. and Nearing, G.S., 2019a. Toward improved predictions in ungauged basins: Exploiting the power of machine learning. *Water Resources Research*, 55(12), pp.11344-11354. <https://doi.org/10.1029/2019WR026065>

Kratzert, F., Klotz, D., Herrnegger, M., Sampson, A.K., Hochreiter, S. and Nearing, G.S., 2019b. Toward improved predictions in ungauged basins: Exploiting the power of machine learning. *Water Resources Research*, 55(12), pp.11344-11354. <https://doi.org/10.1029/2019WR026065>

Kratzert, F., Klotz, D., Hochreiter, S. and Nearing, G.S., 2021. A note on leveraging synergy in multiple meteorological data sets with deep learning for rainfall–runoff modeling. *Hydrology and Earth System Sciences*, 25(5), pp.2685-2703. <https://doi.org/10.5194/hess-25-2685-2021>

Lan, N., Geyer, M., Chemla, E. and Katzir, R., 2022. Minimum description length recurrent neural networks. *Transactions of the Association for Computational Linguistics*, 10, pp.785-799. <https://doi.org/10.1162/tacl.a.00489>

Liang, X., Lettenmaier, D.P., Wood, E.F. and Burges, S.J., 1994. A simple hydrologically based model of land surface water and energy fluxes for general circulation models. *Journal of Geophysical Research: Atmospheres*, 99(D7), pp.14415-14428. <https://doi.org/10.1029/94JD00483>

Li, J., Hsu, K.L., Jiang, A.L. and Sorooshian, S., 2022, December. Attention-based Model for Rainfall-runoff Modeling Using Large-domain Datasets. In *AGU Fall Meeting Abstracts* (Vol. 2022, pp. H45B-06).

Liu, H., Simonyan, K. and Yang, Y., 2018. Darts: Differentiable architecture search. *arXiv preprint arXiv:1806.09055*. <https://doi.org/10.48550/arXiv.1806.09055>

Liu, C., Roy, T., Tartakovsky, D.M. and Dwivedi, D., 2024a. Baseflow identification via explainable AI with Kolmogorov-Arnold networks. *arXiv preprint arXiv:2410.11587*.

Liu, J., Bian, Y., Lawson, K. and Shen, C., 2024b. Probing the limit of hydrologic predictability with the Transformer network. *Journal of Hydrology*, p.131389. <https://doi.org/10.1016/j.jhydrol.2024.131389>

Liu, Z., Wang, Y., Vaidya, S., Ruehle, F., Halverson, J., Soljačić, M., Hou, T.Y. and Tegmark, M., 2024c. Kan: Kolmogorov-arnold networks. *arXiv preprint arXiv:2404.19756*.

Mai, J., Shen, H., Tolson, B.A., Gaborit, É., Arsenault, R., Craig, J.R., Fortin, V., Fry, L.M., Gauch, M., Klotz, D. and Kratzert, F., 2022. The great lakes runoff intercomparison project phase 4: the great lakes (GRIP-GL). *Hydrology and Earth System Sciences*, 26(13), pp.3537-3572. <https://doi.org/10.5194/hess-26-3537-2022>

Maier, H.R., Zheng, F., Gupta, H., Chen, J., Mai, J., Savic, D., Loritz, R., Wu, W., Guo, D., Bennett, A. and Jakeman, A., 2023. On how data are partitioned in model development and evaluation: Confronting the elephant in the room to enhance model generalization. *Environmental Modelling & Software*, 167, p.105779. <https://doi.org/10.1016/j.envsoft.2023.105779>

Molina, A.A.R., Frame, J.M., Halgren, J. and Gong, J., 2024. A Proof of Concept for Improving Estimates of Ungauged Basin Streamflow Via an LSTM-Based Synthetic Network Simulation Approach. *Authorea Preprints*.

Moore, R.J., 2007. The PDM rainfall-runoff model. *Hydrology and Earth System Sciences*, 11(1), pp.483-499. <https://doi.org/10.5194/hess-11-483-2007>

Nash, J.E., 1957. The form of the instantaneous unit hydrograph. *Comptes Rendus et Rapports Assemblée Generale de Toronto*, 3, pp.114-121. <https://nora.nerc.ac.uk/id/eprint/508550>

- Nearing, G., Cohen, D., Dube, V., Gauch, M., Gilon, O., Harrigan, S., Hassidim, A., Kratzert, F., Metzger, A., Nevo, S. and Pappenberger, F., 2023. AI Increases Global Access to Reliable Flood Forecasts. *arXiv preprint arXiv:2307.16104*. <https://doi.org/10.48550/arXiv.2307.16104>
- Nearing, G.S. and Gupta, H.V., 2015. The quantity and quality of information in hydrologic models. *Water Resources Research*, 51(1), pp.524-538. <https://doi.org/10.1002/2014WR015895>
- Nearing, G.S., Klotz, D., Frame, J.M., Gauch, M., Gilon, O., Kratzert, F., Sampson, A.K., Shalev, G. and Nevo, S., 2022. Data assimilation and autoregression for using near-real-time streamflow observations in long short-term memory networks. *Hydrology and Earth System Sciences*, 26(21), pp.5493-5513. <https://doi.org/10.5194/hess-26-5493-2022>
- Nearing, G.S., Kratzert, F., Sampson, A.K., Pelissier, C.S., Klotz, D., Frame, J.M., Prieto, C. and Gupta, H.V., 2021. What role does hydrological science play in the age of machine learning?. *Water Resources Research*, 57(3), p.e2020WR028091. <https://doi.org/10.1029/2020WR028091>
- Nearing, G.S., Ruddell, B.L., Bennett, A.R., Prieto, C. and Gupta, H.V., 2020. Does information theory provide a new paradigm for earth science? Hypothesis testing. *Water Resources Research*, 56(2), p.e2019WR024918. <https://doi.org/10.1029/2019WR024918>
- Nearing, G.S., Sampson, A.K., Kratzert, F. and Frame, J., 2020. Post-processing a Conceptual Rainfall-runoff Model with an LSTM.
- Nourani, V., 2017. An emotional ANN (EANN) approach to modeling rainfall-runoff process. *Journal of Hydrology*, 544, pp.267-277. <https://doi.org/10.1016/j.jhydrol.2016.11.033>
- Oladyshkin, S., Praditia, T., Kroeker, I., Mohammadi, F., Nowak, W. and Otte, S., 2023. The deep arbitrary polynomial chaos neural network or how Deep Artificial Neural Networks could benefit from data-driven homogeneous chaos theory. *Neural Networks*, 166, pp.85-104. <https://doi.org/10.1016/j.neunet.2023.06.036>
- Paszke, A., Gross, S., Massa, F., Lerer, A., Bradbury, J., Chanan, G., Killeen, T., Lin, Z., Gimelshein, N., Antiga, L. and Desmaison, A., 2019. Pytorch: An imperative style, high-performance deep learning library. *Advances in neural information processing systems*, 32.
- Rai, A., 2020. Explainable AI: From black box to glass box. *Journal of the Academy of Marketing Science*, 48, pp.137-141. <https://doi.org/10.1007/s11747-019-00710-5>
- Rudin, C., 2019. Stop explaining black box machine learning models for high stakes decisions and use interpretable models instead. *Nature machine intelligence*, 1(5), pp.206-215. <https://doi.org/10.1038/s42256-019-0048-x>
- Reggiani, P., Hassanizadeh, S.M., Sivapalan, M. and Gray, W.G., 1999. A unifying framework for watershed thermodynamics: constitutive relationships. *Advances in Water Resources*, 23(1), pp.15-39. [https://doi.org/10.1016/S0309-1708\(99\)00005-6](https://doi.org/10.1016/S0309-1708(99)00005-6)
- Reggiani, P., Sivapalan, M. and Hassanizadeh, S.M., 1998. A unifying framework for watershed thermodynamics: balance equations for mass, momentum, energy and entropy, and the second law of thermodynamics. *Advances in Water Resources*, 22(4), pp.367-398. [https://doi.org/10.1016/S0309-1708\(98\)00012-8](https://doi.org/10.1016/S0309-1708(98)00012-8)
- Reggiani, P., Sivapalan, M. and Hassanizadeh, S.M., 2000. Conservation equations governing hillslope responses: Exploring the physical basis of water balance. *Water Resources Research*, 36(7), pp.1845-1863. <https://doi.org/10.1029/2000WR900066>
- Sabzipour, B., Arsenault, R., Troin, M., Martel, J.L., Brissette, F., Brunet, F. and Mai, J., 2023. Comparing a long short-term memory (LSTM) neural network with a physically-based hydrological model for streamflow forecasting over a Canadian catchment. *Journal of Hydrology*, 627, p.130380. <https://doi.org/10.1016/j.jhydrol.2023.130380>
- Schotthöfer, S., Zangrando, E., Kusch, J., Ceruti, G. and Tudisco, F., 2022. Low-rank lottery tickets: finding efficient low-rank neural networks via matrix differential equations. *Advances in Neural Information Processing Systems*, 35, pp.20051-20063.
- Shen, C., 2018. A transdisciplinary review of deep learning research and its relevance for water resources scientists. *Water Resources Research*, 54(11), pp.8558-8593. <https://doi.org/10.1029/2018WR022643>

Shen, C., Appling, A.P., Gentine, P., Bandai, T., Gupta, H., Tartakovsky, A., Baity-Jesi, M., Fenicia, F., Kifer, D., Li, L. and Liu, X., 2023. Differentiable modelling to unify machine learning and physical models for geosciences. *Nature Reviews Earth & Environment*, 4(8), pp.552-567. <https://doi.org/10.1038/s43017-023-00450-9>

Shen, H., Tolson, B.A. and Mai, J., 2022. Time to update the split-sample approach in hydrological model calibration. *Water Resources Research*, 58(3), p.e2021WR031523. <https://doi.org/10.1029/2021WR031523>

Shwartz-Ziv, R. and Tishby, N., 2017. Opening the black box of deep neural networks via information. *arXiv preprint arXiv:1703.00810*. <https://doi.org/10.48550/arXiv.1703.00810>

Singh, V.P. (1988). Hydrologic systems. Volume I: Rainfall-runoff modeling. Prentice Hall, Englewood Cliffs New Jersey. <https://www.worldcat.org/title/hydrologic-systems-volume-i-rainfall-runoffmodeling/oclc/843459667>

Smith, J. and Eli, R.N., 1995. Neural-network models of rainfall-runoff process. *Journal of water resources planning and management*, 121(6), pp.499-508. [https://doi.org/10.1061/\(ASCE\)0733-9496\(1995\)121:6\(499\)](https://doi.org/10.1061/(ASCE)0733-9496(1995)121:6(499))

Sorooshian, S., 1983. Surface water hydrology: On-line estimation. *Reviews of Geophysics*, 21(3), pp.706-721. <https://doi.org/10.1029/RG021i003p00706>

Stanley, K.O. and Miikkulainen, R., 2002. Evolving neural networks through augmenting topologies. *Evolutionary computation*, 10(2), pp.99-127. <https://doi.org/10.1162/106365602320169811>

Tishby, N. and Zaslavsky, N., 2015, April. Deep learning and the information bottleneck principle. In *2015 IEEE information theory workshop (itw)* (pp. 1-5). IEEE. <https://doi.org/10.1109/ITW.2015.7133169>

Tsai, W.P., Feng, D., Pan, M., Beck, H., Lawson, K., Yang, Y., Liu, J. and Shen, C., 2021. From calibration to parameter learning: Harnessing the scaling effects of big data in geoscientific modeling. *Nature communications*, 12(1), p.5988. <https://www.nature.com/articles/s41467-021-26107-z>

Udrescu, S.M. and Tegmark, M., 2020. AI Feynman: A physics-inspired method for symbolic regression. *Science Advances*, 6(16), p.eaay2631. <https://www.science.org/doi/10.1126/sciadv.aay2631>

Vaswani, A., Shazeer, N., Parmar, N., Uszkoreit, J., Jones, L., Gomez, A.N., Kaiser, Ł. and Polosukhin, I., 2017. Attention is all you need. *Advances in neural information processing systems*, 30.

Varadharajan, C., Appling, A.P., Arora, B., Christianson, D.S., Hendrix, V.C., Kumar, V., Lima, A.R., Müller, J., Oliver, S., Ombadi, M. and Perciano, T., 2022. Can machine learning accelerate process understanding and decision-relevant predictions of river water quality?. *Hydrological Processes*, 36(4), p.e14565. <https://doi.org/10.1002/hyp.14565>

Xu, T. and Liang, F., 2021. Machine learning for hydrologic sciences: An introductory overview. *Wiley Interdisciplinary Reviews: Water*, 8(5), p.e1533. <https://doi.org/10.1002/wat2.1533>

Wang, Y.H. and Gupta, H.V., 2024a. A mass-conserving-perceptron for machine-learning-based modeling of geoscientific systems. *Water Resources Research*, 60(4), p.e2023WR036461. <https://doi.org/10.1029/2023WR036461>

Wang, Y.H. and Gupta, H.V., 2024b. Towards interpretable physical-conceptual catchment-scale hydrological modeling using the mass-conserving-perceptron. *Water Resources Research*, 60(10), p.e2024WR037224. <https://doi.org/10.1029/2024WR037224>

Weijs, S.V. and Ruddell, B.L., 2020. Debates: Does information theory provide a new paradigm for earth science? Sharper predictions using Occam's digital razor. *Water resources research*, 56(2), p.e2019WR026471. <https://doi.org/10.1029/2019WR026471>

Wi, S. and Steinschneider, S., 2024. On the need for physical constraints in deep learning rainfall-runoff projections under climate change: a sensitivity analysis to warming and shifts in potential evapotranspiration. *Hydrology and Earth System Sciences*, 28(3), pp.479-503. <https://doi.org/10.5194/hess-28-479-2024>

Willard, J., Jia, X., Xu, S., Steinbach, M. and Kumar, V., 2022. Integrating scientific knowledge with machine learning for engineering and environmental systems. *ACM Computing Surveys*, 55(4), pp.1-37. <https://doi.org/10.1145/3514228>

Yang, Y. and Chui, T.F.M., 2021. Modeling and interpreting hydrological responses of sustainable urban drainage systems with explainable machine learning methods. *Hydrology and Earth System Sciences*, 25(11), pp.5839-5858. <https://doi.org/10.5194/hess-25-5839-2021>

Yang, Y. and Chui, T.F.M., 2023a. Learning to Generate Lumped Hydrological Models. *arXiv preprint arXiv:2309.09904*. <https://doi.org/10.48550/arXiv.2309.09904>

Yang, Y. and Chui, T.F.M., 2023b. Profiling and pairing catchments and hydrological models with latent factor model. *Water Resources Research*, 59(6), p.e2022WR033684. <https://doi.org/10.1029/2022WR033684>

Zangrando, E., Schotthöfer, S., Ceruti, G., Kusch, J. and Tudisco, F., 2023. Rank-adaptive spectral pruning of convolutional layers during training. *arXiv preprint arXiv:2305.19059*. <https://doi.org/10.48550/arXiv.2305.19059>

Zheng, F., Chen, J., Maier, H.R., and Gupta, H. (2022). Achieving Robust and Transferable Performance for Conservation-Based Models of Dynamical Physical Systems. *Water Resources Research*, 58(5), e2021WR031818. <https://doi.org/10.1029/2021WR031818>

Table & Figure

Table 1. Summary of Single-Layer Mass-Conserving Neural Network (MN_s) architectural hypothesis in this study

Model Name	MCP Basic Kernal	Input Distribution Gate	Linear Output Layer	Information (Internal State) Sharing
$MN_{None}^{DI}(N_1)$ $MN_{SAO}^{DI}(N_1)$ $MN_{SAL}^{DI}(N_1)$ $MN_{SALO}^{DI}(N_1)$	$MC\{O_\sigma L_{\sigma+}^{con}\}$	Linear layer with weights sums equal to 1	Sum operation (combining all the output from each node)	No Sharing Output gate only Loss gate only Output and Loss gate
$MN_{None}^{DS}(N_1)$ $MN_{SAO}^{DS}(N_1)$ $MN_{SAL}^{DS}(N_1)$ $MN_{SALO}^{DS}(N_1)$		Unity	Linear layer with weights sums equal to 1	No Sharing Output gate only Loss gate only Output and Loss gate
$MN_{None}^{DIR}(N_1)$ $MN_{SAO}^{DIR}(N_1)$ $MN_{SAL}^{DIR}(N_1)$ $MN_{SALO}^{DIR}(N_1)$		Linear layer (without bias) with weights to be positive	Sum operation (combining all the output from each node)	No Sharing Output gate only Loss gate only Output and Loss gate
$MN_{None}^{DSR}(N_1)$ $MN_{SAO}^{DSR}(N_1)$ $MN_{SAL}^{DSR}(N_1)$ $MN_{SALO}^{DSR}(N_1)$		Unity	Linear layer (without bias) with weights to be positive	No Sharing Output gate only Loss gate only Output and Loss gate
$MN_{None}^{MLB}(N_1)$ $MN_{SAO}^{MLB}(N_1)$ $MN_{SAL}^{MLB}(N_1)$ $MN_{SALO}^{MLB}(N_1)$		Linear layer (w/o bias term) without constraints on weights and bias	Linear layer (with bias term) without constraints on weights and bias	No Sharing Output gate only Loss gate only Output and Loss gate

Table 2. KGE_{SS} scores for the Single-Layer Mass-Conserving Neural Networks (MNs)

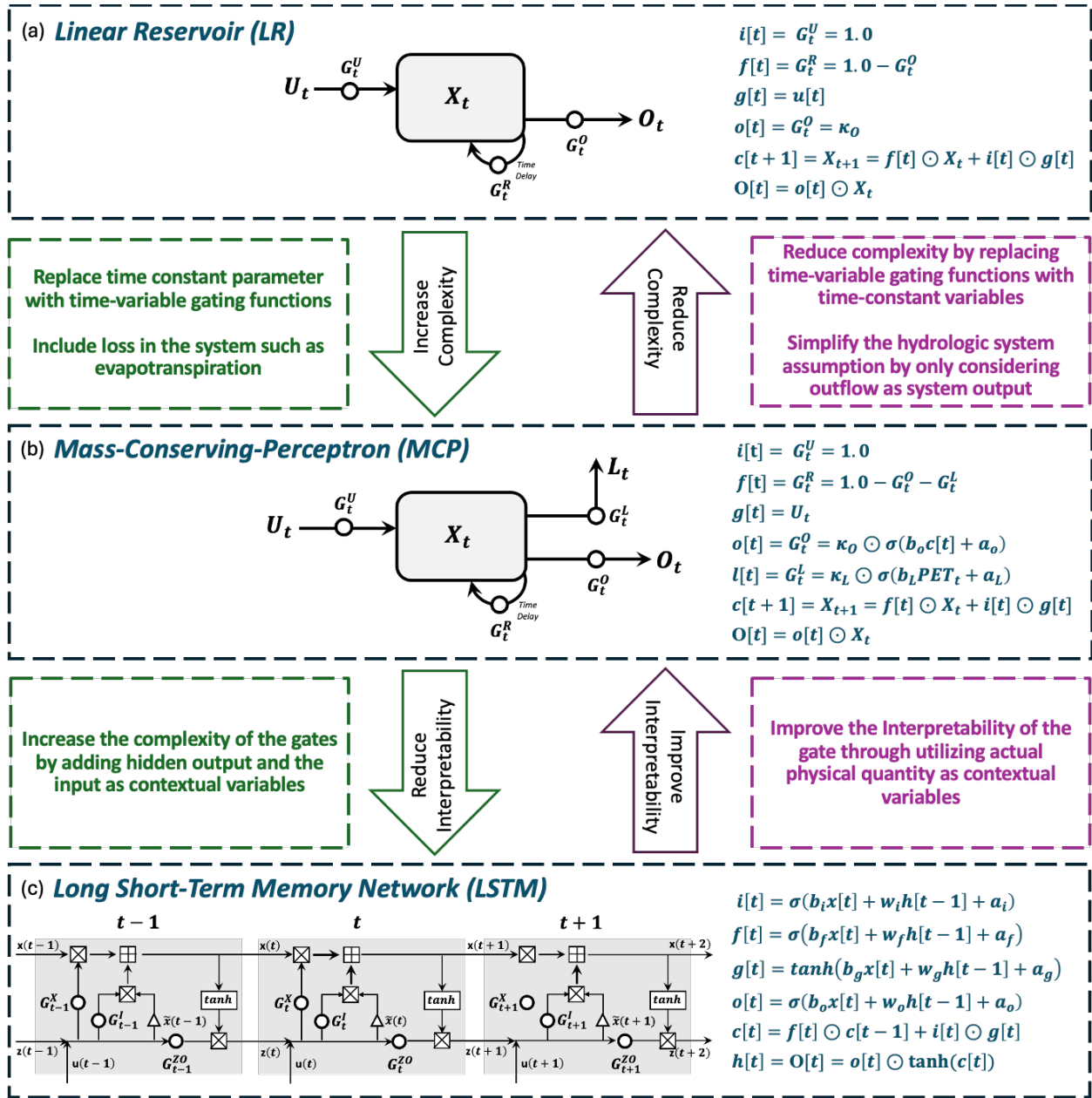
1-Node																							
	MN_{none}^{DI}	MN_{none}^{DS}	MN_{none}^{DIR}	MN_{none}^{DSR}	MN_{none}^{MLB}		MN_{SAL}^{DI}	MN_{SAL}^{DS}	MN_{SAL}^{DIR}	MN_{SAL}^{DSR}	MN_{SAL}^{MLB}		MN_{SAO}^{DI}	MN_{SAO}^{DS}	MN_{SAO}^{DIR}	MN_{SAO}^{DSR}	MN_{SAO}^{MLB}		MN_{SALO}^{DI}	MN_{SALO}^{DS}	MN_{SALO}^{DIR}	MN_{SALO}^{DSR}	MN_{SALO}^{MLB}
KGE_{SS}^{min}	0.57	0.57	0.57	0.55	0.36	KGE_{SS}^{min}	0.57	0.57	0.57	0.55	0.36	KGE_{SS}^{min}	0.57	0.57	0.57	0.55	0.36	KGE_{SS}^{min}	0.57	0.57	0.57	0.55	0.36
$KGE_{SS}^{5\%}$	0.70	0.70	0.68	0.66	0.42	$KGE_{SS}^{5\%}$	0.70	0.70	0.68	0.66	0.42	$KGE_{SS}^{5\%}$	0.70	0.70	0.68	0.66	0.42	$KGE_{SS}^{5\%}$	0.70	0.70	0.68	0.66	0.42
$KGE_{SS}^{25\%}$	0.81	0.81	0.81	0.80	0.64	$KGE_{SS}^{25\%}$	0.81	0.81	0.81	0.80	0.64	$KGE_{SS}^{25\%}$	0.81	0.81	0.81	0.80	0.64	$KGE_{SS}^{25\%}$	0.81	0.81	0.81	0.80	0.64
$KGE_{SS}^{50\%}$	0.84	0.84	0.84	0.85	0.83	$KGE_{SS}^{50\%}$	0.84	0.84	0.84	0.85	0.83	$KGE_{SS}^{50\%}$	0.84	0.84	0.84	0.85	0.83	$KGE_{SS}^{50\%}$	0.84	0.84	0.84	0.85	0.83
$KGE_{SS}^{75\%}$	0.87	0.87	0.87	0.88	0.85	$KGE_{SS}^{75\%}$	0.87	0.87	0.87	0.88	0.85	$KGE_{SS}^{75\%}$	0.87	0.87	0.87	0.88	0.85	$KGE_{SS}^{75\%}$	0.87	0.87	0.87	0.88	0.85
$KGE_{SS}^{95\%}$	0.91	0.91	0.91	0.91	0.91	$KGE_{SS}^{95\%}$	0.91	0.91	0.91	0.91	0.91	$KGE_{SS}^{95\%}$	0.91	0.91	0.91	0.91	0.91	$KGE_{SS}^{95\%}$	0.91	0.91	0.91	0.91	0.91
PNs	8	8	9	9	11	PNs	8	8	9	9	11	PNs	8	8	9	9	11	PNs	8	8	9	9	11
2-Node																							
KGE_{SS}^{min}	0.53	0.60	0.55	0.57	0.63	KGE_{SS}^{min}	0.48	0.63	0.56	0.54	0.65	KGE_{SS}^{min}	0.65	0.58	0.59	0.67	0.61	KGE_{SS}^{min}	0.61	0.56	0.63	0.63	0.68
$KGE_{SS}^{5\%}$	0.60	0.67	0.62	0.64	0.69	$KGE_{SS}^{5\%}$	0.55	0.66	0.67	0.63	0.69	$KGE_{SS}^{5\%}$	0.68	0.63	0.65	0.69	0.70	$KGE_{SS}^{5\%}$	0.62	0.63	0.66	0.68	0.71
$KGE_{SS}^{25\%}$	0.79	0.79	0.82	0.77	0.82	$KGE_{SS}^{25\%}$	0.78	0.79	0.83	0.76	0.82	$KGE_{SS}^{25\%}$	0.80	0.76	0.81	0.81	0.81	$KGE_{SS}^{25\%}$	0.81	0.77	0.82	0.80	0.82
$KGE_{SS}^{50\%}$	0.86	0.86	0.87	0.86	0.86	$KGE_{SS}^{50\%}$	0.86	0.86	0.87	0.85	0.88	$KGE_{SS}^{50\%}$	0.87	0.87	0.87	0.86	0.87	$KGE_{SS}^{50\%}$	0.87	0.86	0.88	0.86	0.88
$KGE_{SS}^{75\%}$	0.88	0.89	0.88	0.89	0.89	$KGE_{SS}^{75\%}$	0.88	0.89	0.89	0.89	0.89	$KGE_{SS}^{75\%}$	0.90	0.90	0.89	0.89	0.89	$KGE_{SS}^{75\%}$	0.89	0.90	0.90	0.89	0.89
$KGE_{SS}^{95\%}$	0.90	0.92	0.92	0.92	0.93	$KGE_{SS}^{95\%}$	0.90	0.92	0.92	0.92	0.93	$KGE_{SS}^{95\%}$	0.92	0.94	0.92	0.94	0.93	$KGE_{SS}^{95\%}$	0.93	0.94	0.92	0.95	0.93
PNs	18	18	18	18	21	PNs	20	20	20	20	23	PNs	20	20	20	20	23	PNs	22	22	22	22	25
3-Node																							
KGE_{SS}^{min}	0.52	0.62	0.55	0.58	0.67	KGE_{SS}^{min}	0.47	0.49	0.53	0.49	0.62	KGE_{SS}^{min}	0.62	0.68	0.58	0.71	0.63	KGE_{SS}^{min}	0.72	0.50	0.74	0.72	0.68
$KGE_{SS}^{5\%}$	0.59	0.69	0.62	0.62	0.69	$KGE_{SS}^{5\%}$	0.55	0.64	0.57	0.56	0.69	$KGE_{SS}^{5\%}$	0.66	0.75	0.64	0.73	0.67	$KGE_{SS}^{5\%}$	0.75	0.66	0.76	0.75	0.71
$KGE_{SS}^{25\%}$	0.78	0.79	0.82	0.78	0.82	$KGE_{SS}^{25\%}$	0.78	0.82	0.78	0.80	0.82	$KGE_{SS}^{25\%}$	0.81	0.86	0.81	0.85	0.82	$KGE_{SS}^{25\%}$	0.84	0.82	0.84	0.83	0.85
$KGE_{SS}^{50\%}$	0.86	0.86	0.87	0.86	0.87	$KGE_{SS}^{50\%}$	0.86	0.87	0.87	0.86	0.87	$KGE_{SS}^{50\%}$	0.85	0.90	0.87	0.89	0.87	$KGE_{SS}^{50\%}$	0.88	0.87	0.88	0.88	0.89
$KGE_{SS}^{75\%}$	0.88	0.88	0.88	0.89	0.90	$KGE_{SS}^{75\%}$	0.88	0.90	0.89	0.89	0.90	$KGE_{SS}^{75\%}$	0.90	0.93	0.90	0.93	0.92	$KGE_{SS}^{75\%}$	0.90	0.92	0.90	0.91	0.92
$KGE_{SS}^{95\%}$	0.90	0.92	0.92	0.92	0.92	$KGE_{SS}^{95\%}$	0.90	0.92	0.92	0.92	0.92	$KGE_{SS}^{95\%}$	0.94	0.96	0.93	0.96	0.94	$KGE_{SS}^{95\%}$	0.94	0.95	0.94	0.94	0.95
PNs	27	27	27	27	31	PNs	33	33	33	33	37	PNs	33	33	33	33	37	PNs	39	39	39	39	43
4-Node																							
KGE_{SS}^{min}	0.59	0.62	0.55	0.58	0.65	KGE_{SS}^{min}	0.53	0.63	0.57	0.46	0.64	KGE_{SS}^{min}	0.62	0.72	0.55	0.69	0.73	KGE_{SS}^{min}	0.71	0.49	0.71	0.74	0.62
$KGE_{SS}^{5\%}$	0.61	0.67	0.63	0.63	0.69	$KGE_{SS}^{5\%}$	0.56	0.71	0.60	0.62	0.71	$KGE_{SS}^{5\%}$	0.64	0.74	0.64	0.72	0.79	$KGE_{SS}^{5\%}$	0.73	0.70	0.73	0.82	0.68
$KGE_{SS}^{25\%}$	0.80	0.79	0.82	0.77	0.82	$KGE_{SS}^{25\%}$	0.81	0.83	0.80	0.81	0.83	$KGE_{SS}^{25\%}$	0.81	0.87	0.83	0.86	0.85	$KGE_{SS}^{25\%}$	0.84	0.85	0.84	0.88	0.84
$KGE_{SS}^{50\%}$	0.84	0.86	0.86	0.86	0.88	$KGE_{SS}^{50\%}$	0.86	0.87	0.86	0.87	0.88	$KGE_{SS}^{50\%}$	0.85	0.91	0.89	0.90	0.91	$KGE_{SS}^{50\%}$	0.88	0.89	0.88	0.91	0.89
$KGE_{SS}^{75\%}$	0.87	0.89	0.88	0.89	0.89	$KGE_{SS}^{75\%}$	0.88	0.89	0.89	0.89	0.90	$KGE_{SS}^{75\%}$	0.90	0.93	0.90	0.93	0.94	$KGE_{SS}^{75\%}$	0.90	0.93	0.90	0.93	0.91
$KGE_{SS}^{95\%}$	0.91	0.92	0.92	0.92	0.93	$KGE_{SS}^{95\%}$	0.91	0.92	0.92	0.92	0.93	$KGE_{SS}^{95\%}$	0.94	0.97	0.93	0.96	0.96	$KGE_{SS}^{95\%}$	0.94	0.96	0.94	0.97	0.95
PNs	36	36	36	36	41	PNs	48	48	48	48	53	PNs	48	48	48	48	53	PNs	60	60	60	60	65
5-Node																							
KGE_{SS}^{min}	0.53	0.63	0.57	0.58	0.63	KGE_{SS}^{min}	0.55	0.59	0.77	0.55	0.64	KGE_{SS}^{min}	0.61	0.61	0.57	0.71	0.76	KGE_{SS}^{min}	0.62	0.73	0.76	0.76	0.70
$KGE_{SS}^{5\%}$	0.59	0.66	0.59	0.62	0.68	$KGE_{SS}^{5\%}$	0.63	0.72	0.79	0.67	0.68	$KGE_{SS}^{5\%}$	0.64	0.70	0.67	0.77	0.78	$KGE_{SS}^{5\%}$	0.74	0.78	0.79	0.80	0.77
$KGE_{SS}^{25\%}$	0.78	0.78	0.80	0.77	0.82	$KGE_{SS}^{25\%}$	0.80	0.81	0.84	0.79	0.83	$KGE_{SS}^{25\%}$	0.81	0.85	0.83	0.87	0.88	$KGE_{SS}^{25\%}$	0.85	0.87	0.85	0.88	0.87
$KGE_{SS}^{50\%}$	0.86	0.86	0.87	0.86	0.88	$KGE_{SS}^{50\%}$	0.85	0.87	0.89	0.85	0.87	$KGE_{SS}^{50\%}$	0.87	0.91	0.88	0.92	0.90	$KGE_{SS}^{50\%}$	0.89	0.92	0.89	0.92	0.90
$KGE_{SS}^{75\%}$	0.88	0.88	0.89	0.89	0.90	$KGE_{SS}^{75\%}$	0.88	0.89	0.90	0.89	0.90	$KGE_{SS}^{75\%}$	0.90	0.93	0.91	0.94	0.93	$KGE_{SS}^{75\%}$	0.91	0.95	0.92	0.94	0.94
$KGE_{SS}^{95\%}$	0.90	0.92	0.93	0.92	0.93	$KGE_{SS}^{95\%}$	0.91	0.92	0.93	0.92	0.92	$KGE_{SS}^{95\%}$	0.94	0.96	0.93	0.96	0.96	$KGE_{SS}^{95\%}$	0.94	0.97	0.94	0.96	0.96
PNs	45	45	45	45	51	PNs	65	65	65	65	71	PNs	65	65	65	65	71	PNs	85	85	85	85	91

Table 3. KGE_{SS} Statistics and Numbers of Parameter for the single-layer Mass-Conserving Networks and the single-layer LSTM Networks

Model Names	$MN_{None}^{DS}(2)$	$MN_{None}^{DS}(3)$	$MN_{None}^{DS}(4)$	$MN_{None}^{DS}(5)$	$MN_{SALO}^{DS}(2)$	$MN_{SALO}^{DS}(3)$	$MN_{SALO}^{DS}(4)$	$MN_{SALO}^{DS}(5)$
KGE_{SS}^{min}	0.60	0.62	0.62	0.63	0.56	0.50	0.49	0.73
$KGE_{SS}^{5\%}$	0.67	0.69	0.66	0.66	0.63	0.66	0.70	0.78
$KGE_{SS}^{25\%}$	0.78	0.78	0.78	0.77	0.75	0.83	0.84	0.88
KGE_{SS}^{median}	0.86	0.86	0.86	0.86	0.86	0.87	0.89	0.92
$KGE_{SS}^{75\%}$	0.89	0.89	0.89	0.89	0.90	0.92	0.92	0.95
$KGE_{SS}^{95\%}$	0.92	0.92	0.92	0.92	0.94	0.95	0.96	0.96
Par No.	18	27	36	45	22	39	60	85
Model Names	$MN_{None}^{DSR}(2)$	$MN_{None}^{DSR}(3)$	$MN_{None}^{DSR}(4)$	$MN_{None}^{DSR}(5)$	$MN_{SALO}^{DSR}(2)$	$MN_{SALO}^{DSR}(3)$	$MN_{SALO}^{DSR}(4)$	$MN_{SALO}^{DSR}(5)$
KGE_{SS}^{min}	0.57	0.58	0.58	0.58	0.63	0.72	0.74	0.76
$KGE_{SS}^{5\%}$	0.64	0.62	0.62	0.62	0.68	0.75	0.81	0.80
$KGE_{SS}^{25\%}$	0.77	0.76	0.76	0.76	0.80	0.82	0.88	0.88
KGE_{SS}^{median}	0.86	0.86	0.86	0.86	0.86	0.88	0.91	0.92
$KGE_{SS}^{75\%}$	0.89	0.89	0.89	0.89	0.89	0.92	0.93	0.94
$KGE_{SS}^{95\%}$	0.92	0.92	0.92	0.92	0.94	0.94	0.96	0.95
Par No.	18	27	36	45	22	39	60	85
Model Names	$MN_{None}^{DS-MLB}(2)$	$MN_{None}^{DS-MLB}(3)$	$MN_{None}^{DS-MLB}(4)$	$MN_{None}^{DS-MLB}(5)$	$MN_{SALO}^{DS-MLB}(2)$	$MN_{SALO}^{DS-MLB}(3)$	$MN_{SALO}^{DS-MLB}(4)$	$MN_{SALO}^{DS-MLB}(5)$
KGE_{SS}^{min}	0.57	0.56	0.55	0.57	0.70	0.69	0.71	0.76
$KGE_{SS}^{5\%}$	0.61	0.61	0.58	0.59	0.74	0.73	0.80	0.80
$KGE_{SS}^{25\%}$	0.80	0.80	0.79	0.79	0.84	0.84	0.88	0.88
KGE_{SS}^{median}	0.86	0.85	0.86	0.86	0.87	0.89	0.92	0.91
$KGE_{SS}^{75\%}$	0.90	0.89	0.90	0.90	0.89	0.93	0.94	0.93
$KGE_{SS}^{95\%}$	0.92	0.91	0.91	0.91	0.95	0.95	0.96	0.97
Par No.	19	28	37	46	23	40	61	86
Model Names	$LSTM(2)$	$LSTM(3)$	$LSTM(4)$	$LSTM(5)$	$LSTM(2)$	$LSTM(3)$	$LSTM(4)$	$LSTM(5)$
KGE_{SS}^{min}	0.68	0.66	0.69	0.66	0.68	0.66	0.69	0.66
$KGE_{SS}^{5\%}$	0.72	0.75	0.76	0.78	0.72	0.75	0.76	0.78
$KGE_{SS}^{25\%}$	0.83	0.84	0.84	0.85	0.83	0.84	0.84	0.85
KGE_{SS}^{median}	0.87	0.88	0.89	0.90	0.87	0.88	0.89	0.90
$KGE_{SS}^{75\%}$	0.92	0.93	0.93	0.93	0.92	0.93	0.93	0.93
$KGE_{SS}^{95\%}$	0.95	0.96	0.96	0.98	0.95	0.96	0.96	0.98
Par No.	43	76	117	166	43	76	117	166

Table 4. KGE_{SS} Statistics and Numbers of Parameter for cases used for the benchmark comparison

Model Names	MA_3	MA_4	MA_5	MA_6	MA_{3-SAO}	MA_{4-SAO}	MA_{5-SAO}	MA_{6-SAO}	$MN_{None}^{DS}(2,0,0)$	$MN_{None}^{DS}(3,0,0)$
KGE_{SS}^{min}	0.30	0.58	0.58	0.57	0.57	0.59	0.65	0.57	0.60	0.62
$KGE_{SS}^{5\%}$	0.46	0.60	0.59	0.62	0.59	0.61	0.66	0.59	0.67	0.69
$KGE_{SS}^{25\%}$	0.75	0.79	0.77	0.81	0.80	0.81	0.82	0.83	0.78	0.78
KGE_{SS}^{median}	0.82	0.86	0.84	0.86	0.86	0.86	0.87	0.88	0.86	0.86
$KGE_{SS}^{75\%}$	0.87	0.90	0.88	0.91	0.90	0.91	0.90	0.92	0.89	0.89
$KGE_{SS}^{95\%}$	0.91	0.94	0.92	0.94	0.94	0.95	0.95	0.96	0.92	0.92
Par No.	11	14	18	21	13	16	24	27	18	27
Model Names	$MN_{None}^{DS}(3,3,0)$	$MN_{None}^{DSR}(2,1,0)$	$MN_{None}^{DSR}(3,1,0)$	$MN_{None}^{DS-MLB}(2,3,0)$	$MN_{SALO}^{DS}(5,0,0)$	$MN_{SALO}^{DSR}(5,0,0)$	$MN_{SALO}^{DS-MLB}(5,0,0)$	$LSTM(5)$	$LSTM(6)$	$LSTM(5,5,5)$
KGE_{SS}^{min}	0.72	0.72	0.65	0.75	0.73	0.76	0.76	0.66	0.68	0.59
$KGE_{SS}^{5\%}$	0.74	0.73	0.69	0.77	0.78	0.80	0.80	0.78	0.78	0.66
$KGE_{SS}^{25\%}$	0.84	0.82	0.82	0.80	0.88	0.88	0.88	0.85	0.84	0.87
KGE_{SS}^{median}	0.87	0.85	0.86	0.84	0.92	0.92	0.91	0.90	0.90	0.91
$KGE_{SS}^{75\%}$	0.90	0.90	0.91	0.89	0.95	0.94	0.93	0.93	0.93	0.93
$KGE_{SS}^{95\%}$	0.94	0.93	0.94	0.92	0.96	0.95	0.97	0.98	0.96	0.97
Par No.	60	27	36	50	85	85	86	166	223	486



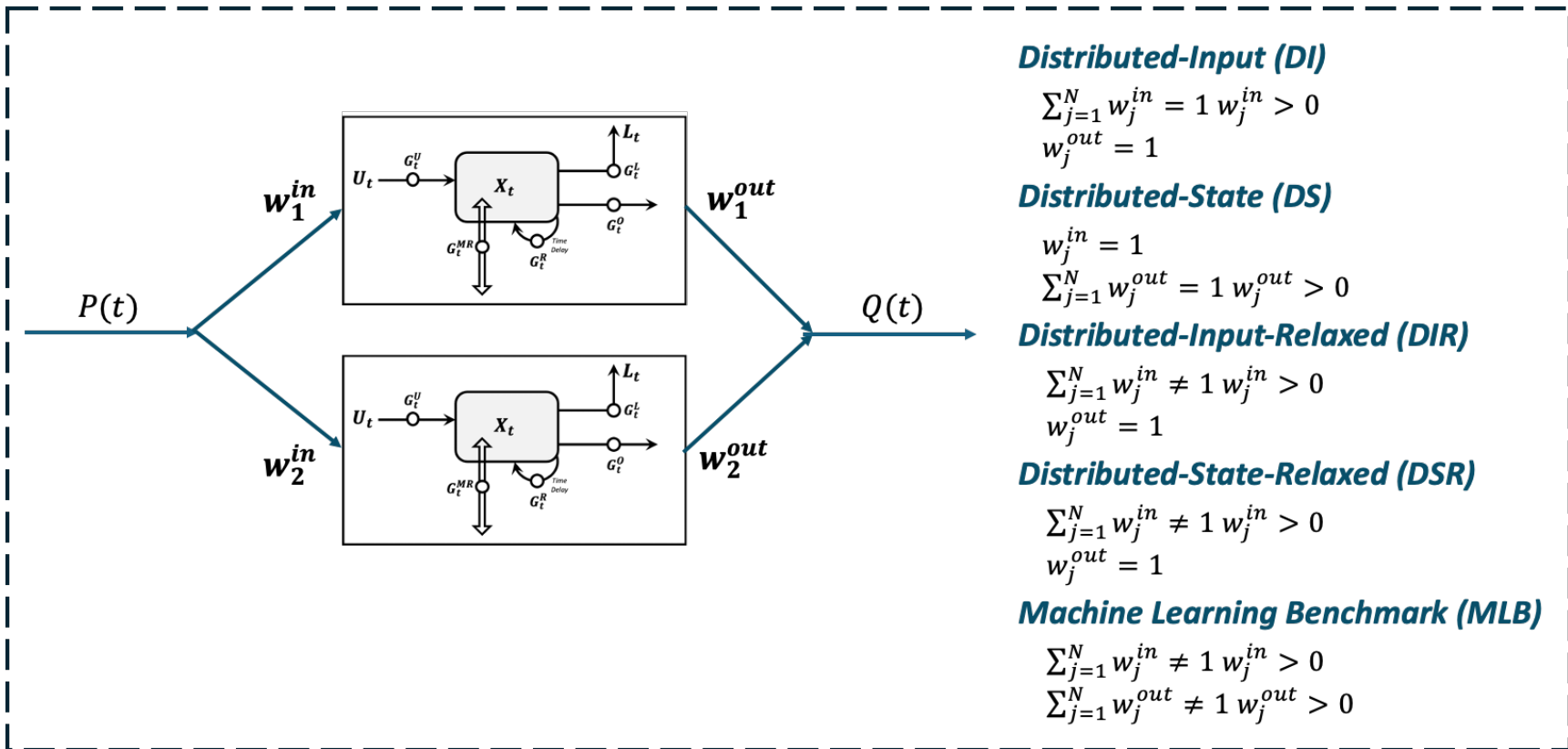


Figure 2: Illustrative representations of various types of Mass-Conserving Networks (MNs) utilized in this study.

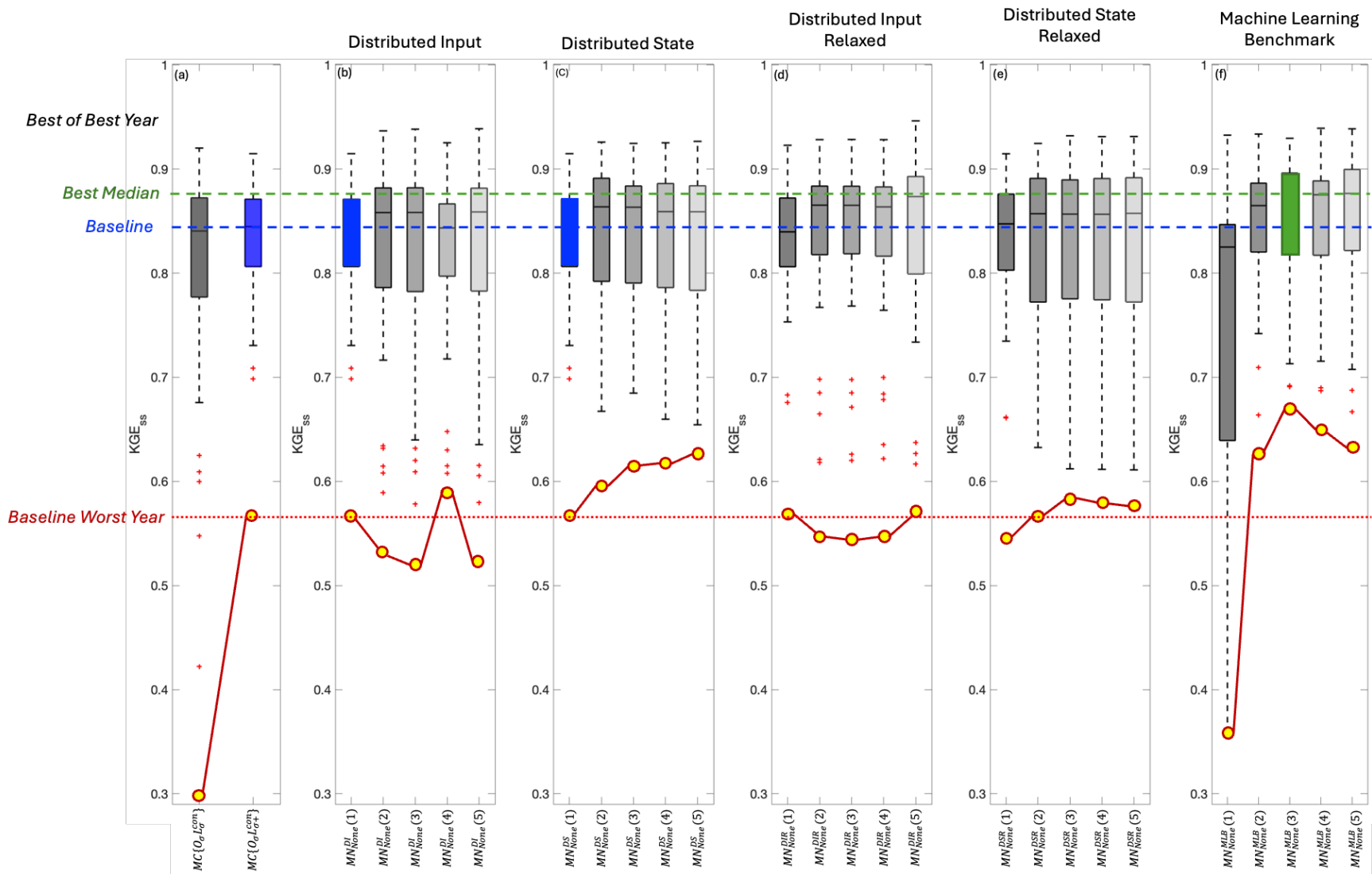


Figure 3: Box and whisker plots of the distributions of annual KGE scores for network performance, including (a) single MCP nodes, and the single-layer network cases: (b) Distributed Input (DI), (c) Distributed State (DS), (d) Distributed Input Relaxed (DIR), and (e) Distributed State Relaxed (DSR), with the number of nodes varying from 1 to 5.

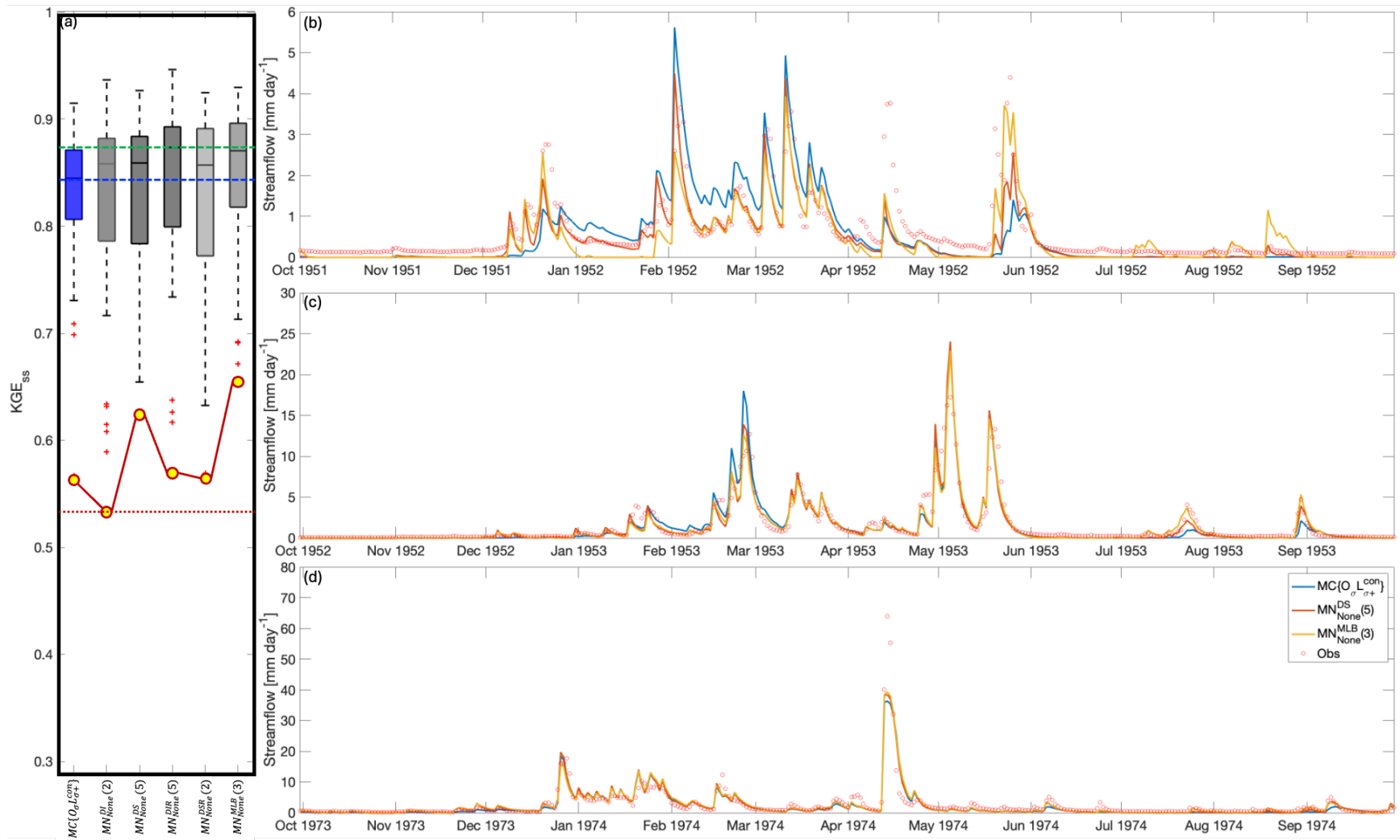


Figure 4: Comparison of selected single-layer Mass-Conserving Network performance using (a) box and whisker plots showing the distributions of annual KGE scores, and the associated hydrographs for selected dry, median, and wet years in subplots (b) to (d).

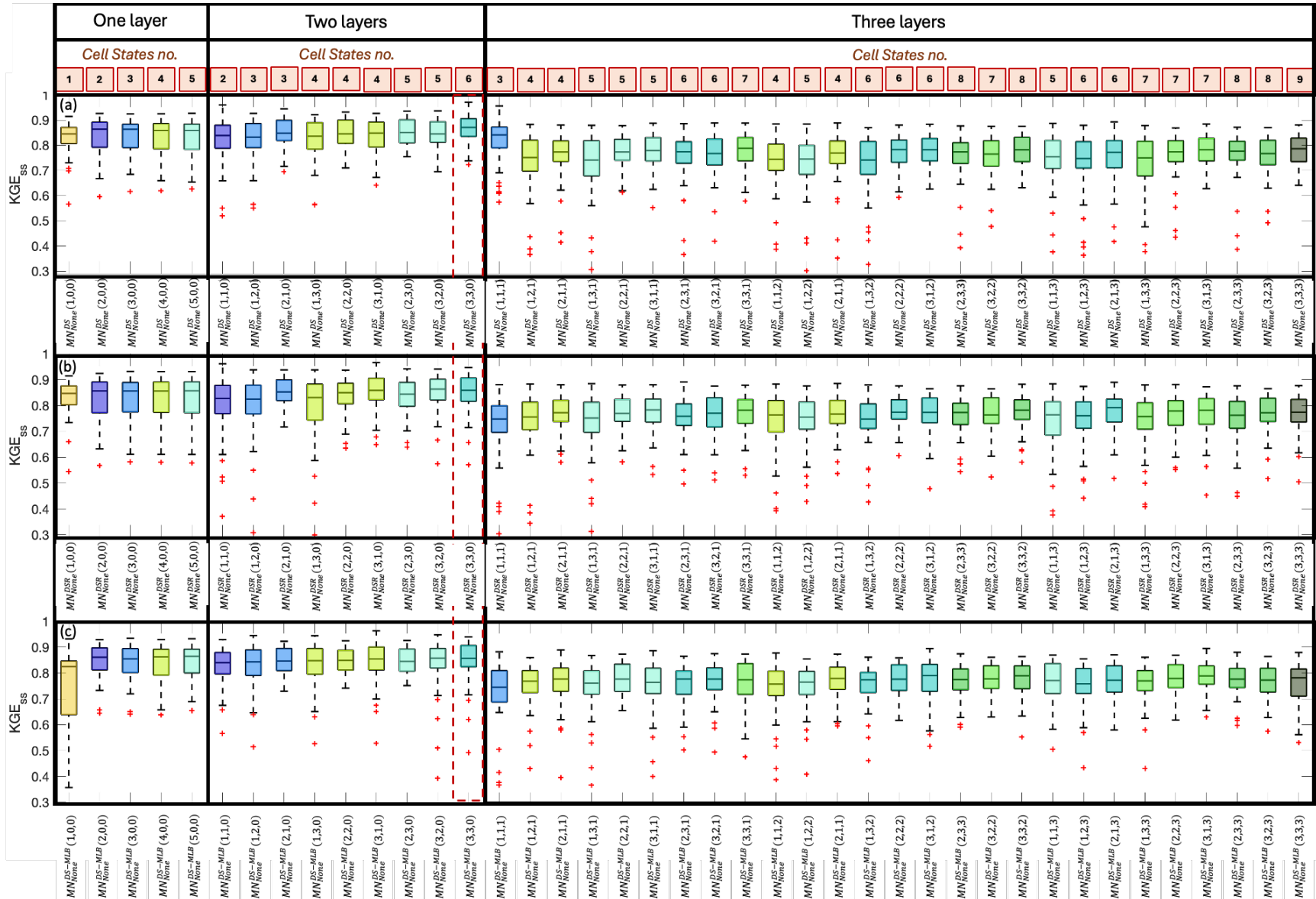


Figure 5: Box and whisker plots of the distributions of annual KGE_{ss} values for the performance of Single- and Multi-Layer Networks, including (a) Distributed-State (DS), (b) Distributed-State Relaxation (DSR), and (c) Distributed-State Machine Learning Benchmark. Each network architecture includes 41 cases, with the number of nodes in the first layer varying from 1 to 3, and in the second and third layers from 0 to 3. Single-layer cases with 4 and 5 nodes are also included for comparison.

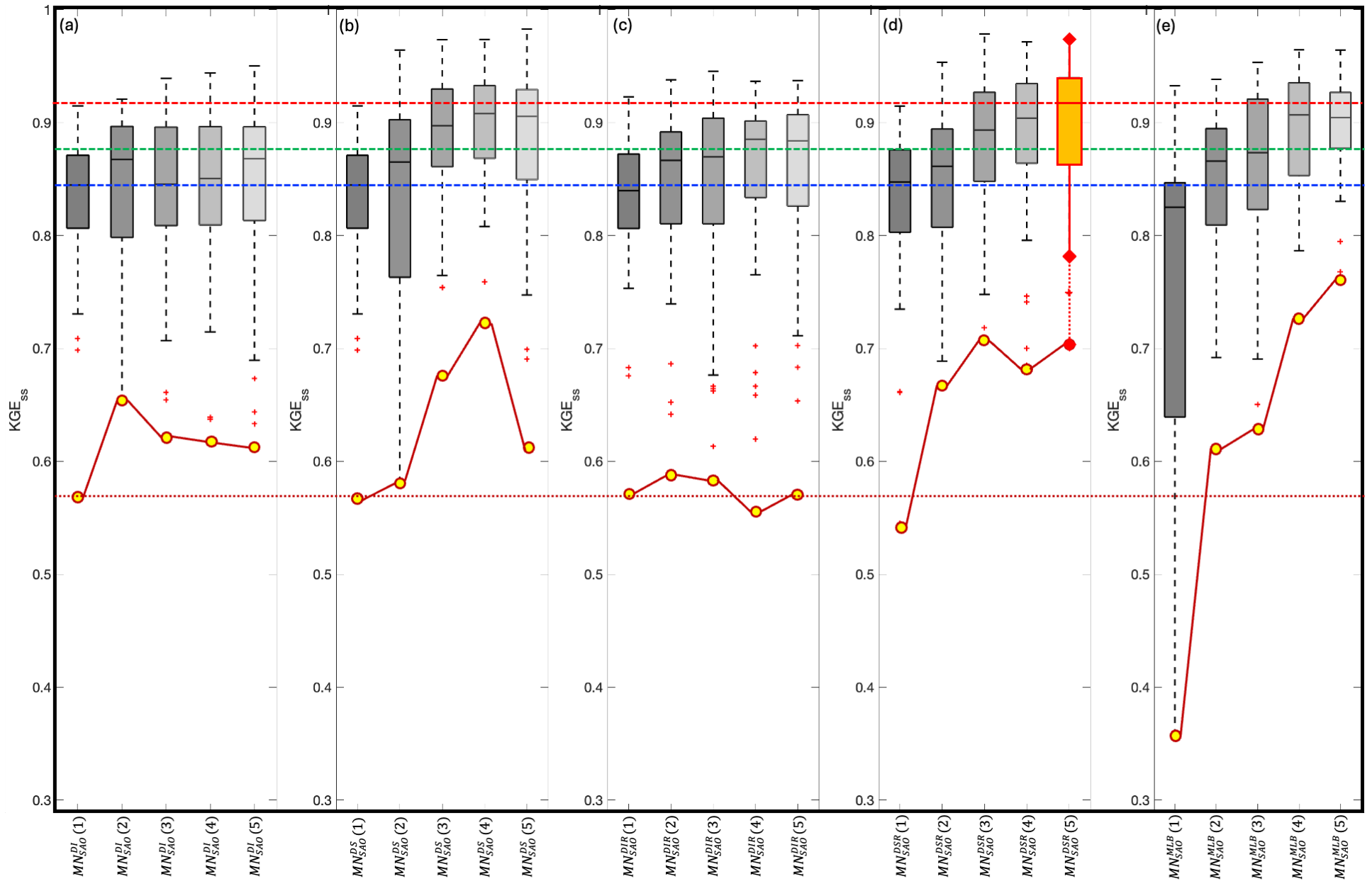


Figure 6: Box and whisker plots of the distributions of annual KGE_{ss} values for single-layer Sharing-Augmented Output Gates (SAO) networks, including (a) Distributed Input (DI), (b) Distributed State (DS), (c) Distributed Input Relaxed (DIR), (d) Distributed State Relaxed (DSR), and (e) Machine-Learning Benchmark (MLB). The number of nodes varies from 1 to 5

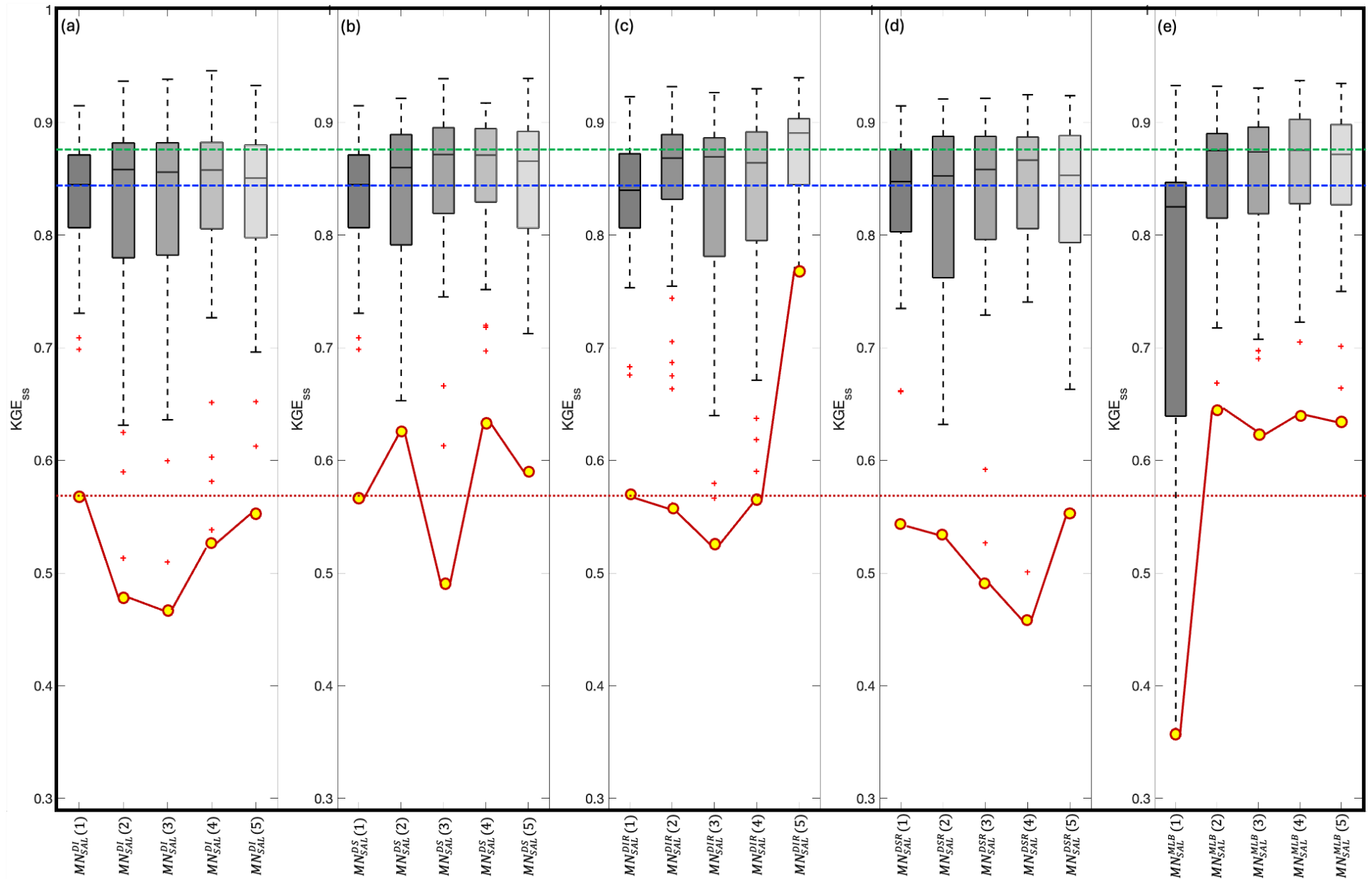


Figure 7: Box and whisker plots of the distributions of annual KGE_{ss} values for single-layer Sharing-Augmented Loss Gates (SAL) networks, including (a) Distributed Input (DI), (b) Distributed State (DS), (c) Distributed Input Relaxed (DIR), (d) Distributed State Relaxed (DSR), and (e) Machine-Learning Benchmark (MLB). The number of nodes varies from 1 to 5.

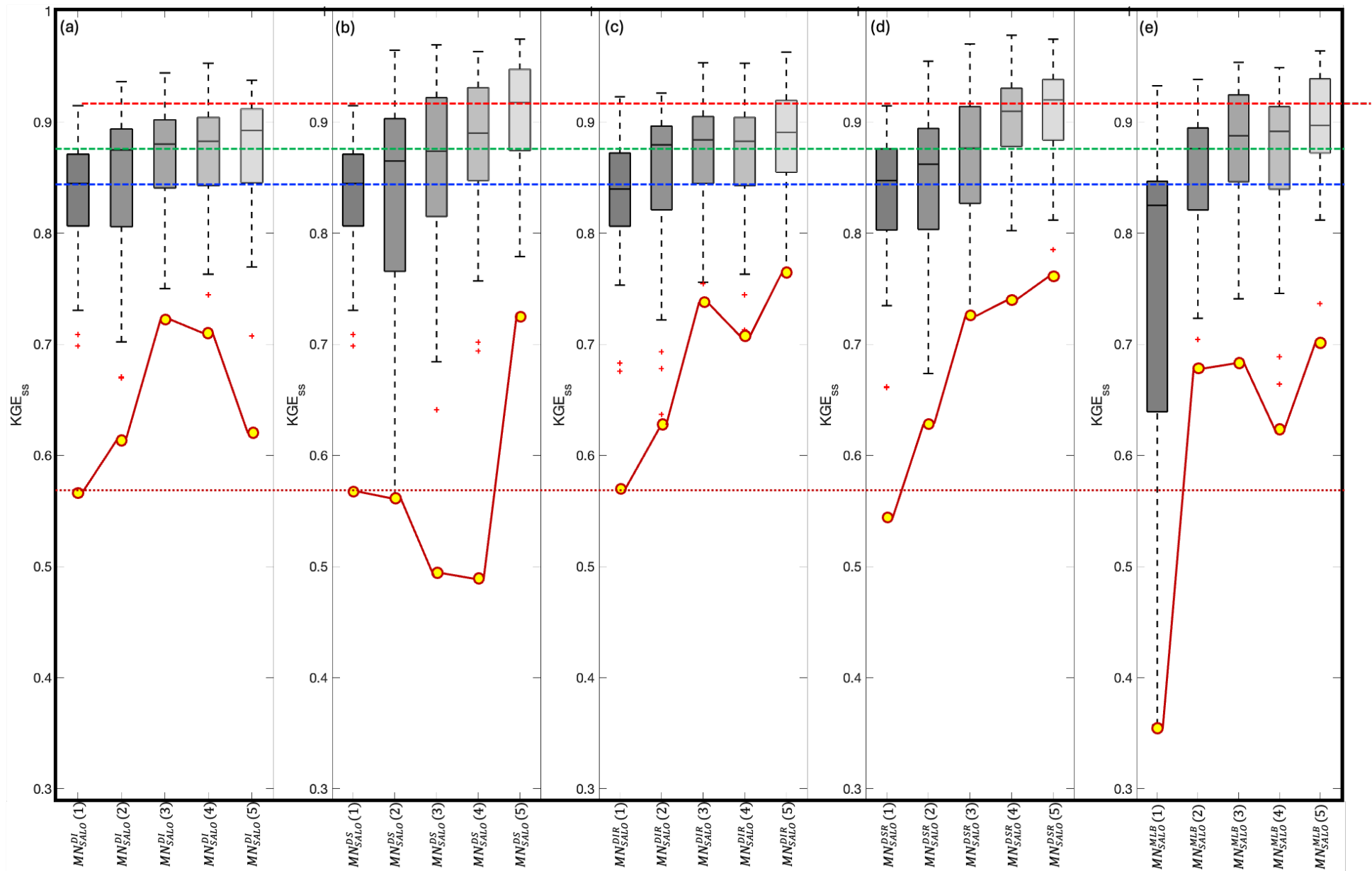


Figure 8: Box and whisker plots of the distributions of annual KGE_{ss} values for single-layer Sharing-Augmented Loss & Output Gates (SALO) networks, including (a) Distributed Input (DI), (b) Distributed State (DS), (c) Distributed Input Relaxed (DIR), (d) Distributed State Relaxed (DSR), and (e) Machine-Learning Benchmark (MLB). The number of nodes varies from 1 to 5.

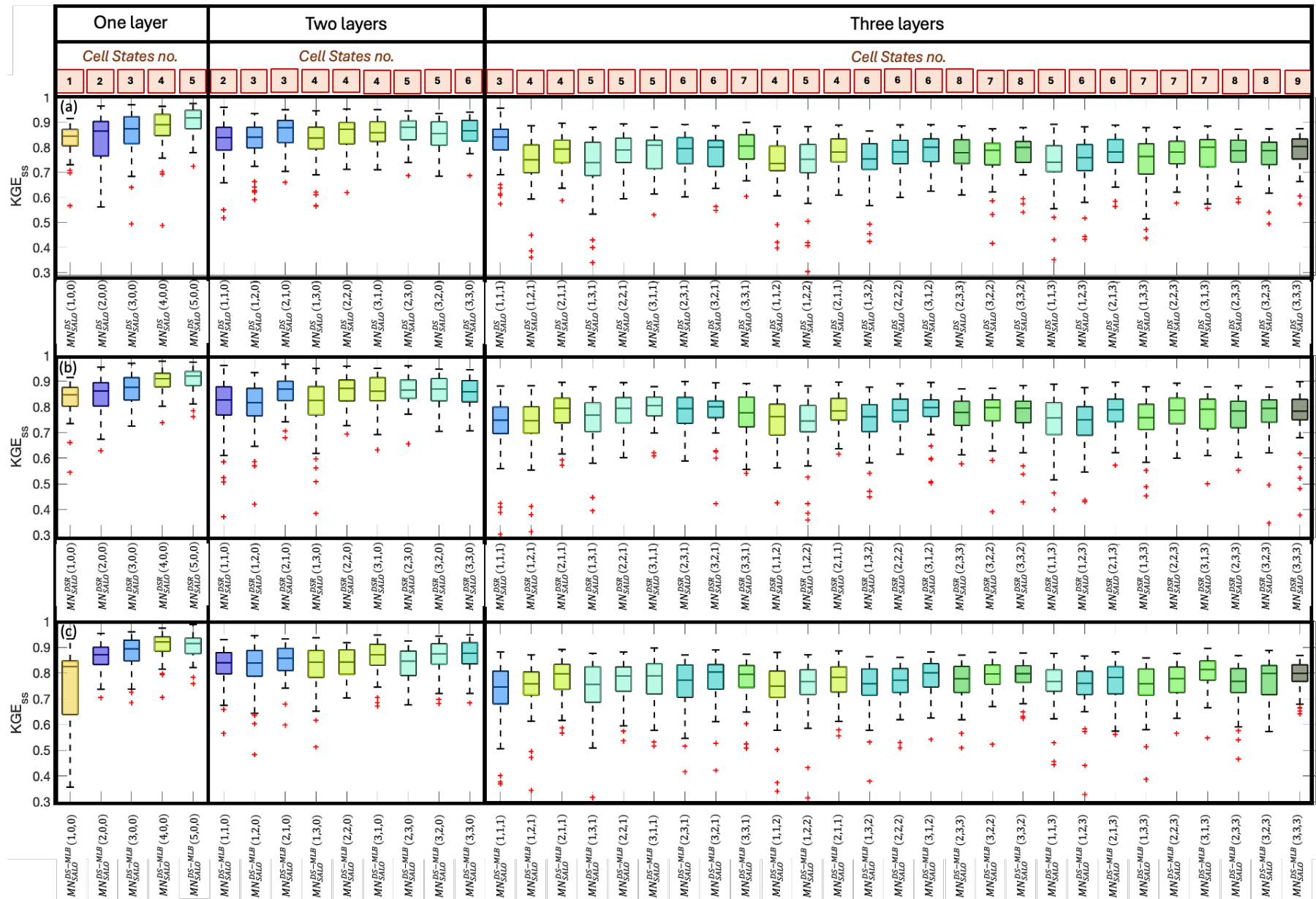


Figure 9: Box and whisker plots of the distributions of annual KGESs values for the performance of Single- and Multi-Layer Sharing-Augmented Loss & Output Gates Networks, including (a) Distributed-State (DS), (b) Distributed-State Relaxation (DSR), and (c) Distributed-State Machine Learning Benchmark Case. Each network architecture includes 41 cases, with the number of nodes in the first layer varying from 1 to 3, and in the second and third layers from 0 to 3. Cases with a single layer and 4 or 5 nodes are also included for comparison.

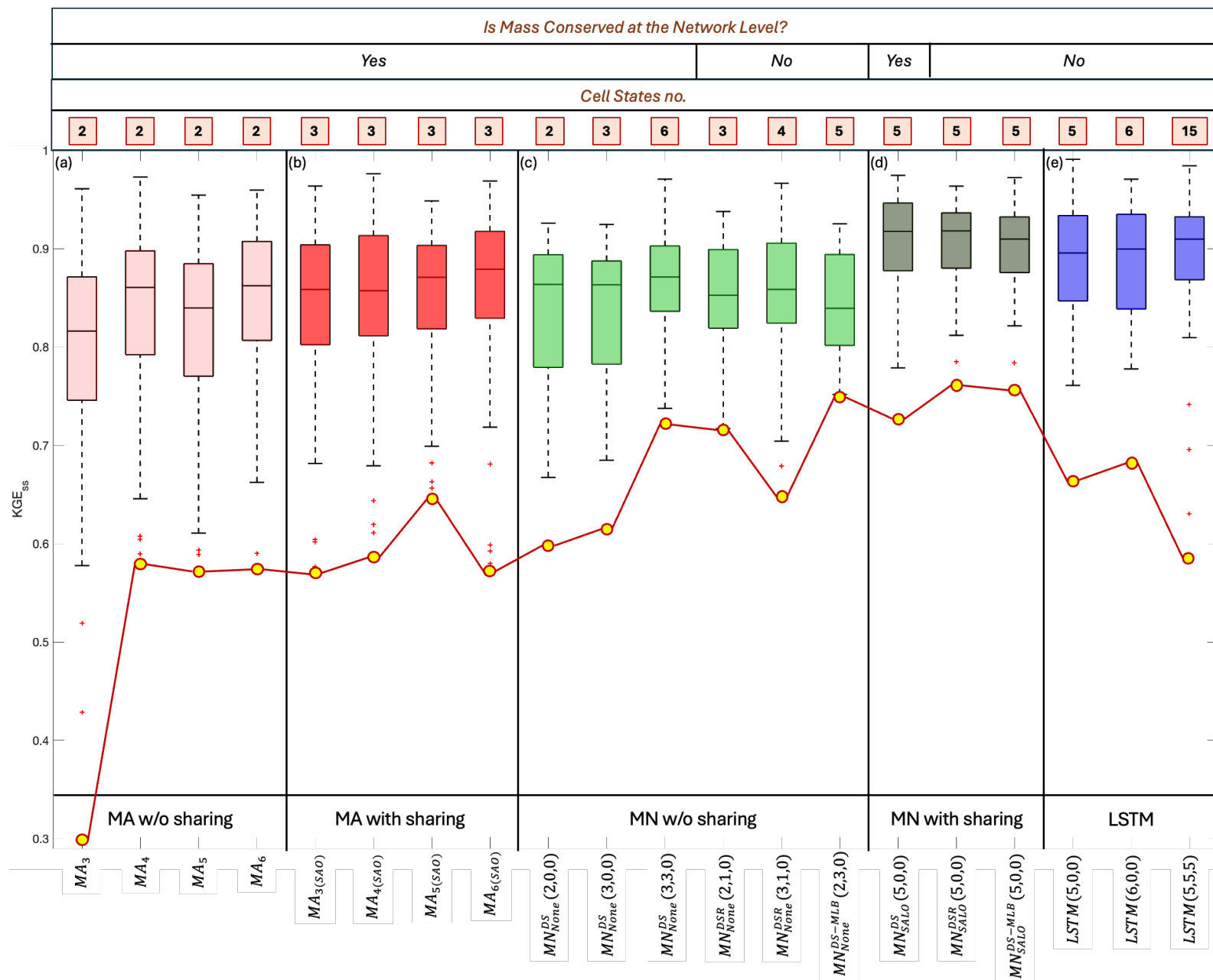


Figure 10: Box and whisker plots of the distributions of annual KGE scores, comparing (a) Mass-Conserving Architectures (MAs) reported in Wang & Gupta (2024b), (b) associated MAs with Sharing-Augmented Output Gates, (c) several selected mass-conserving neural networks (MNs) developed in the current study, and (d) the associated architectures with Sharing-Augmented output or loss gates (or both), also developed in this study, along with LSTM networks with varying numbers of layers and nodes.

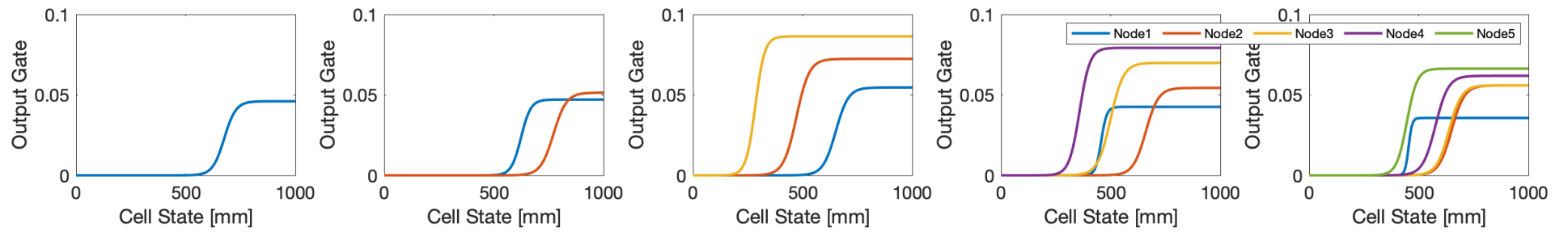


Figure 11: The output gate function for the distributed-state (DS) case ($MN_{None}^{DS}(N)$) is shown, with subplots (a) to (e) illustrating the variation in the number of nodes (N) from 1 to 5. The color coding represents the peak value of each gate.

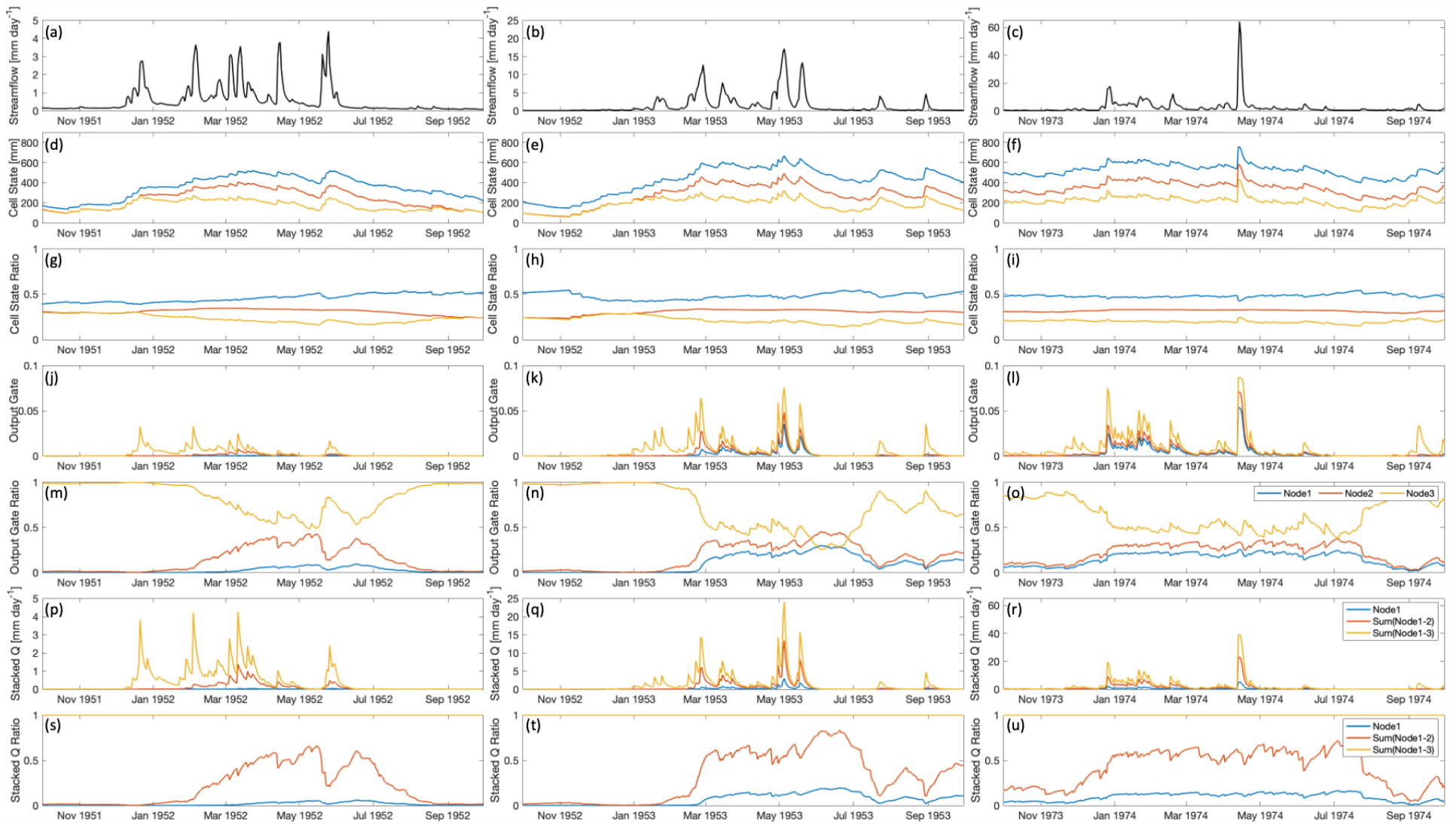


Figure 12: Time series plots of streamflow observations for dry, median, and wet years are shown in subplots (a) to (c). The results for the single-layer three-node distributed case ($MN_{None}^{DS}(3)$) are presented with these three years including cell state in subplots (d) to (f), cell state ratio in subplots (g) to (i), output gate series in subplots (j) to (l), output gate ratio in subplots (m) to (o), streamflow accumulated from each node in subplots (p) to (r), and the ratio for the streamflow accumulated from each node in subplots (s) to (u). Q=streamflow

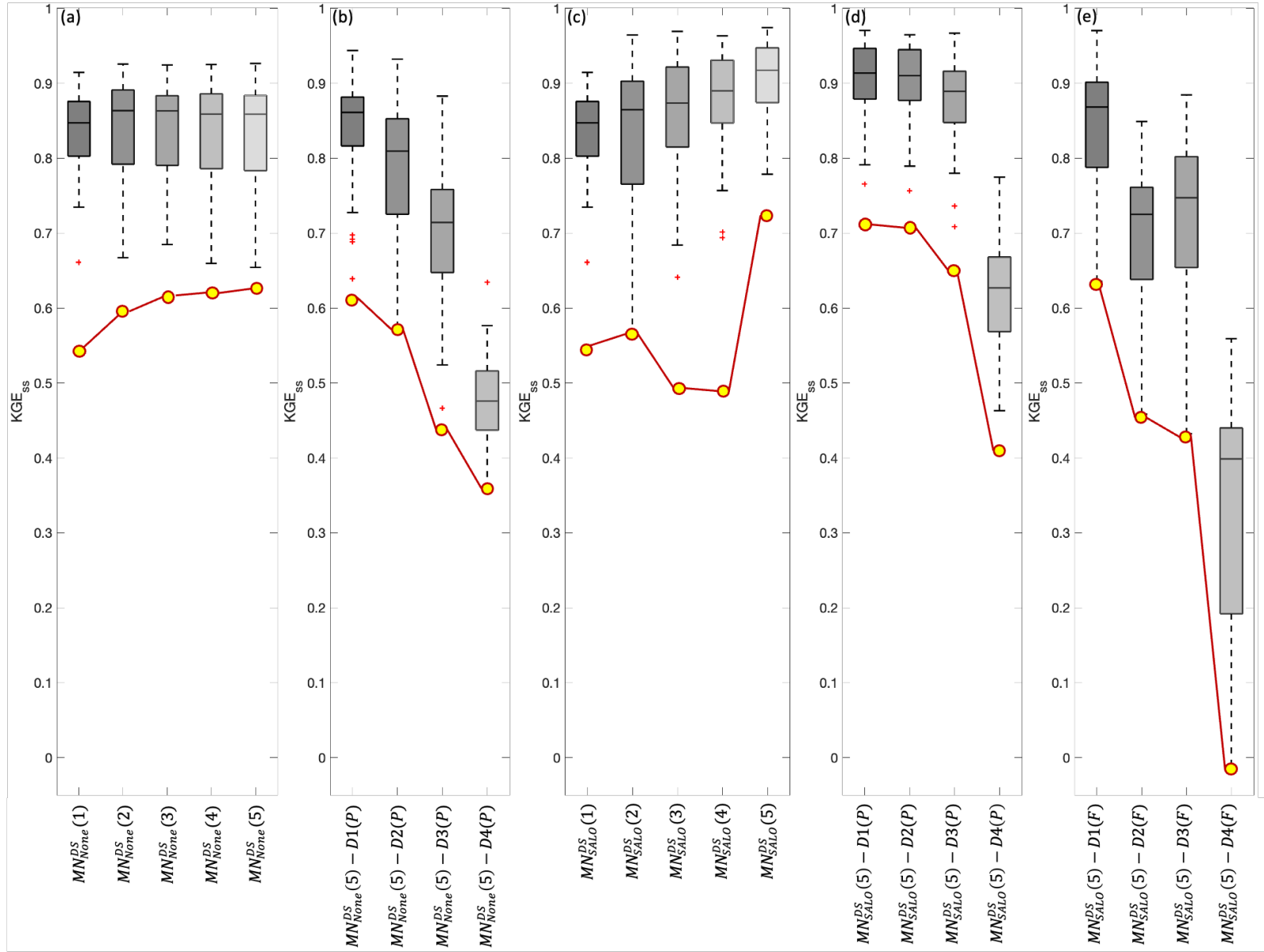


Figure 13: Box and whisker plots of the distributions of annual KGE_{ss} values for (a) single-layer distributed state (DS) case ($MN_{None}^{DS}(N)$) with node number (N) varies from 1 to 5, (b) the $MN_{None}^{DS}(5)$ network with pruning 1 to 4 flow paths ($MN_{None}^{DS}(5) - D1(P)$ to $MN_{None}^{DS}(5) - D4(P)$), (c) single-layer distributed state (DS) Sharing-Augmented Loss & Output Gates (SALO) networks with node number (N) varies from 1 to 5, (d) the $MN_{SALO}^{DS}(5)$ network with pruning 1 to 4 flow paths ($MN_{SALO}^{DS}(5) - D1(P)$ to $MN_{SALO}^{DS}(5) - D4(P)$), and (e) the $MN_{SALO}^{DS}(5)$ network with pruning 1 to 4 flow paths ($MN_{SALO}^{DS}(5) - D1(F)$ to $MN_{SALO}^{DS}(5) - D4(F)$)

Supplementary Materials

Contents of this supplementary material:

Table S1 to S11
Figures S1 to S11

Introduction

This Supporting Information provides 8 supplementary tables, and 11 supplementary figures to support the discussions in the main text. The contents of these supplementary materials are as follows.

Table S1. α_*^{KGE} scores for the Single-Layer Mass-Conserving Neural Networks (MNs)

Table S2. β_*^{KGE} scores for the Single-Layer Mass-Conserving Neural Networks (MNs)

Table S3. γ^{KGE} scores for the Single-Layer Mass-Conserving Neural Networks (MNs)

Table S4. KGE_{SS} scores of flow magnitude for the Single-Layer Mass-Conserving Neural Networks (MNs)

Table S5. α^{KGE} scores of flow magnitude for the Single-Layer Mass-Conserving Neural Networks (MNs)

Table S6. β^{KGE} scores of flow magnitude for the Single-Layer Mass-Conserving Neural Networks (MNs)

Table S7. γ^{KGE} scores of flow magnitude for the Single-Layer Mass-Conserving Neural Networks (MNs)

Table S8. Summary of Multi-Layer Mass-Conserving Neural Network (MN_s) architectural hypothesis in this study

Table S9. Summary of benchmark models in this study

Table S10. KGE_{SS} statistics and numbers of parameter for the benchmark LSTM network used in this study

Table S11. Summary of the pruned network models in this study

Figure S1. Comparison of selected single-layer Mass-Conserving Network performance using hydrographs in log-scale for selected dry, median, and wet years in subplots (a) to (c).

Figure S2. Comparison of selected single-layer Mass-Conserving Network performance using the hydrographs for selected dry, median, and wet years in subplots (a) to (c).

Figure S3. Box and whisker plots of the distributions of annual KGE scores, comparing the (a) 1-layer, (b) 2-layer, and (c) 3-layer long short-term memory (LSTM) networks, with the number of nodes varying from 1 to 5.

Figure S4. Time series plots of streamflow observations for dry, median, and wet years are shown in subplots (a) to (c). The cell states for the distributed case (DS) are presented with 1-node in subplots (d) to (f) (dry, median, and wet years), 2-node in subplots (g) to (i), 3-node in subplots (j) to (l), 4-node in subplots (m) to (o), and 5-node in subplots (p) to (r).

Figure S5. Time series plots of streamflow observations for dry, median, and wet years are shown in subplots (a) to (c). The output gate series for the distributed case (DS) are presented with 1-node in subplots (d) to (f) (dry, median, and wet years), 2-node in subplots (g) to (i), 3-node in subplots (j) to (l), 4-node in subplots (m) to (o), and 5-node in subplots (p) to (r).

Figure S6. Time series plots of streamflow observations for dry, median, and wet years are shown in subplots (a) to (c). The streamflow components for the distributed case (DS) are presented with 1-node in subplots (d) to (f) (dry, median, and wet years), 2-node in subplots (g) to (i), 3-node in subplots (j) to (l), 4-node in subplots (m) to (o), and 5-node in subplots (p) to (r).

Figure S7. Time series plots of streamflow observations for dry, median, and wet years are shown in subplots (a) to (c). The cumulative streamflow components for the distributed case (DS) are presented with 1-node in subplots (d) to (f) (dry, median, and wet years), 2-node in subplots (g) to (i), 3-node in subplots (j) to (l), 4-node in subplots (m) to (o), and 5-node in subplots (p) to (r).

Figure S8. Time series plots of streamflow observations for dry, median, and wet years are shown in subplots (a) to (c). The cell states ratio for the distributed case (DS) are presented with 1-node in subplots (d) to (f) (dry, median, and wet years), 2-node in subplots (g) to (i), 3-node in subplots (j) to (l), 4-node in subplots (m) to (o), and 5-node in subplots (p) to (r).

Figure S9. Time series plots of streamflow observations for dry, median, and wet years are shown in subplots (a) to (c). The ratio of output gate series for the distributed case (DS) are presented with 1-node in subplots (d) to (f) (dry, median, and wet years), 2-node in subplots (g) to (i), 3-node in subplots (j) to (l), 4-node in subplots (m) to (o), and 5-node in subplots (p) to (r).

Figure S10. Time series plots of streamflow observations for dry, median, and wet years are shown in subplots (a) to (c). The ratio of streamflow components for the distributed case (DS) are presented with 1-node in subplots (d) to (f) (dry, median, and wet years), 2-node in subplots (g) to (i), 3-node in subplots (j) to (l), 4-node in subplots (m) to (o), and 5-node in subplots (p) to (r).

Figure S11. Time series plots of streamflow observations for dry, median, and wet years are shown in subplots (a) to (c). The ratio of cumulative streamflow components for the distributed case (DS) are presented with 1-node in subplots (d) to (f) (dry, median, and wet years), 2-node in subplots (g) to (i), 3-node in subplots (j) to (l), 4-node in subplots (m) to (o), and 5-node in subplots (p) to (r).

Table S1. 1 – $|1 - \alpha^{KGE}|$ (α^{KGE}) scores for the Single-Layer Mass-Conserving Neural Networks (MNs)

1-Node																							
	MN_{none}^{DI}	MN_{none}^{DS}	MN_{none}^{DIR}	MN_{none}^{DSR}	MN_{none}^{MLB}		MN_{SAL}^{DI}	MN_{SAL}^{DS}	MN_{SAL}^{DIR}	MN_{SAL}^{DSR}	MN_{SAL}^{MLB}		MN_{SAO}^{DI}	MN_{SAO}^{DS}	MN_{SAO}^{DIR}	MN_{SAO}^{DSR}	MN_{SAO}^{MLB}		MN_{SALO}^{DI}	MN_{SALO}^{DS}	MN_{SALO}^{DIR}	MN_{SALO}^{DSR}	MN_{SALO}^{MLB}
KGE_{ss}^{min}	0.60	0.60	0.60	0.57	0.40	KGE_{ss}^{min}							KGE_{ss}^{min}						KGE_{ss}^{min}				
$KGE_{ss}^{5\%}$	0.73	0.72	0.73	0.70	0.51	$KGE_{ss}^{5\%}$							$KGE_{ss}^{5\%}$						$KGE_{ss}^{5\%}$				
$KGE_{ss}^{25\%}$	0.83	0.82	0.83	0.83	0.74	$KGE_{ss}^{25\%}$							$KGE_{ss}^{25\%}$						$KGE_{ss}^{25\%}$				
$KGE_{ss}^{50\%}$	0.89	0.88	0.89	0.90	0.91	$KGE_{ss}^{50\%}$							$KGE_{ss}^{50\%}$						$KGE_{ss}^{50\%}$				
$KGE_{ss}^{75\%}$	0.93	0.93	0.93	0.94	0.97	$KGE_{ss}^{75\%}$							$KGE_{ss}^{75\%}$						$KGE_{ss}^{75\%}$				
$KGE_{ss}^{95\%}$	0.98	0.99	0.98	0.98	0.99	$KGE_{ss}^{95\%}$							$KGE_{ss}^{95\%}$						$KGE_{ss}^{95\%}$				
PNs	8	8	9	9	11	PNs							PNs						PNs				
2-Node																							
KGE_{ss}^{min}	0.58	0.61	0.56	0.59	0.67	KGE_{ss}^{min}	0.59	0.65	0.58	0.61	0.69	KGE_{ss}^{min}	0.60	0.62	0.61	0.70	0.65	KGE_{ss}^{min}	0.63	0.60	0.69	0.68	0.73
$KGE_{ss}^{5\%}$	0.66	0.70	0.67	0.69	0.71	$KGE_{ss}^{5\%}$	0.59	0.68	0.71	0.68	0.73	$KGE_{ss}^{5\%}$	0.73	0.66	0.69	0.72	0.70	$KGE_{ss}^{5\%}$	0.70	0.67	0.70	0.71	0.74
$KGE_{ss}^{25\%}$	0.79	0.82	0.82	0.79	0.85	$KGE_{ss}^{25\%}$	0.79	0.82	0.82	0.77	0.84	$KGE_{ss}^{25\%}$	0.82	0.80	0.84	0.85	0.83	$KGE_{ss}^{25\%}$	0.83	0.80	0.85	0.85	0.85
$KGE_{ss}^{50\%}$	0.89	0.91	0.90	0.89	0.92	$KGE_{ss}^{50\%}$	0.89	0.88	0.89	0.89	0.92	$KGE_{ss}^{50\%}$	0.91	0.91	0.90	0.91	0.92	$KGE_{ss}^{50\%}$	0.91	0.91	0.90	0.91	0.92
$KGE_{ss}^{75\%}$	0.94	0.95	0.96	0.95	0.95	$KGE_{ss}^{75\%}$	0.94	0.95	0.96	0.95	0.95	$KGE_{ss}^{75\%}$	0.94	0.97	0.96	0.94	0.96	$KGE_{ss}^{75\%}$	0.95	0.96	0.97	0.94	0.97
$KGE_{ss}^{95\%}$	0.98	0.99	0.99	0.98	0.99	$KGE_{ss}^{95\%}$	0.98	0.98	0.99	0.98	0.99	$KGE_{ss}^{95\%}$	0.97	0.99	0.99	0.99	0.99	$KGE_{ss}^{95\%}$	0.99	0.99	0.99	0.98	0.99
PNs	18	18	18	18	21	PNs	20	20	20	20	23	PNs	20	20	20	20	23	PNs	22	22	22	22	25
3-Node																							
KGE_{ss}^{min}	0.58	0.65	0.56	0.62	0.67	KGE_{ss}^{min}	0.58	0.57	0.55	0.55	0.69	KGE_{ss}^{min}	0.64	0.70	0.61	0.73	0.64	KGE_{ss}^{min}	0.70	0.48	0.71	0.75	0.64
$KGE_{ss}^{5\%}$	0.64	0.69	0.67	0.65	0.73	$KGE_{ss}^{5\%}$	0.59	0.64	0.63	0.68	0.72	$KGE_{ss}^{5\%}$	0.69	0.76	0.66	0.76	0.73	$KGE_{ss}^{5\%}$	0.74	0.65	0.77	0.78	0.77
$KGE_{ss}^{25\%}$	0.79	0.82	0.82	0.78	0.83	$KGE_{ss}^{25\%}$	0.80	0.84	0.80	0.80	0.83	$KGE_{ss}^{25\%}$	0.83	0.89	0.80	0.88	0.86	$KGE_{ss}^{25\%}$	0.86	0.83	0.87	0.86	0.87
$KGE_{ss}^{50\%}$	0.89	0.89	0.90	0.88	0.90	$KGE_{ss}^{50\%}$	0.89	0.90	0.91	0.89	0.92	$KGE_{ss}^{50\%}$	0.88	0.93	0.90	0.93	0.93	$KGE_{ss}^{50\%}$	0.91	0.91	0.94	0.93	0.94
$KGE_{ss}^{75\%}$	0.94	0.95	0.95	0.94	0.97	$KGE_{ss}^{75\%}$	0.94	0.95	0.94	0.95	0.98	$KGE_{ss}^{75\%}$	0.96	0.98	0.97	0.97	0.96	$KGE_{ss}^{75\%}$	0.97	0.96	0.96	0.96	0.98
$KGE_{ss}^{95\%}$	0.99	0.98	0.99	0.98	1.00	$KGE_{ss}^{95\%}$	0.98	0.98	0.99	0.99	1.00	$KGE_{ss}^{95\%}$	1.00	1.00	1.00	1.00	0.99	$KGE_{ss}^{95\%}$	0.99	0.99	1.00	0.99	1.00
PNs	27	27	27	27	31	PNs	33	33	33	33	37	PNs	33	33	33	33	37	PNs	39	39	39	39	43
4-Node																							
KGE_{ss}^{min}	0.54	0.63	0.56	0.61	0.66	KGE_{ss}^{min}	0.60	0.64	0.59	0.52	0.69	KGE_{ss}^{min}	0.62	0.74	0.59	0.69	0.70	KGE_{ss}^{min}	0.75	0.54	0.75	0.76	0.61
$KGE_{ss}^{5\%}$	0.66	0.67	0.68	0.65	0.71	$KGE_{ss}^{5\%}$	0.61	0.72	0.63	0.66	0.74	$KGE_{ss}^{5\%}$	0.68	0.76	0.64	0.76	0.79	$KGE_{ss}^{5\%}$	0.79	0.71	0.79	0.80	0.71
$KGE_{ss}^{25\%}$	0.82	0.82	0.82	0.80	0.82	$KGE_{ss}^{25\%}$	0.81	0.84	0.81	0.84	0.83	$KGE_{ss}^{25\%}$	0.83	0.89	0.85	0.90	0.88	$KGE_{ss}^{25\%}$	0.88	0.89	0.88	0.91	0.86
$KGE_{ss}^{50\%}$	0.88	0.88	0.90	0.89	0.91	$KGE_{ss}^{50\%}$	0.89	0.91	0.90	0.90	0.92	$KGE_{ss}^{50\%}$	0.90	0.94	0.91	0.94	0.94	$KGE_{ss}^{50\%}$	0.92	0.94	0.92	0.94	0.92
$KGE_{ss}^{75\%}$	0.93	0.94	0.94	0.94	0.96	$KGE_{ss}^{75\%}$	0.95	0.95	0.96	0.95	0.95	$KGE_{ss}^{75\%}$	0.96	0.97	0.96	0.97	0.97	$KGE_{ss}^{75\%}$	0.96	0.97	0.96	0.97	0.95
$KGE_{ss}^{95\%}$	0.98	0.98	0.99	0.98	0.99	$KGE_{ss}^{95\%}$	0.98	0.99	1.00	0.99	0.98	$KGE_{ss}^{95\%}$	0.99	0.99	0.99	0.99	0.99	$KGE_{ss}^{95\%}$	0.98	0.99	0.98	1.00	1.00
PNs	36	36	36	36	41	PNs	48	48	48	48	53	PNs	48	48	48	48	53	PNs	60	60	60	60	65
5-Node																							
KGE_{ss}^{min}	0.58	0.63	0.60	0.61	0.66	KGE_{ss}^{min}	0.62	0.62	0.77	0.61	0.65	KGE_{ss}^{min}	0.62	0.62	0.66	0.69	0.76	KGE_{ss}^{min}	0.62	0.68	0.71	0.72	0.73
$KGE_{ss}^{5\%}$	0.65	0.67	0.65	0.65	0.69	$KGE_{ss}^{5\%}$	0.72	0.71	0.81	0.72	0.72	$KGE_{ss}^{5\%}$	0.66	0.71	0.68	0.74	0.80	$KGE_{ss}^{5\%}$	0.72	0.75	0.81	0.79	0.76
$KGE_{ss}^{25\%}$	0.79	0.82	0.80	0.79	0.81	$KGE_{ss}^{25\%}$	0.83	0.85	0.90	0.81	0.86	$KGE_{ss}^{25\%}$	0.83	0.89	0.84	0.87	0.91	$KGE_{ss}^{25\%}$	0.87	0.89	0.88	0.90	0.89
$KGE_{ss}^{50\%}$	0.89	0.88	0.92	0.89	0.92	$KGE_{ss}^{50\%}$	0.87	0.89	0.93	0.89	0.93	$KGE_{ss}^{50\%}$	0.91	0.94	0.92	0.96	0.94	$KGE_{ss}^{50\%}$	0.92	0.96	0.92	0.95	0.95
$KGE_{ss}^{75\%}$	0.94	0.94	0.95	0.95	0.97	$KGE_{ss}^{75\%}$	0.91	0.95	0.94	0.94	0.96	$KGE_{ss}^{75\%}$	0.96	0.98	0.96	0.97	0.98	$KGE_{ss}^{75\%}$	0.97	0.98	0.97	0.97	0.97
$KGE_{ss}^{95\%}$	0.99	0.98	0.99	0.99	0.99	$KGE_{ss}^{95\%}$	0.97	0.97	0.99	0.99	0.99	$KGE_{ss}^{95\%}$	0.99	0.99	0.99	0.99	0.99	$KGE_{ss}^{95\%}$	1.00	0.99	1.00	0.99	1.00
PNs	45	45	45	45	51	PNs	65	65	65	65	71	PNs	65	65	65	65	71	PNs	85	85	85	85	91

Table S2. 1 – $|1 - \beta^{KGE}|$ (β_s^{KGE}) scores for the Single-Layer Mass-Conserving Neural Networks (MNs)

1-Node																							
	MN_{none}^{DI}	MN_{none}^{DS}	MN_{none}^{DIR}	MN_{none}^{DSR}	MN_{none}^{MLB}		MN_{SAL}^{DI}	MN_{SAL}^{DS}	MN_{SAL}^{DIR}	MN_{SAL}^{DSR}	MN_{SAL}^{MLB}		MN_{SAO}^{DI}	MN_{SAO}^{DS}	MN_{SAO}^{DIR}	MN_{SAO}^{DSR}	MN_{SAO}^{MLB}		MN_{SALO}^{DI}	MN_{SALO}^{DS}	MN_{SALO}^{DIR}	MN_{SALO}^{DSR}	MN_{SALO}^{MLB}
KGE_{ss}^{min}	0.62	0.62	0.62	0.60	0.36	KGE_{ss}^{min}							KGE_{ss}^{min}						KGE_{ss}^{min}				
$KGE_{ss}^{5\%}$	0.74	0.72	0.74	0.70	0.41	$KGE_{ss}^{5\%}$							$KGE_{ss}^{5\%}$						$KGE_{ss}^{5\%}$				
$KGE_{ss}^{25\%}$	0.85	0.84	0.85	0.84	0.64	$KGE_{ss}^{25\%}$							$KGE_{ss}^{25\%}$						$KGE_{ss}^{25\%}$				
$KGE_{ss}^{50\%}$	0.90	0.90	0.90	0.90	0.82	$KGE_{ss}^{50\%}$							$KGE_{ss}^{50\%}$						$KGE_{ss}^{50\%}$				
$KGE_{ss}^{75\%}$	0.97	0.96	0.97	0.96	0.93	$KGE_{ss}^{75\%}$							$KGE_{ss}^{75\%}$						$KGE_{ss}^{75\%}$				
$KGE_{ss}^{95\%}$	0.99	0.99	0.99	1.00	0.98	$KGE_{ss}^{95\%}$							$KGE_{ss}^{95\%}$						$KGE_{ss}^{95\%}$				
PNs	8	8	9	9	11	PNs							PNs						PNs				
2-Node																							
KGE_{ss}^{min}	0.50	0.61	0.56	0.57	0.62	KGE_{ss}^{min}	0.44	0.63	0.57	0.50	0.63	KGE_{ss}^{min}	0.64	0.60	0.60	0.67	0.60	KGE_{ss}^{min}	0.57	0.60	0.60	0.62	0.66
$KGE_{ss}^{5\%}$	0.58	0.67	0.60	0.62	0.69	$KGE_{ss}^{5\%}$	0.53	0.64	0.64	0.59	0.66	$KGE_{ss}^{5\%}$	0.69	0.66	0.63	0.69	0.70	$KGE_{ss}^{5\%}$	0.61	0.63	0.63	0.68	0.70
$KGE_{ss}^{25\%}$	0.81	0.83	0.84	0.81	0.82	$KGE_{ss}^{25\%}$	0.81	0.82	0.85	0.80	0.81	$KGE_{ss}^{25\%}$	0.84	0.83	0.83	0.84	0.82	$KGE_{ss}^{25\%}$	0.83	0.82	0.83	0.83	0.82
$KGE_{ss}^{50\%}$	0.88	0.90	0.90	0.89	0.90	$KGE_{ss}^{50\%}$	0.89	0.90	0.91	0.87	0.91	$KGE_{ss}^{50\%}$	0.91	0.89	0.90	0.90	0.90	$KGE_{ss}^{50\%}$	0.89	0.90	0.91	0.89	0.91
$KGE_{ss}^{75\%}$	0.95	0.97	0.95	0.96	0.96	$KGE_{ss}^{75\%}$	0.94	0.96	0.96	0.97	0.96	$KGE_{ss}^{75\%}$	0.95	0.96	0.96	0.96	0.96	$KGE_{ss}^{75\%}$	0.95	0.96	0.96	0.96	0.97
$KGE_{ss}^{95\%}$	0.99	0.99	0.99	0.99	0.99	$KGE_{ss}^{95\%}$	0.98	0.99	1.00	0.99	0.99	$KGE_{ss}^{95\%}$	0.99	0.97	1.00	0.99	1.00	$KGE_{ss}^{95\%}$	0.99	0.98	1.00	0.99	0.99
PNs	18	18	18	18	21	PNs	20	20	20	20	23	PNs	20	20	20	20	23	PNs	22	22	22	22	25
3-Node																							
KGE_{ss}^{min}	0.49	0.62	0.56	0.58	0.66	KGE_{ss}^{min}	0.43	0.46	0.53	0.46	0.62	KGE_{ss}^{min}	0.64	0.67	0.54	0.68	0.65	KGE_{ss}^{min}	0.72	0.56	0.71	0.67	0.64
$KGE_{ss}^{5\%}$	0.57	0.69	0.60	0.60	0.69	$KGE_{ss}^{5\%}$	0.53	0.68	0.55	0.51	0.66	$KGE_{ss}^{5\%}$	0.67	0.74	0.62	0.73	0.66	$KGE_{ss}^{5\%}$	0.78	0.68	0.74	0.71	0.76
$KGE_{ss}^{25\%}$	0.81	0.83	0.84	0.81	0.82	$KGE_{ss}^{25\%}$	0.81	0.82	0.79	0.81	0.81	$KGE_{ss}^{25\%}$	0.81	0.85	0.84	0.83	0.80	$KGE_{ss}^{25\%}$	0.85	0.83	0.85	0.83	0.84
$KGE_{ss}^{50\%}$	0.88	0.90	0.90	0.89	0.91	$KGE_{ss}^{50\%}$	0.89	0.92	0.90	0.88	0.89	$KGE_{ss}^{50\%}$	0.89	0.91	0.91	0.93	0.90	$KGE_{ss}^{50\%}$	0.92	0.90	0.91	0.89	0.91
$KGE_{ss}^{75\%}$	0.95	0.97	0.95	0.96	0.96	$KGE_{ss}^{75\%}$	0.94	0.95	0.96	0.96	0.96	$KGE_{ss}^{75\%}$	0.97	0.96	0.95	0.98	0.94	$KGE_{ss}^{75\%}$	0.96	0.95	0.96	0.97	0.95
$KGE_{ss}^{95\%}$	0.99	0.99	0.99	0.99	0.99	$KGE_{ss}^{95\%}$	0.98	0.99	0.99	1.00	1.00	$KGE_{ss}^{95\%}$	0.99	0.99	1.00	1.00	0.98	$KGE_{ss}^{95\%}$	1.00	0.99	0.99	0.99	0.99
PNs	27	27	27	27	31	PNs	33	33	33	33	37	PNs	33	33	33	33	37	PNs	39	39	39	39	43
4-Node																							
KGE_{ss}^{min}	0.57	0.62	0.56	0.57	0.63	KGE_{ss}^{min}	0.50	0.69	0.57	0.43	0.61	KGE_{ss}^{min}	0.63	0.71	0.57	0.69	0.76	KGE_{ss}^{min}	0.67	0.50	0.67	0.72	0.65
$KGE_{ss}^{5\%}$	0.63	0.67	0.61	0.61	0.69	$KGE_{ss}^{5\%}$	0.53	0.72	0.59	0.62	0.71	$KGE_{ss}^{5\%}$	0.65	0.76	0.66	0.71	0.79	$KGE_{ss}^{5\%}$	0.71	0.71	0.71	0.80	0.67
$KGE_{ss}^{25\%}$	0.84	0.83	0.84	0.80	0.83	$KGE_{ss}^{25\%}$	0.83	0.84	0.80	0.83	0.85	$KGE_{ss}^{25\%}$	0.83	0.86	0.84	0.87	0.88	$KGE_{ss}^{25\%}$	0.85	0.85	0.85	0.88	0.85
$KGE_{ss}^{50\%}$	0.89	0.90	0.90	0.89	0.90	$KGE_{ss}^{50\%}$	0.89	0.92	0.90	0.90	0.91	$KGE_{ss}^{50\%}$	0.90	0.93	0.90	0.93	0.92	$KGE_{ss}^{50\%}$	0.92	0.90	0.92	0.93	0.91
$KGE_{ss}^{75\%}$	0.94	0.97	0.95	0.96	0.96	$KGE_{ss}^{75\%}$	0.95	0.94	0.95	0.96	0.98	$KGE_{ss}^{75\%}$	0.94	0.97	0.95	0.97	0.97	$KGE_{ss}^{75\%}$	0.95	0.96	0.95	0.97	0.96
$KGE_{ss}^{95\%}$	0.99	0.99	0.99	0.99	1.00	$KGE_{ss}^{95\%}$	0.98	0.98	1.00	0.99	1.00	$KGE_{ss}^{95\%}$	0.99	0.99	0.98	0.99	0.99	$KGE_{ss}^{95\%}$	0.98	0.99	0.98	0.99	1.00
PNs	36	36	36	36	41	PNs	48	48	48	48	53	PNs	48	48	48	48	53	PNs	60	60	60	60	65
5-Node																							
KGE_{ss}^{min}	0.49	0.62	0.55	0.57	0.59	KGE_{ss}^{min}	0.54	0.64	0.78	0.54	0.68	KGE_{ss}^{min}	0.64	0.65	0.54	0.73	0.75	KGE_{ss}^{min}	0.72	0.80	0.73	0.79	0.69
$KGE_{ss}^{5\%}$	0.57	0.66	0.58	0.61	0.71	$KGE_{ss}^{5\%}$	0.60	0.73	0.79	0.63	0.70	$KGE_{ss}^{5\%}$	0.67	0.69	0.67	0.78	0.77	$KGE_{ss}^{5\%}$	0.74	0.82	0.81	0.81	0.81
$KGE_{ss}^{25\%}$	0.81	0.83	0.82	0.80	0.85	$KGE_{ss}^{25\%}$	0.82	0.82	0.87	0.82	0.82	$KGE_{ss}^{25\%}$	0.83	0.84	0.84	0.87	0.87	$KGE_{ss}^{25\%}$	0.86	0.88	0.88	0.89	0.87
$KGE_{ss}^{50\%}$	0.89	0.90	0.91	0.89	0.92	$KGE_{ss}^{50\%}$	0.89	0.90	0.94	0.87	0.91	$KGE_{ss}^{50\%}$	0.91	0.91	0.90	0.93	0.92	$KGE_{ss}^{50\%}$	0.92	0.93	0.93	0.94	0.91
$KGE_{ss}^{75\%}$	0.95	0.97	0.96	0.96	0.95	$KGE_{ss}^{75\%}$	0.94	0.95	0.97	0.95	0.96	$KGE_{ss}^{75\%}$	0.95	0.96	0.94	0.97	0.98	$KGE_{ss}^{75\%}$	0.96	0.96	0.96	0.98	0.97
$KGE_{ss}^{95\%}$	0.98	0.99	0.99	0.99	1.00	$KGE_{ss}^{95\%}$	0.98	0.98	1.00	0.99	0.99	$KGE_{ss}^{95\%}$	0.99	1.00	0.98	0.99	1.00	$KGE_{ss}^{95\%}$	0.99	0.99	1.00	1.00	0.99
PNs	45	45	45	45	51	PNs	65	65	65	65	71	PNs	65	65	65	65	71	PNs	85	85	85	85	91

Table S3. γ^{KGE} scores for the Single-Layer Mass-Conserving Neural Networks (MNs)

1-Node																							
	MN_{none}^{DI}	MN_{none}^{DS}	MN_{none}^{DIR}	MN_{none}^{DSR}	MN_{none}^{MLB}		MN_{SAL}^{DI}	MN_{SAL}^{DS}	MN_{SAL}^{DIR}	MN_{SAL}^{DSR}	MN_{SAL}^{MLB}		MN_{SAO}^{DI}	MN_{SAO}^{DS}	MN_{SAO}^{DIR}	MN_{SAO}^{DSR}	MN_{SAO}^{MLB}		MN_{SALO}^{DI}	MN_{SALO}^{DS}	MN_{SALO}^{DIR}	MN_{SALO}^{DSR}	MN_{SALO}^{MLB}
KGE_{ss}^{min}	0.71	0.70	0.71	0.69	0.56	KGE_{ss}^{min}						KGE_{ss}^{min}						KGE_{ss}^{min}					
$KGE_{ss}^{5\%}$	0.72	0.71	0.72	0.71	0.69	$KGE_{ss}^{5\%}$						$KGE_{ss}^{5\%}$						$KGE_{ss}^{5\%}$					
$KGE_{ss}^{25\%}$	0.81	0.81	0.81	0.81	0.78	$KGE_{ss}^{25\%}$						$KGE_{ss}^{25\%}$						$KGE_{ss}^{25\%}$					
$KGE_{ss}^{50\%}$	0.85	0.85	0.85	0.85	0.83	$KGE_{ss}^{50\%}$						$KGE_{ss}^{50\%}$						$KGE_{ss}^{50\%}$					
$KGE_{ss}^{75\%}$	0.90	0.90	0.90	0.90	0.90	$KGE_{ss}^{75\%}$						$KGE_{ss}^{75\%}$						$KGE_{ss}^{75\%}$					
$KGE_{ss}^{95\%}$	0.93	0.92	0.93	0.92	0.92	$KGE_{ss}^{95\%}$						$KGE_{ss}^{95\%}$						$KGE_{ss}^{95\%}$					
PNs	8	8	9	9	11	PNs						PNs						PNs					
2-Node																							
KGE_{ss}^{min}	0.75	0.80	0.77	0.78	0.80	KGE_{ss}^{min}	0.75	0.79	0.80	0.79	0.82	KGE_{ss}^{min}	0.79	0.73	0.76	0.75	0.81	KGE_{ss}^{min}	0.70	0.75	0.76	0.77	0.82
$KGE_{ss}^{5\%}$	0.81	0.80	0.82	0.80	0.82	$KGE_{ss}^{5\%}$	0.79	0.80	0.81	0.81	0.83	$KGE_{ss}^{5\%}$	0.83	0.75	0.82	0.79	0.83	$KGE_{ss}^{5\%}$	0.79	0.76	0.81	0.79	0.84
$KGE_{ss}^{25\%}$	0.84	0.84	0.84	0.84	0.85	$KGE_{ss}^{25\%}$	0.85	0.84	0.85	0.85	0.86	$KGE_{ss}^{25\%}$	0.86	0.82	0.84	0.83	0.85	$KGE_{ss}^{25\%}$	0.86	0.83	0.85	0.84	0.87
$KGE_{ss}^{50\%}$	0.87	0.87	0.87	0.87	0.88	$KGE_{ss}^{50\%}$	0.88	0.87	0.87	0.87	0.88	$KGE_{ss}^{50\%}$	0.88	0.87	0.88	0.89	0.88	$KGE_{ss}^{50\%}$	0.89	0.88	0.88	0.89	0.89
$KGE_{ss}^{75\%}$	0.90	0.90	0.91	0.91	0.91	$KGE_{ss}^{75\%}$	0.90	0.91	0.91	0.91	0.91	$KGE_{ss}^{75\%}$	0.92	0.93	0.91	0.93	0.91	$KGE_{ss}^{75\%}$	0.92	0.93	0.92	0.93	0.92
$KGE_{ss}^{95\%}$	0.93	0.93	0.93	0.93	0.93	$KGE_{ss}^{95\%}$	0.93	0.93	0.93	0.93	0.93	$KGE_{ss}^{95\%}$	0.94	0.96	0.94	0.96	0.94	$KGE_{ss}^{95\%}$	0.94	0.96	0.94	0.96	0.94
PNs	18	18	18	18	21	PNs	20	20	20	20	23	PNs	20	20	20	20	23	PNs	22	22	22	22	25
3-Node																							
KGE_{ss}^{min}	0.75	0.78	0.77	0.79	0.76	KGE_{ss}^{min}	0.75	0.79	0.77	0.78	0.76	KGE_{ss}^{min}	0.73	0.82	0.81	0.82	0.73	KGE_{ss}^{min}	0.77	0.78	0.80	0.78	0.78
$KGE_{ss}^{5\%}$	0.82	0.81	0.82	0.81	0.84	$KGE_{ss}^{5\%}$	0.79	0.81	0.82	0.81	0.84	$KGE_{ss}^{5\%}$	0.78	0.85	0.83	0.83	0.84	$KGE_{ss}^{5\%}$	0.82	0.80	0.83	0.82	0.84
$KGE_{ss}^{25\%}$	0.84	0.84	0.85	0.85	0.86	$KGE_{ss}^{25\%}$	0.85	0.85	0.84	0.85	0.86	$KGE_{ss}^{25\%}$	0.85	0.89	0.86	0.88	0.88	$KGE_{ss}^{25\%}$	0.88	0.87	0.87	0.87	0.88
$KGE_{ss}^{50\%}$	0.87	0.87	0.87	0.88	0.89	$KGE_{ss}^{50\%}$	0.88	0.88	0.87	0.88	0.89	$KGE_{ss}^{50\%}$	0.89	0.94	0.89	0.93	0.91	$KGE_{ss}^{50\%}$	0.90	0.92	0.90	0.90	0.93
$KGE_{ss}^{75\%}$	0.90	0.91	0.91	0.91	0.91	$KGE_{ss}^{75\%}$	0.90	0.91	0.91	0.91	0.92	$KGE_{ss}^{75\%}$	0.93	0.96	0.92	0.95	0.94	$KGE_{ss}^{75\%}$	0.93	0.94	0.93	0.93	0.95
$KGE_{ss}^{95\%}$	0.93	0.93	0.93	0.93	0.93	$KGE_{ss}^{95\%}$	0.93	0.93	0.93	0.93	0.93	$KGE_{ss}^{95\%}$	0.95	0.97	0.94	0.98	0.97	$KGE_{ss}^{95\%}$	0.95	0.96	0.95	0.97	0.98
PNs	27	27	27	27	31	PNs	33	33	33	33	37	PNs	33	33	33	33	37	PNs	39	39	39	39	43
4-Node																							
KGE_{ss}^{min}	0.64	0.80	0.77	0.79	0.78	KGE_{ss}^{min}	0.75	0.77	0.78	0.76	0.82	KGE_{ss}^{min}	0.72	0.86	0.79	0.82	0.82	KGE_{ss}^{min}	0.78	0.76	0.78	0.85	0.82
$KGE_{ss}^{5\%}$	0.70	0.81	0.82	0.81	0.84	$KGE_{ss}^{5\%}$	0.79	0.79	0.82	0.80	0.84	$KGE_{ss}^{5\%}$	0.77	0.87	0.82	0.86	0.86	$KGE_{ss}^{5\%}$	0.81	0.79	0.81	0.88	0.86
$KGE_{ss}^{25\%}$	0.82	0.85	0.85	0.85	0.86	$KGE_{ss}^{25\%}$	0.84	0.86	0.85	0.85	0.87	$KGE_{ss}^{25\%}$	0.85	0.90	0.87	0.90	0.91	$KGE_{ss}^{25\%}$	0.87	0.89	0.87	0.92	0.89
$KGE_{ss}^{50\%}$	0.86	0.88	0.87	0.88	0.89	$KGE_{ss}^{50\%}$	0.88	0.89	0.88	0.88	0.89	$KGE_{ss}^{50\%}$	0.90	0.95	0.90	0.94	0.94	$KGE_{ss}^{50\%}$	0.90	0.94	0.90	0.95	0.92
$KGE_{ss}^{75\%}$	0.90	0.91	0.91	0.91	0.92	$KGE_{ss}^{75\%}$	0.90	0.91	0.91	0.91	0.92	$KGE_{ss}^{75\%}$	0.93	0.96	0.93	0.96	0.96	$KGE_{ss}^{75\%}$	0.92	0.95	0.92	0.96	0.94
$KGE_{ss}^{95\%}$	0.93	0.93	0.93	0.93	0.93	$KGE_{ss}^{95\%}$	0.93	0.93	0.93	0.93	0.94	$KGE_{ss}^{95\%}$	0.96	0.98	0.95	0.98	0.98	$KGE_{ss}^{95\%}$	0.94	0.98	0.94	0.98	0.96
PNs	36	36	36	36	41	PNs	48	48	48	48	53	PNs	48	48	48	48	53	PNs	60	60	60	60	65
5-Node																							
KGE_{ss}^{min}	0.75	0.80	0.80	0.79	0.78	KGE_{ss}^{min}	0.77	0.76	0.79	0.79	0.72	KGE_{ss}^{min}	0.71	0.82	0.80	0.85	0.80	KGE_{ss}^{min}	0.72	0.86	0.80	0.88	0.83
$KGE_{ss}^{5\%}$	0.81	0.81	0.83	0.81	0.83	$KGE_{ss}^{5\%}$	0.81	0.81	0.83	0.81	0.83	$KGE_{ss}^{5\%}$	0.77	0.85	0.83	0.86	0.86	$KGE_{ss}^{5\%}$	0.81	0.88	0.85	0.90	0.85
$KGE_{ss}^{25\%}$	0.84	0.85	0.85	0.85	0.86	$KGE_{ss}^{25\%}$	0.84	0.86	0.86	0.85	0.86	$KGE_{ss}^{25\%}$	0.86	0.91	0.88	0.92	0.89	$KGE_{ss}^{25\%}$	0.86	0.92	0.89	0.92	0.91
$KGE_{ss}^{50\%}$	0.87	0.88	0.88	0.88	0.89	$KGE_{ss}^{50\%}$	0.88	0.88	0.89	0.88	0.88	$KGE_{ss}^{50\%}$	0.89	0.95	0.90	0.95	0.94	$KGE_{ss}^{50\%}$	0.90	0.95	0.90	0.95	0.94
$KGE_{ss}^{75\%}$	0.90	0.91	0.91	0.91	0.92	$KGE_{ss}^{75\%}$	0.90	0.92	0.91	0.91	0.91	$KGE_{ss}^{75\%}$	0.93	0.96	0.93	0.96	0.96	$KGE_{ss}^{75\%}$	0.93	0.97	0.93	0.96	0.95
$KGE_{ss}^{95\%}$	0.93	0.93	0.93	0.93	0.94	$KGE_{ss}^{95\%}$	0.93	0.93	0.93	0.93	0.94	$KGE_{ss}^{95\%}$	0.96	0.98	0.96	0.98	0.98	$KGE_{ss}^{95\%}$	0.97	0.98	0.95	0.98	0.97
PNs	45	45	45	45	51	PNs	65	65	65	65	71	PNs	65	65	65	65	71	PNs	85	85	85	85	91

Table S4. KGE_{ss} scores of flow magnitude for the Single-Layer Mass-Conserving Neural Networks (MNs)

1-Node																								
	MN_{none}^{DI}	MN_{none}^{DS}	MN_{none}^{DIR}	MN_{none}^{DSR}	MN_{none}^{MLB}		MN_{SAL}^{DI}	MN_{SAL}^{DS}	MN_{SAL}^{DIR}	MN_{SAL}^{DSR}	MN_{SAL}^{MLB}		MN_{SAO}^{DI}	MN_{SAO}^{DS}	MN_{SAO}^{DIR}	MN_{SAO}^{DSR}	MN_{SAO}^{MLB}		MN_{SALO}^{DI}	MN_{SALO}^{DS}	MN_{SALO}^{DIR}	MN_{SALO}^{DSR}	MN_{SALO}^{MLB}	
1 st group	0.20	0.20	0.19	0.20	0.06	1 st group						1 st group						1 st group						
2 nd group	-1.04	-1.04	-0.99	-0.93	-0.18	2 nd group						2 nd group						2 nd group						
3 rd group	-1.58	-1.58	-1.58	-1.52	-0.79	3 rd group						3 rd group						3 rd group						
4 th group	-0.63	-0.63	-0.66	-0.61	-0.41	4 th group						4 th group						4 th group						
5 th group	0.87	0.87	0.87	0.86	0.83	5 th group						5 th group						5 th group						
2-Node																								
	MN_{none}^{DI}	MN_{none}^{DS}	MN_{none}^{DIR}	MN_{none}^{DSR}	MN_{none}^{MLB}		MN_{SAL}^{DI}	MN_{SAL}^{DS}	MN_{SAL}^{DIR}	MN_{SAL}^{DSR}	MN_{SAL}^{MLB}		MN_{SAO}^{DI}	MN_{SAO}^{DS}	MN_{SAO}^{DIR}	MN_{SAO}^{DSR}	MN_{SAO}^{MLB}		MN_{SALO}^{DI}	MN_{SALO}^{DS}	MN_{SALO}^{DIR}	MN_{SALO}^{DSR}	MN_{SALO}^{MLB}	
1 st group	-0.07	0.02	-0.13	0.17	-0.48	1 st group	-0.04	0.16	0.09	0.18	-0.13	1 st group	0.09	0.11	0.19	0.00	0.03	1 st group	-0.06	0.17	0.18	0.01	-0.11	
2 nd group	-1.55	-1.46	-1.42	-1.11	-2.44	2 nd group	-1.38	-1.13	-0.80	-1.05	-1.99	2 nd group	-1.24	-1.40	-0.94	-1.79	-1.84	2 nd group	-1.39	-1.28	-0.85	-1.62	-2.06	
3 rd group	-1.22	-1.08	-0.96	-1.08	-1.40	3 rd group	-1.14	-1.09	-0.66	-1.04	-1.26	3 rd group	-1.09	-1.38	-1.01	-1.47	-1.29	3 rd group	-1.16	-1.37	-0.99	-1.44	-1.25	
4 th group	-0.36	-0.35	-0.32	-0.43	-0.38	4 th group	-0.34	-0.40	-0.24	-0.42	-0.32	4 th group	-0.28	-0.55	-0.32	-0.50	-0.33	4 th group	-0.27	-0.53	-0.30	-0.48	-0.22	
5 th group	0.87	0.88	0.88	0.88	0.88	5 th group	0.87	0.88	0.88	0.88	0.88	5 th group	0.89	0.90	0.89	0.91	0.89	5 th group	0.89	0.91	0.89	0.91	0.89	
3-Node																								
	MN_{none}^{DI}	MN_{none}^{DS}	MN_{none}^{DIR}	MN_{none}^{DSR}	MN_{none}^{MLB}		MN_{SAL}^{DI}	MN_{SAL}^{DS}	MN_{SAL}^{DIR}	MN_{SAL}^{DSR}	MN_{SAL}^{MLB}		MN_{SAO}^{DI}	MN_{SAO}^{DS}	MN_{SAO}^{DIR}	MN_{SAO}^{DSR}	MN_{SAO}^{MLB}		MN_{SALO}^{DI}	MN_{SALO}^{DS}	MN_{SALO}^{DIR}	MN_{SALO}^{DSR}	MN_{SALO}^{MLB}	
1 st group	-0.07	0.13	-0.12	0.18	-0.94	1 st group	-0.03	0.15	0.09	0.22	-0.45	1 st group	-1.14	-0.20	0.00	-0.65	-1.78	1 st group	-0.42	-0.12	0.13	-0.12	-0.85	
2 nd group	-1.56	-1.33	-1.41	-0.95	-2.55	2 nd group	-1.36	-1.06	-0.99	-1.00	-2.26	2 nd group	-2.29	-1.21	-1.44	-1.51	-2.50	2 nd group	-1.31	-1.18	-1.02	-1.51	-1.98	
3 rd group	-1.22	-1.14	-0.94	-0.98	-1.30	3 rd group	-1.13	-1.02	-0.83	-1.00	-1.25	3 rd group	-1.08	-0.64	-1.07	-0.58	-0.88	3 rd group	-0.66	-0.74	-0.85	-1.11	-1.00	
4 th group	-0.35	-0.40	-0.31	-0.40	-0.27	4 th group	-0.34	-0.36	-0.28	-0.39	-0.27	4 th group	-0.10	-0.01	-0.24	0.03	0.02	4 th group	-0.06	-0.11	-0.18	-0.35	-0.08	
5 th group	0.87	0.88	0.88	0.88	0.89	5 th group	0.87	0.88	0.88	0.88	0.88	5 th group	0.90	0.94	0.90	0.93	0.93	5 th group	0.91	0.91	0.91	0.92	0.94	
4-Node																								
	MN_{none}^{DI}	MN_{none}^{DS}	MN_{none}^{DIR}	MN_{none}^{DSR}	MN_{none}^{MLB}		MN_{SAL}^{DI}	MN_{SAL}^{DS}	MN_{SAL}^{DIR}	MN_{SAL}^{DSR}	MN_{SAL}^{MLB}		MN_{SAO}^{DI}	MN_{SAO}^{DS}	MN_{SAO}^{DIR}	MN_{SAO}^{DSR}	MN_{SAO}^{MLB}		MN_{SALO}^{DI}	MN_{SALO}^{DS}	MN_{SALO}^{DIR}	MN_{SALO}^{DSR}	MN_{SALO}^{MLB}	
1 st group	0.11	0.18	-0.11	0.19	-0.90	1 st group	-0.05	0.09	0.09	0.15	0.09	1 st group	-1.99	-0.20	-0.01	-0.92	-1.20	1 st group	0.02	-0.03	0.02	-0.09	-0.92	
2 nd group	-1.23	-1.05	-1.41	-0.95	-2.55	2 nd group	-1.40	-1.14	-0.98	-1.13	-1.29	2 nd group	-2.61	-1.14	-0.77	-1.27	-1.96	2 nd group	-1.22	-1.62	-1.22	-0.82	-1.99	
3 rd group	-1.59	-0.97	-0.94	-0.97	-1.33	3 rd group	-1.14	-1.04	-0.83	-1.02	-0.98	3 rd group	-1.04	-0.46	-0.51	-0.45	-0.82	3 rd group	-0.89	-1.38	-0.89	-0.44	-0.79	
4 th group	-0.61	-0.36	-0.31	-0.40	-0.25	4 th group	-0.32	-0.36	-0.27	-0.39	-0.24	4 th group	-0.08	0.18	-0.05	0.10	0.03	4 th group	-0.20	-0.30	-0.20	0.11	0.02	
5 th group	0.87	0.88	0.88	0.88	0.88	5 th group	0.87	0.88	0.88	0.88	0.89	5 th group	0.90	0.94	0.91	0.94	0.94	5 th group	0.90	0.92	0.90	0.94	0.93	
5-Node																								
	MN_{none}^{DI}	MN_{none}^{DS}	MN_{none}^{DIR}	MN_{none}^{DSR}	MN_{none}^{MLB}		MN_{SAL}^{DI}	MN_{SAL}^{DS}	MN_{SAL}^{DIR}	MN_{SAL}^{DSR}	MN_{SAL}^{MLB}		MN_{SAO}^{DI}	MN_{SAO}^{DS}	MN_{SAO}^{DIR}	MN_{SAO}^{DSR}	MN_{SAO}^{MLB}		MN_{SALO}^{DI}	MN_{SALO}^{DS}	MN_{SALO}^{DIR}	MN_{SALO}^{DSR}	MN_{SALO}^{MLB}	
1 st group	-0.06	0.15	0.05	0.18	-1.35	1 st group	-0.05	0.15	0.22	0.19	-1.11	1 st group	-1.41	-0.22	0.21	-0.25	-2.16	1 st group	-1.14	0.27	-0.51	-0.55	-1.68	
2 nd group	-1.55	-1.13	-1.29	-0.96	-2.36	2 nd group	-1.35	-1.01	-0.75	-0.95	-2.89	2 nd group	-2.15	-1.08	-0.77	-0.93	-2.33	2 nd group	-2.02	-0.45	-1.13	-1.12	-1.46	
3 rd group	-1.21	-0.97	-0.94	-0.96	-1.18	3 rd group	-1.17	-0.98	-0.65	-0.99	-1.47	3 rd group	-0.97	-0.58	-0.55	-0.41	-0.92	3 rd group	-1.02	-0.30	-0.75	-0.46	-0.57	
4 th group	-0.35	-0.36	-0.27	-0.39	-0.21	4 th group	-0.33	-0.36	-0.15	-0.37	-0.33	4 th group	-0.12	0.16	-0.08	0.16	0.05	4 th group	-0.19	0.24	-0.18	0.11	-0.02	
5 th group	0.87	0.88	0.88	0.88	0.90	5 th group	0.87	0.88	0.89	0.88	0.88	5 th group	0.90	0.94	0.91	0.95	0.94	5 th group	0.91	0.95	0.92	0.95	0.94	

*Note that the 1st group represents the flows within the lowest 20th percentile and the 5th group represents the flows within the highest 20th percentile.

Table S5. α^{KEF} scores of flow magnitude for the Single-Layer Mass-Conserving Neural Networks (MNs)

1-Node																							
	MN_{none}^{DI}	MN_{none}^{DS}	MN_{none}^{DIR}	MN_{none}^{DSR}	MN_{none}^{MLB}		MN_{SAL}^{DI}	MN_{SAL}^{DS}	MN_{SAL}^{DIR}	MN_{SAL}^{DSR}	MN_{SAL}^{MLB}		MN_{SAO}^{DI}	MN_{SAO}^{DS}	MN_{SAO}^{DIR}	MN_{SAO}^{DSR}	MN_{SAO}^{MLB}		MN_{SALO}^{DI}	MN_{SALO}^{DS}	MN_{SALO}^{DIR}	MN_{SALO}^{DSR}	MN_{SALO}^{MLB}
1 st group	1.11	1.11	1.09	1.03	0.50	1 st group						1 st group						1 st group					
2 nd group	3.74	3.74	3.67	3.58	2.27	2 nd group						2 nd group						2 nd group					
3 rd group	4.60	4.60	4.60	4.51	3.43	3 rd group						3 rd group						3 rd group					
4 th group	3.19	3.19	3.24	3.16	2.88	4 th group						4 th group						4 th group					
5 th group	0.96	0.96	0.96	0.94	0.93	5 th group						5 th group						5 th group					
2-Node																							
	MN_{none}^{DI}	MN_{none}^{DS}	MN_{none}^{DIR}	MN_{none}^{DSR}	MN_{none}^{MLB}		MN_{SAL}^{DI}	MN_{SAL}^{DS}	MN_{SAL}^{DIR}	MN_{SAL}^{DSR}	MN_{SAL}^{MLB}		MN_{SAO}^{DI}	MN_{SAO}^{DS}	MN_{SAO}^{DIR}	MN_{SAO}^{DSR}	MN_{SAO}^{MLB}		MN_{SALO}^{DI}	MN_{SALO}^{DS}	MN_{SALO}^{DIR}	MN_{SALO}^{DSR}	MN_{SALO}^{MLB}
1 st group	2.09	1.96	2.23	1.41	2.72	1 st group	2.02	1.48	1.81	1.41	2.00	1 st group	1.68	1.74	1.35	1.94	1.60	1 st group	2.02	1.53	1.31	1.90	1.97
2 nd group	4.53	4.40	4.33	3.87	5.79	2 nd group	4.28	3.91	3.44	3.79	5.15	2 nd group	4.07	4.30	3.62	4.88	4.92	2 nd group	4.29	4.13	3.48	4.63	5.26
3 rd group	4.09	3.89	3.71	3.89	4.34	3 rd group	3.96	3.89	3.29	3.83	4.15	3 rd group	3.90	4.31	3.79	4.43	4.19	3 rd group	4.00	4.30	3.76	4.39	4.13
4 th group	2.80	2.79	2.76	2.92	2.83	4 th group	2.78	2.87	2.65	2.90	2.75	4 th group	2.70	3.07	2.76	3.00	2.77	4 th group	2.68	3.04	2.73	2.97	2.60
5 th group	0.97	0.97	0.99	0.97	0.95	5 th group	0.97	0.97	0.98	0.97	0.95	5 th group	0.98	1.01	0.98	1.01	0.97	5 th group	0.99	1.00	0.98	1.00	0.96
3-Node																							
	MN_{none}^{DI}	MN_{none}^{DS}	MN_{none}^{DIR}	MN_{none}^{DSR}	MN_{none}^{MLB}		MN_{SAL}^{DI}	MN_{SAL}^{DS}	MN_{SAL}^{DIR}	MN_{SAL}^{DSR}	MN_{SAL}^{MLB}		MN_{SAO}^{DI}	MN_{SAO}^{DS}	MN_{SAO}^{DIR}	MN_{SAO}^{DSR}	MN_{SAO}^{MLB}		MN_{SALO}^{DI}	MN_{SALO}^{DS}	MN_{SALO}^{DIR}	MN_{SALO}^{DSR}	MN_{SALO}^{MLB}
1 st group	2.08	1.57	2.22	1.29	3.51	1 st group	2.00	1.55	1.76	1.29	2.68	1 st group	3.91	2.52	1.94	3.22	4.84	1 st group	2.86	2.37	1.53	2.19	3.43
2 nd group	4.54	4.19	4.31	3.63	5.95	2 nd group	4.25	3.81	3.71	3.72	5.54	2 nd group	5.61	4.07	4.37	4.50	5.91	2 nd group	4.19	4.03	3.75	4.48	5.16
3 rd group	4.08	3.96	3.69	3.74	4.20	3 rd group	3.96	3.80	3.52	3.77	4.12	3 rd group	3.87	3.24	3.87	3.16	3.58	3 rd group	3.27	3.40	3.56	3.92	3.76
4 th group	2.80	2.88	2.75	2.88	2.69	4 th group	2.78	2.81	2.70	2.86	2.68	4 th group	2.43	2.28	2.65	2.22	2.25	4 th group	2.37	2.43	2.57	2.79	2.39
5 th group	0.97	0.97	0.99	0.96	0.95	5 th group	0.97	0.97	0.98	0.97	0.95	5 th group	1.05	1.02	0.99	1.05	1.01	5 th group	1.03	1.02	0.99	1.00	1.02
4-Node																							
	MN_{none}^{DI}	MN_{none}^{DS}	MN_{none}^{DIR}	MN_{none}^{DSR}	MN_{none}^{MLB}		MN_{SAL}^{DI}	MN_{SAL}^{DS}	MN_{SAL}^{DIR}	MN_{SAL}^{DSR}	MN_{SAL}^{MLB}		MN_{SAO}^{DI}	MN_{SAO}^{DS}	MN_{SAO}^{DIR}	MN_{SAO}^{DSR}	MN_{SAO}^{MLB}		MN_{SALO}^{DI}	MN_{SALO}^{DS}	MN_{SALO}^{DIR}	MN_{SALO}^{DSR}	MN_{SALO}^{MLB}
1 st group	1.55	1.48	2.20	1.29	3.44	1 st group	2.06	1.72	1.72	1.58	1.40	1 st group	5.17	2.53	2.28	3.64	3.99	1 st group	1.90	2.13	1.90	2.41	3.55
2 nd group	4.04	3.80	4.32	3.64	5.95	2 nd group	4.31	3.93	3.69	3.91	4.13	2 nd group	6.05	3.97	3.42	4.15	5.13	2 nd group	4.05	4.12	4.05	3.49	5.18
3 rd group	4.61	3.73	3.68	3.73	4.24	3 rd group	3.97	3.82	3.54	3.80	3.75	3 rd group	3.80	3.00	3.06	2.96	3.49	3 rd group	3.61	3.51	3.61	2.96	3.47
4 th group	3.17	2.81	2.75	2.87	2.66	4 th group	2.76	2.81	2.69	2.86	2.63	4 th group	2.40	2.03	2.36	2.14	2.23	4 th group	2.59	2.36	2.59	2.11	2.26
5 th group	0.97	0.97	0.99	0.96	0.95	5 th group	0.97	0.97	0.98	0.96	0.97	5 th group	1.04	1.02	1.03	1.04	1.01	5 th group	0.99	1.03	0.99	1.03	0.98
5-Node																							
	MN_{none}^{DI}	MN_{none}^{DS}	MN_{none}^{DIR}	MN_{none}^{DSR}	MN_{none}^{MLB}		MN_{SAL}^{DI}	MN_{SAL}^{DS}	MN_{SAL}^{DIR}	MN_{SAL}^{DSR}	MN_{SAL}^{MLB}		MN_{SAO}^{DI}	MN_{SAO}^{DS}	MN_{SAO}^{DIR}	MN_{SAO}^{DSR}	MN_{SAO}^{MLB}		MN_{SALO}^{DI}	MN_{SALO}^{DS}	MN_{SALO}^{DIR}	MN_{SALO}^{DSR}	MN_{SALO}^{MLB}
1 st group	2.08	1.53	1.87	1.31	4.18	1 st group	2.06	1.49	1.55	1.37	3.78	1 st group	4.34	2.53	1.85	2.61	5.37	1 st group	3.92	1.83	2.96	3.12	4.74
2 nd group	4.51	3.90	4.14	3.65	5.69	2 nd group	4.24	3.73	3.39	3.64	6.45	2 nd group	5.40	3.89	3.43	3.67	5.65	2 nd group	5.22	2.99	3.91	3.92	4.41
3 rd group	4.07	3.73	3.69	3.71	4.02	3 rd group	4.02	3.74	3.27	3.75	4.44	3 rd group	3.71	3.16	3.12	2.92	3.65	3 rd group	3.77	2.76	3.41	2.98	3.14
4 th group	2.79	2.82	2.69	2.86	2.60	4 th group	2.77	2.82	2.51	2.83	2.76	4 th group	2.45	2.06	2.41	2.06	2.20	4 th group	2.55	1.93	2.56	2.14	2.32
5 th group	0.97	0.96	0.98	0.96	0.98	5 th group	0.97	0.96	0.98	0.96	0.94	5 th group	1.05	1.02	1.01	1.03	1.02	5 th group	1.05	1.03	1.03	1.02	1.01

*Note that the 1st group represents the flows within the lowest 20th percentile and the 5th group represents the flows within the highest 20th percentile.

Table S6. β^{KGE} scores of flow magnitude for the Single-Layer Mass-Conserving Neural Networks (MNs)

1-Node																							
	MN_{none}^{DI}	MN_{none}^{DS}	MN_{none}^{DIR}	MN_{none}^{DSR}	MN_{none}^{MLB}		MN_{SAL}^{DI}	MN_{SAL}^{DS}	MN_{SAL}^{DIR}	MN_{SAL}^{DSR}	MN_{SAL}^{MLB}		MN_{SAO}^{DI}	MN_{SAO}^{DS}	MN_{SAO}^{DIR}	MN_{SAO}^{DSR}	MN_{SAO}^{MLB}		MN_{SALO}^{DI}	MN_{SALO}^{DS}	MN_{SALO}^{DIR}	MN_{SALO}^{DSR}	MN_{SALO}^{MLB}
1 st group	0.12	0.12	0.10	0.10	0.03	1 st group						1 st group						1 st group					
2 nd group	0.43	0.43	0.41	0.40	0.19	2 nd group						2 nd group						2 nd group					
3 rd group	0.97	0.97	0.97	0.95	0.62	3 rd group						3 rd group						3 rd group					
4 th group	1.25	1.25	1.27	1.24	0.97	4 th group						4 th group						4 th group					
5 th group	0.98	0.98	0.99	0.96	0.87	5 th group						5 th group						5 th group					
2-Node																							
	MN_{none}^{DI}	MN_{none}^{DS}	MN_{none}^{DIR}	MN_{none}^{DSR}	MN_{none}^{MLB}		MN_{SAL}^{DI}	MN_{SAL}^{DS}	MN_{SAL}^{DIR}	MN_{SAL}^{DSR}	MN_{SAL}^{MLB}		MN_{SAO}^{DI}	MN_{SAO}^{DS}	MN_{SAO}^{DIR}	MN_{SAO}^{DSR}	MN_{SAO}^{MLB}		MN_{SALO}^{DI}	MN_{SALO}^{DS}	MN_{SALO}^{DIR}	MN_{SALO}^{DSR}	MN_{SALO}^{MLB}
1 st group	0.23	0.24	0.26	0.14	0.14	1 st group	0.22	0.16	0.24	0.15	0.08	1 st group	0.17	0.22	0.15	0.20	0.07	1 st group	0.19	0.18	0.13	0.18	0.09
2 nd group	0.60	0.65	0.62	0.51	0.61	2 nd group	0.59	0.53	0.60	0.52	0.54	2 nd group	0.54	0.61	0.50	0.66	0.52	2 nd group	0.56	0.57	0.45	0.62	0.56
3 rd group	1.03	1.06	0.99	0.98	1.05	3 rd group	1.02	1.00	0.99	0.99	1.08	3 rd group	1.00	1.09	0.98	1.14	1.04	3 rd group	1.03	1.08	0.95	1.13	1.10
4 th group	1.24	1.26	1.23	1.25	1.34	4 th group	1.24	1.25	1.22	1.25	1.34	4 th group	1.23	1.32	1.24	1.30	1.31	4 th group	1.24	1.31	1.23	1.30	1.32
5 th group	0.99	0.97	0.99	0.99	1.01	5 th group	0.99	0.99	0.99	0.99	1.01	5 th group	1.00	0.96	1.00	0.96	1.00	5 th group	0.99	0.96	1.00	0.96	1.01
3-Node																							
	MN_{none}^{DI}	MN_{none}^{DS}	MN_{none}^{DIR}	MN_{none}^{DSR}	MN_{none}^{MLB}		MN_{SAL}^{DI}	MN_{SAL}^{DS}	MN_{SAL}^{DIR}	MN_{SAL}^{DSR}	MN_{SAL}^{MLB}		MN_{SAO}^{DI}	MN_{SAO}^{DS}	MN_{SAO}^{DIR}	MN_{SAO}^{DSR}	MN_{SAO}^{MLB}		MN_{SALO}^{DI}	MN_{SALO}^{DS}	MN_{SALO}^{DIR}	MN_{SALO}^{DSR}	MN_{SALO}^{MLB}
1 st group	0.22	0.16	0.26	0.13	0.23	1 st group	0.22	0.18	0.20	0.15	0.14	1 st group	0.56	0.52	0.22	0.61	0.49	1 st group	0.87	0.46	0.16	0.21	0.36
2 nd group	0.60	0.54	0.62	0.47	0.64	2 nd group	0.59	0.55	0.56	0.51	0.59	2 nd group	0.99	0.90	0.60	1.01	1.10	2 nd group	1.00	0.86	0.51	0.67	0.83
3 rd group	1.03	1.00	0.99	0.95	1.02	3 rd group	1.02	1.01	0.98	1.00	1.04	3 rd group	1.19	1.14	0.99	1.19	1.25	3 rd group	1.13	1.19	0.94	1.12	1.20
4 th group	1.24	1.24	1.23	1.24	1.30	4 th group	1.24	1.24	1.23	1.25	1.33	4 th group	1.20	1.17	1.22	1.19	1.25	4 th group	1.15	1.27	1.18	1.26	1.25
5 th group	0.99	0.99	0.99	1.00	1.01	5 th group	0.99	0.99	0.99	0.99	1.01	5 th group	0.95	0.96	0.99	0.96	0.96	5 th group	0.96	0.94	1.00	0.97	0.97
4-Node																							
	MN_{none}^{DI}	MN_{none}^{DS}	MN_{none}^{DIR}	MN_{none}^{DSR}	MN_{none}^{MLB}		MN_{SAL}^{DI}	MN_{SAL}^{DS}	MN_{SAL}^{DIR}	MN_{SAL}^{DSR}	MN_{SAL}^{MLB}		MN_{SAO}^{DI}	MN_{SAO}^{DS}	MN_{SAO}^{DIR}	MN_{SAO}^{DSR}	MN_{SAO}^{MLB}		MN_{SALO}^{DI}	MN_{SALO}^{DS}	MN_{SALO}^{DIR}	MN_{SALO}^{DSR}	MN_{SALO}^{MLB}
1 st group	0.14	0.19	0.26	0.13	0.22	1 st group	0.23	0.18	0.19	0.20	0.07	1 st group	0.88	0.54	0.79	0.75	0.44	1 st group	0.21	0.29	0.21	0.98	0.40
2 nd group	0.46	0.54	0.62	0.48	0.66	2 nd group	0.61	0.56	0.54	0.55	0.43	2 nd group	1.21	0.91	0.95	1.03	0.94	2 nd group	0.59	0.76	0.59	1.01	0.90
3 rd group	1.01	0.99	0.99	0.96	1.05	3 rd group	1.03	1.01	0.97	1.00	0.99	3 rd group	1.24	1.16	1.11	1.12	1.22	3 rd group	0.98	1.18	0.98	1.12	1.16
4 th group	1.28	1.24	1.23	1.24	1.30	4 th group	1.24	1.24	1.23	1.24	1.27	4 th group	1.20	1.17	1.19	1.13	1.23	4 th group	1.18	1.26	1.18	1.13	1.26
5 th group	0.99	0.99	0.99	1.00	1.01	5 th group	0.99	0.99	1.00	0.99	1.01	5 th group	0.94	0.97	0.95	0.96	0.97	5 th group	0.98	0.96	0.98	0.96	0.98
5-Node																							
	MN_{none}^{DI}	MN_{none}^{DS}	MN_{none}^{DIR}	MN_{none}^{DSR}	MN_{none}^{MLB}		MN_{SAL}^{DI}	MN_{SAL}^{DS}	MN_{SAL}^{DIR}	MN_{SAL}^{DSR}	MN_{SAL}^{MLB}		MN_{SAO}^{DI}	MN_{SAO}^{DS}	MN_{SAO}^{DIR}	MN_{SAO}^{DSR}	MN_{SAO}^{MLB}		MN_{SALO}^{DI}	MN_{SALO}^{DS}	MN_{SALO}^{DIR}	MN_{SALO}^{DSR}	MN_{SALO}^{MLB}
1 st group	0.22	0.16	0.24	0.13	0.41	1 st group	0.23	0.15	0.23	0.15	0.25	1 st group	0.82	0.43	0.57	0.74	0.75	1 st group	0.78	0.72	0.84	0.90	0.86
2 nd group	0.60	0.54	0.62	0.48	0.73	2 nd group	0.62	0.50	0.63	0.50	0.68	2 nd group	1.08	0.86	0.83	0.95	0.89	2 nd group	1.04	0.93	0.84	1.03	1.06
3 rd group	1.02	0.99	1.00	0.96	0.98	3 rd group	1.05	0.97	1.04	0.99	1.04	3 rd group	1.15	1.14	1.12	1.11	1.14	3 rd group	1.12	1.13	1.03	1.08	1.11
4 th group	1.24	1.24	1.23	1.24	1.21	4 th group	1.25	1.23	1.21	1.25	1.34	4 th group	1.18	1.19	1.22	1.15	1.23	4 th group	1.17	1.15	1.18	1.12	1.19
5 th group	0.98	0.99	0.98	1.00	1.00	5 th group	0.99	0.99	0.99	0.99	1.01	5 th group	0.94	0.97	0.96	0.97	0.97	5 th group	0.96	0.97	0.97	0.97	0.96

*Note that the 1st group represents the flows within the lowest 20th percentile and the 5th group represents the flows within the highest 20th percentile.

Table S7. r^{KGE} scores of flow magnitude for the Single-Layer Mass-Conserving Neural Networks (MNs)

1-Node																								
	MN_{none}^{DI}	MN_{none}^{DS}	MN_{none}^{DIR}	MN_{none}^{DSR}	MN_{none}^{MLB}		MN_{SAL}^{DI}	MN_{SAL}^{DS}	MN_{SAL}^{DIR}	MN_{SAL}^{DSR}	MN_{SAL}^{MLB}		MN_{SAO}^{DI}	MN_{SAO}^{DS}	MN_{SAO}^{DIR}	MN_{SAO}^{DSR}	MN_{SAO}^{MLB}		MN_{SALO}^{DI}	MN_{SALO}^{DS}	MN_{SALO}^{DIR}	MN_{SALO}^{DSR}	MN_{SALO}^{MLB}	
1 st group	0.29	0.33	0.30	0.31	0.19	1 st group						1 st group						1 st group						
2 nd group	0.32	0.35	0.32	0.35	0.28	2 nd group						2 nd group						2 nd group						
3 rd group	0.40	0.41	0.42	0.42	0.41	3 rd group						3 rd group						3 rd group						
4 th group	0.39	0.41	0.42	0.40	0.44	4 th group						4 th group						4 th group						
5 th group	0.82	0.83	0.83	0.83	0.84	5 th group						5 th group						5 th group						
2-Node																								
	MN_{none}^{DI}	MN_{none}^{DS}	MN_{none}^{DIR}	MN_{none}^{DSR}	MN_{none}^{MLB}		MN_{SAL}^{DI}	MN_{SAL}^{DS}	MN_{SAL}^{DIR}	MN_{SAL}^{DSR}	MN_{SAL}^{MLB}		MN_{SAO}^{DI}	MN_{SAO}^{DS}	MN_{SAO}^{DIR}	MN_{SAO}^{DSR}	MN_{SAO}^{MLB}		MN_{SALO}^{DI}	MN_{SALO}^{DS}	MN_{SALO}^{DIR}	MN_{SALO}^{DSR}	MN_{SALO}^{MLB}	
1 st group	0.29	0.33	0.30	0.31	0.19	1 st group	0.29	0.32	0.35	0.33	0.16	1 st group	0.29	0.34	0.33	0.33	0.18	1 st group	0.35	0.31	0.27	0.29	0.17	
2 nd group	0.32	0.35	0.32	0.35	0.28	2 nd group	0.34	0.36	0.41	0.36	0.34	2 nd group	0.36	0.34	0.38	0.35	0.33	2 nd group	0.35	0.36	0.35	0.37	0.35	
3 rd group	0.40	0.41	0.42	0.42	0.41	3 rd group	0.41	0.42	0.48	0.42	0.43	3 rd group	0.42	0.42	0.44	0.38	0.42	3 rd group	0.41	0.38	0.42	0.45	0.42	
4 th group	0.39	0.41	0.42	0.40	0.44	4 th group	0.40	0.40	0.43	0.40	0.45	4 th group	0.41	0.36	0.42	0.35	0.43	4 th group	0.36	0.36	0.40	0.42	0.46	
5 th group	0.82	0.83	0.83	0.83	0.84	5 th group	0.83	0.83	0.84	0.83	0.84	5 th group	0.85	0.87	0.84	0.88	0.85	5 th group	0.87	0.88	0.85	0.85	0.85	
3-Node																								
	MN_{none}^{DI}	MN_{none}^{DS}	MN_{none}^{DIR}	MN_{none}^{DSR}	MN_{none}^{MLB}		MN_{SAL}^{DI}	MN_{SAL}^{DS}	MN_{SAL}^{DIR}	MN_{SAL}^{DSR}	MN_{SAL}^{MLB}		MN_{SAO}^{DI}	MN_{SAO}^{DS}	MN_{SAO}^{DIR}	MN_{SAO}^{DSR}	MN_{SAO}^{MLB}		MN_{SALO}^{DI}	MN_{SALO}^{DS}	MN_{SALO}^{DIR}	MN_{SALO}^{DSR}	MN_{SALO}^{MLB}	
1 st group	0.29	0.31	0.31	0.31	0.19	1 st group	0.30	0.33	0.32	0.36	0.19	1 st group	0.33	0.43	0.30	0.39	0.34	1 st group	0.42	0.31	0.25	0.27	0.28	
2 nd group	0.32	0.34	0.33	0.36	0.27	2 nd group	0.34	0.37	0.38	0.37	0.31	2 nd group	0.32	0.42	0.34	0.40	0.36	2 nd group	0.42	0.37	0.34	0.36	0.34	
3 rd group	0.40	0.41	0.42	0.44	0.39	3 rd group	0.41	0.43	0.45	0.43	0.42	3 rd group	0.36	0.42	0.41	0.42	0.38	3 rd group	0.47	0.41	0.42	0.45	0.44	
4 th group	0.39	0.40	0.42	0.41	0.46	4 th group	0.40	0.40	0.43	0.41	0.47	4 th group	0.41	0.41	0.43	0.41	0.44	4 th group	0.40	0.37	0.42	0.43	0.40	
5 th group	0.82	0.83	0.84	0.83	0.84	5 th group	0.83	0.84	0.83	0.83	0.85	5 th group	0.88	0.92	0.85	0.92	0.90	5 th group	0.90	0.89	0.89	0.87	0.92	
4-Node																								
	MN_{none}^{DI}	MN_{none}^{DS}	MN_{none}^{DIR}	MN_{none}^{DSR}	MN_{none}^{MLB}		MN_{SAL}^{DI}	MN_{SAL}^{DS}	MN_{SAL}^{DIR}	MN_{SAL}^{DSR}	MN_{SAL}^{MLB}		MN_{SAO}^{DI}	MN_{SAO}^{DS}	MN_{SAO}^{DIR}	MN_{SAO}^{DSR}	MN_{SAO}^{MLB}		MN_{SALO}^{DI}	MN_{SALO}^{DS}	MN_{SALO}^{DIR}	MN_{SALO}^{DSR}	MN_{SALO}^{MLB}	
1 st group	0.26	0.33	0.31	0.31	0.19	1 st group	0.30	0.32	0.31	0.32	0.19	1 st group	0.32	0.42	0.41	0.43	0.36	1 st group	0.30	0.37	0.30	0.30	0.29	
2 nd group	0.32	0.36	0.33	0.36	0.29	2 nd group	0.35	0.36	0.37	0.36	0.36	2 nd group	0.29	0.44	0.40	0.36	0.36	2 nd group	0.32	0.36	0.37	0.37	0.37	
3 rd group	0.40	0.44	0.43	0.44	0.39	3 rd group	0.41	0.43	0.46	0.43	0.48	3 rd group	0.34	0.47	0.46	0.42	0.43	3 rd group	0.41	0.46	0.42	0.42	0.44	
4 th group	0.35	0.41	0.42	0.41	0.47	4 th group	0.40	0.40	0.43	0.40	0.44	4 th group	0.42	0.47	0.44	0.44	0.46	4 th group	0.39	0.44	0.42	0.42	0.50	
5 th group	0.82	0.83	0.84	0.83	0.84	5 th group	0.83	0.84	0.83	0.83	0.85	5 th group	0.88	0.93	0.89	0.93	0.93	5 th group	0.89	0.93	0.86	0.86	0.90	
5-Node																								
	MN_{none}^{DI}	MN_{none}^{DS}	MN_{none}^{DIR}	MN_{none}^{DSR}	MN_{none}^{MLB}		MN_{SAL}^{DI}	MN_{SAL}^{DS}	MN_{SAL}^{DIR}	MN_{SAL}^{DSR}	MN_{SAL}^{MLB}		MN_{SAO}^{DI}	MN_{SAO}^{DS}	MN_{SAO}^{DIR}	MN_{SAO}^{DSR}	MN_{SAO}^{MLB}		MN_{SALO}^{DI}	MN_{SALO}^{DS}	MN_{SALO}^{DIR}	MN_{SALO}^{DSR}	MN_{SALO}^{MLB}	
1 st group	0.29	0.31	0.33	0.31	0.22	1 st group	0.30	0.30	0.44	0.34	0.21	1 st group	0.33	0.43	0.43	0.33	0.08	1 st group	0.43	0.33	0.33	0.43	0.08	
2 nd group	0.32	0.36	0.35	0.37	0.27	2 nd group	0.37	0.36	0.44	0.36	0.24	2 nd group	0.29	0.44	0.44	0.40	0.31	2 nd group	0.44	0.40	0.29	0.44	0.31	
3 rd group	0.40	0.44	0.42	0.44	0.36	3 rd group	0.41	0.43	0.49	0.44	0.39	3 rd group	0.36	0.46	0.48	0.48	0.41	3 rd group	0.46	0.48	0.36	0.48	0.41	
4 th group	0.39	0.41	0.43	0.41	0.46	4 th group	0.40	0.40	0.43	0.41	0.45	4 th group	0.41	0.48	0.45	0.48	0.45	4 th group	0.48	0.48	0.41	0.45	0.45	
5 th group	0.82	0.83	0.83	0.83	0.85	5 th group	0.83	0.84	0.85	0.84	0.85	5 th group	0.88	0.93	0.89	0.93	0.93	5 th group	0.93	0.93	0.88	0.89	0.93	

*Note that the 1st group represents the flows within the lowest 20th percentile and the 5th group represents the flows within the highest 20th percentile.

Table S8. Summary of Multi-Layer Mass-Conserving Neural Network (MN_s) architectural hypothesis in this study

Model Name	Input Distribution Gate	Linear Transformation Layer	Information (Internal State) Sharing	Node Number in Each Layer
$MN_{None}^{DS}(N_1, N_2, N_3)$	Unity	Weight sum to 1.0	No	$(1 \leq N_1 \leq 3; 0 \leq N_2 \leq 3; 0 \leq N_3 \leq 3)$
$MN_{None}^{DSR}(N_1, N_2, N_3)$	Unity	Positive Weight	No	$1 \leq N_1 \leq 3; 0 \leq N_2 \leq 3; 0 \leq N_3 \leq 3$
$MN_{None}^{MLB}(N_1, N_2, N_3)$	Unity	Real values weight & bias	No	$1 \leq N_1 \leq 3; 0 \leq N_2 \leq 3; 0 \leq N_3 \leq 3$
$MN_{SALO}^{DS}(N_1, N_2, N_3)$	Unity	Weight sum to 1.0	Yes	$1 \leq N_1 \leq 3; 0 \leq N_2 \leq 3; 0 \leq N_3 \leq 3$
$MN_{SALO}^{DSR}(N_1, N_2, N_3)$	Unity	Positive Weight	Yes	$1 \leq N_1 \leq 3; 0 \leq N_2 \leq 3; 0 \leq N_3 \leq 3$
$MN_{SALO}^{MLB}(N_1, N_2, N_3)$	Unity	Real values weight & bias	Yes	$1 \leq N_1 \leq 3; 0 \leq N_2 \leq 3; 0 \leq N_3 \leq 3$
$MN_{None}^{DS}(N_1, 0, 0)$	Unity	Weight sum to 1.0	No	$4 \leq N_1 \leq 5$
$MN_{None}^{DSR}(N_1, 0, 0)$	Unity	Positive Weight	No	$4 \leq N_1 \leq 5$
$MN_{None}^{MLB}(N_1, 0, 0)$	Unity	Real values weight & bias	No	$4 \leq N_1 \leq 5$
$MN_{SALO}^{DS}(N_1, 0, 0)$	Unity	Weight sum to 1.0	Yes	$4 \leq N_1 \leq 5$
$MN_{SALO}^{DSR}(N_1, 0, 0)$	Unity	Positive Weight	Yes	$4 \leq N_1 \leq 5$
$MN_{SALO}^{DS-MLB}(N_1, 0, 0)$	Unity	Real values weight & bias	Yes	$4 \leq N_1 \leq 5$

Table S9. Summary of benchmark models used in this study

Model Name	Model Description
<i>LSTM(N₁, 0, 0)</i>	Single-Layer LSTM network with node number N_1 varies from 1 to 6
<i>LSTM(N₁, N₁, 0)</i>	Two-Layer LSTM network with node number N_1 varies from 1 to 5
<i>LSTM(N₁, N₁, N₁)</i>	Three-Layer LSTM network with node number N_1 varies from 1 to 5
<i>MA₃(SAO)</i>	Two Cell-state Single Flow path Mass-Conserving-Architecture with Share Augmented Output gate
<i>MA₄(SAO)</i>	Two Cell-state Two path Mass-Conserving-Architecture with Share Augmented Output gate
<i>MA₅(SAO)</i>	Three Cell-state Two Flow path Mass-Conserving-Architecture with Share Augmented Output gate
<i>MA₆(SAO)</i>	Three Cell-state Three Flow path Mass-Conserving-Architecture with Share Augmented Output gate

Table S10. KGE_{SS} Statistics and Numbers of Parameter for the benchmark LSTM network used in this study

Model Names	$LSTM(1)$	$LSTM(2)$	$LSTM(3)$	$LSTM(4)$	$LSTM(5)$	$LSTM(6)$	$LSTM(1,1,0)$	$LSTM(2,2,0)$
KGE_{SS}^{min}	0.41	0.68	0.66	0.69	0.66	0.55	0.64	0.70
$KGE_{SS}^{5\%}$	0.46	0.72	0.75	0.76	0.78	0.68	0.72	0.75
$KGE_{SS}^{25\%}$	0.74	0.83	0.84	0.84	0.85	0.81	0.84	0.86
KGE_{SS}^{median}	0.77	0.87	0.88	0.89	0.90	0.86	0.89	0.90
$KGE_{SS}^{75\%}$	0.84	0.92	0.93	0.93	0.93	0.91	0.92	0.94
$KGE_{SS}^{95\%}$	0.91	0.95	0.96	0.96	0.98	0.95	0.96	0.96
Par no.	16	43	76	117	166	223	32	83
Model Names	$LSTM(3,3,0)$	$LSTM(4,4,0)$	$LSTM(5,5,0)$	$LSTM(1,1,1)$	$LSTM(2,2,2)$	$LSTM(3,3,3)$	$LSTM(4,4,4)$	$LSTM(5,5,5)$
KGE_{SS}^{min}	0.76	0.71	0.66	0.70	0.62	0.62	0.59	0.73
$KGE_{SS}^{5\%}$	0.76	0.72	0.66	0.72	0.67	0.69	0.66	0.78
$KGE_{SS}^{25\%}$	0.83	0.82	0.80	0.82	0.82	0.82	0.87	0.88
KGE_{SS}^{median}	0.88	0.90	0.84	0.89	0.89	0.90	0.91	0.92
$KGE_{SS}^{75\%}$	0.93	0.94	0.90	0.92	0.92	0.93	0.93	0.95
$KGE_{SS}^{95\%}$	0.95	0.96	0.95	0.95	0.95	0.97	0.97	0.96
Par no.	148	229	326	48	123	220	341	486

Table S11. Summary of the pruned network models in this study

Model Name	Model Description
$MN_{None}^{DS}(5) - D1(P)$	Pruned (one flow path) four-cell-state case to its parent Un-Pruned five-cell-state $MN_{None}^{DS}(5)$
$MN_{None}^{DS}(5) - D2(P)$	Pruned (two flow path) three-cell-state case to its parent Un-Pruned five-cell-state $MN_{None}^{DS}(5)$
$MN_{None}^{DS}(5) - D3(P)$	Pruned (three flow path) two-cell-state case to its parent Un-Pruned five-cell-state $MN_{None}^{DS}(5)$
$MN_{None}^{DS}(5) - D4(P)$	Pruned (four flow path) one-cell-state case to its parent Un-Pruned five-cell-state $MN_{None}^{DS}(5)$
$MN_{SALO}^{DS}(5) - D1(P)$	Pruned (one flow path) four-cell-state case to its parent Un-Pruned five-cell-state $MN_{SALO}^{DS}(5)$
$MN_{SALO}^{DS}(5) - D2(P)$	Pruned (two flow path) three-cell-state case to its parent Un-Pruned five-cell-state $MN_{SALO}^{DS}(5)$
$MN_{SALO}^{DS}(5) - D3(P)$	Pruned (three flow path) two-cell-state case to its parent Un-Pruned five-cell-state $MN_{SALO}^{DS}(5)$
$MN_{SALO}^{DS}(5) - D4(P)$	Pruned (four flow path) one-cell-state case to its parent Un-Pruned five-cell-state $MN_{SALO}^{DS}(5)$
$MN_{SALO}^{DS}(5) - D1(F)$	Pruned (one flow path) four-cell-state case to its parent Un-Pruned five-cell-state $MN_{SALO}^{DS}(5)$ (Full removal of shared information)
$MN_{SALO}^{DS}(5) - D2(F)$	Pruned (two flow path) four-cell-state case to its parent Un-Pruned five-cell-state $MN_{SALO}^{DS}(5)$ (Full removal of shared information)
$MN_{SALO}^{DS}(5) - D3(F)$	Pruned (three flow path) four-cell-state case to its parent Un-Pruned five-cell-state $MN_{SALO}^{DS}(5)$ (Full removal of shared information)
$MN_{SALO}^{DS}(5) - D3(F)$	Pruned (four flow path) four-cell-state case to its parent "un-pruned" five-cell-state $MN_{SALO}^{DS}(5)$ (Full removal of shared information)



Figure S1: Comparison of selected single-layer Mass-Conserving Network performance using hydrographs in log-scale for selected dry, median, and wet years in subplots (a) to (c).

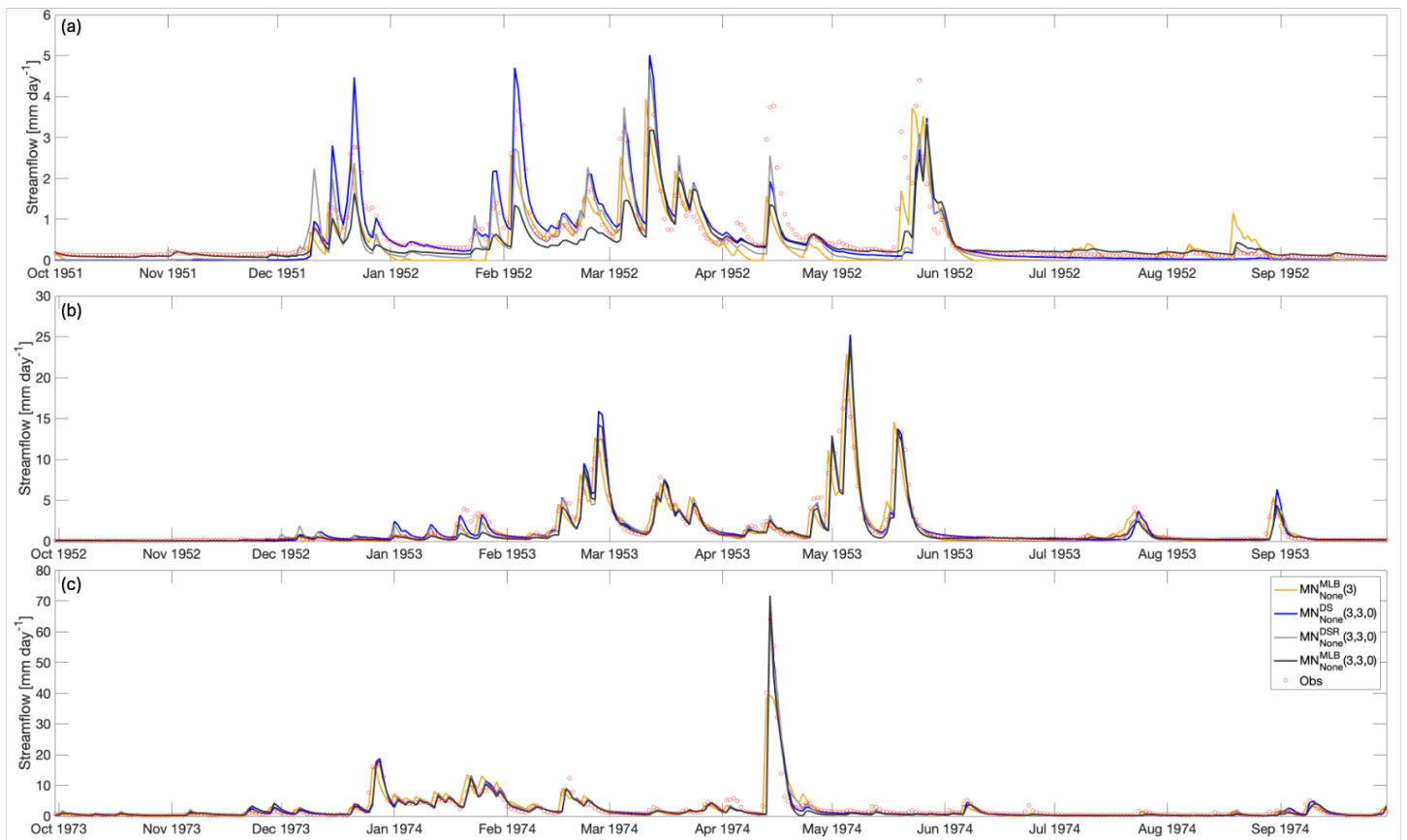


Figure S2: Comparison of selected single-layer Mass-Conserving Network performance using the hydrographs for selected dry, median, and wet years in subplots (a) to (c).

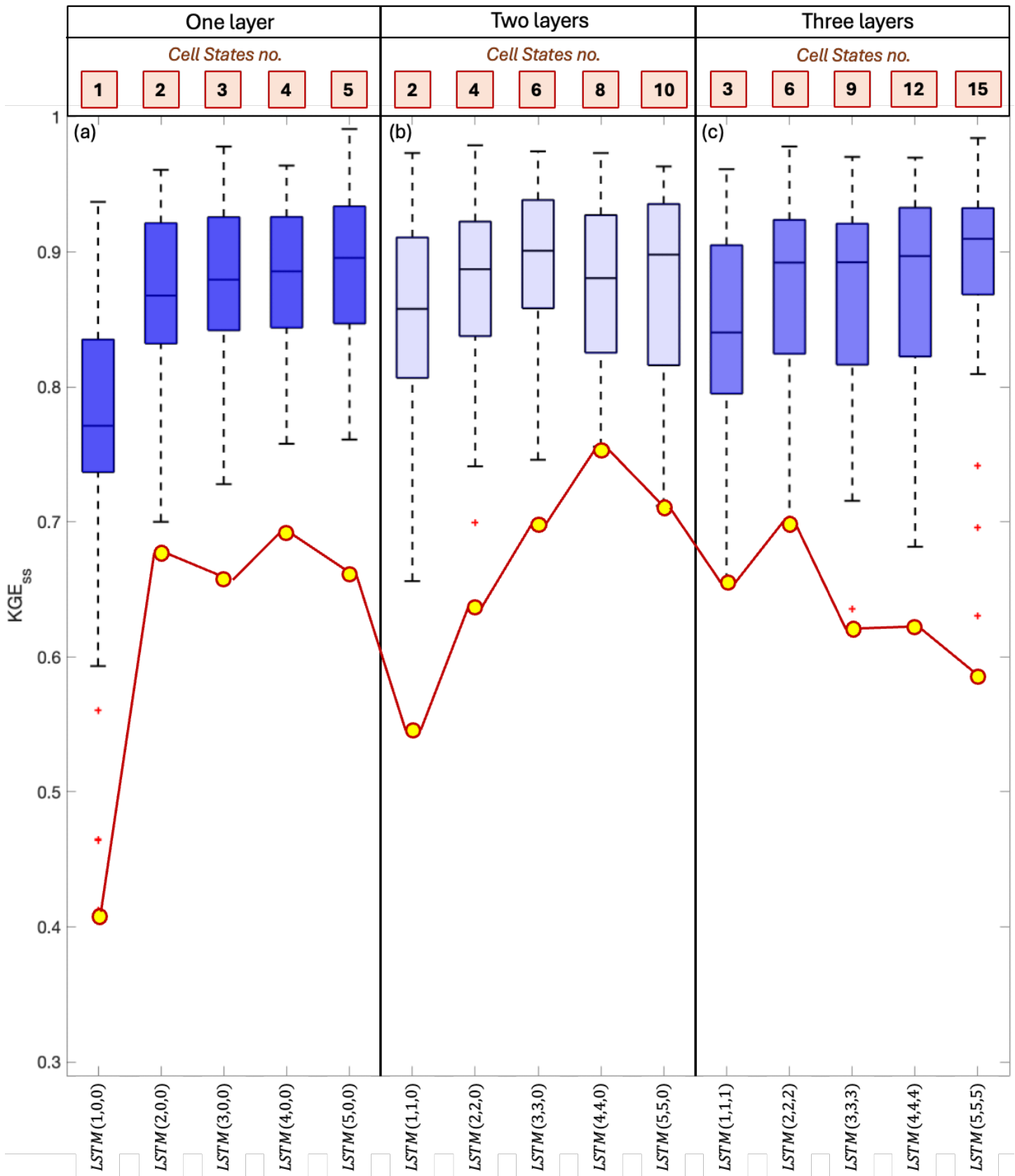


Figure S3: Box and whisker plots of the distributions of annual KGE scores, comparing the (a) 1-layer, (b) 2-layer, and (c) 3-layer long short-term memory (LSTM) networks, with the number of nodes varying from 1 to 5.

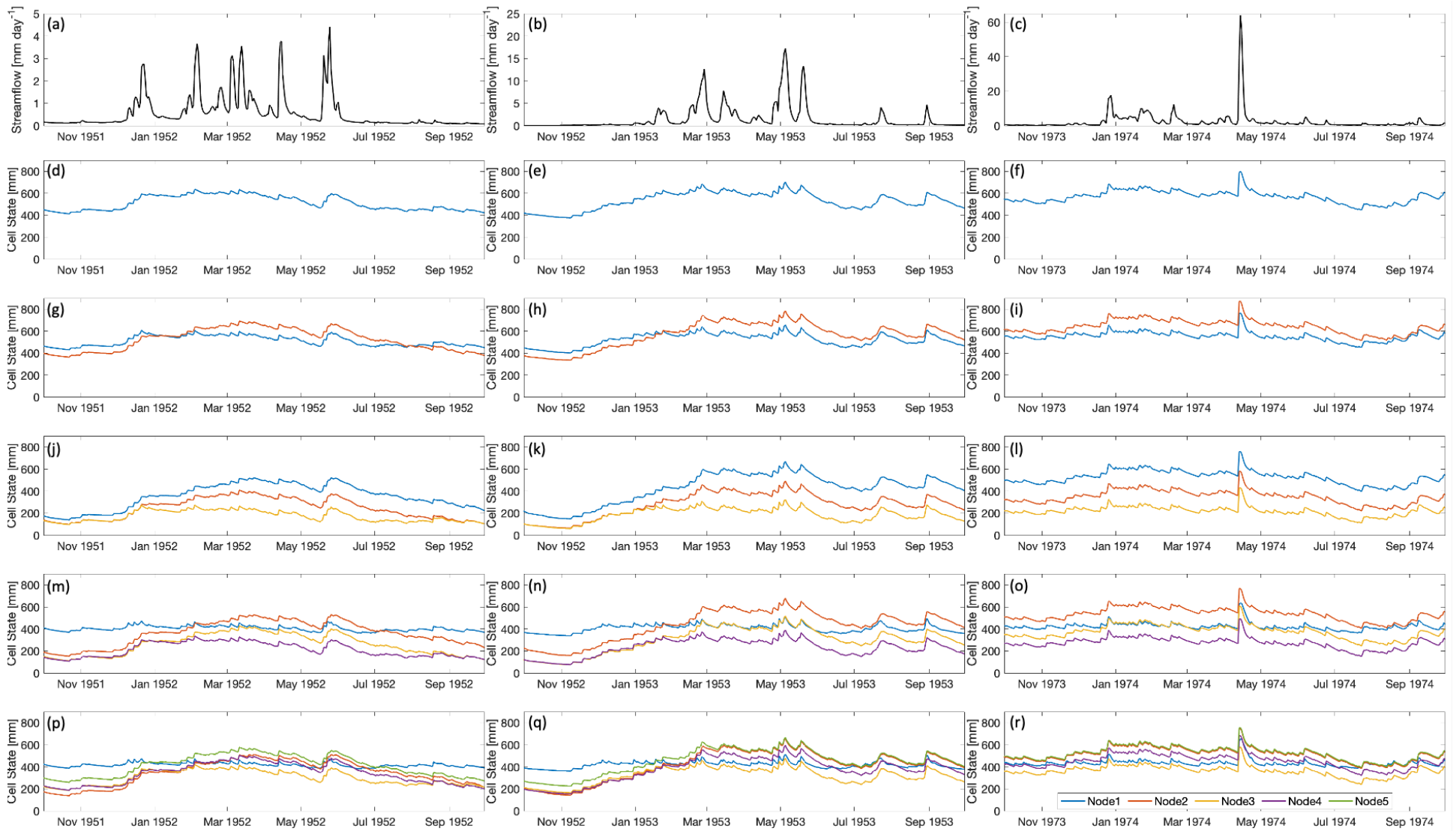


Figure S4: Time series plots of streamflow observations for dry, median, and wet years are shown in subplots (a) to (c). The cell states for the distributed case (DS) are presented with 1-node in subplots (d) to (f) (dry, median, and wet years), 2-node in subplots (g) to (i), 3-node in subplots (j) to (l), 4-node in subplots (m) to (o), and 5-node in subplots (p) to (r).

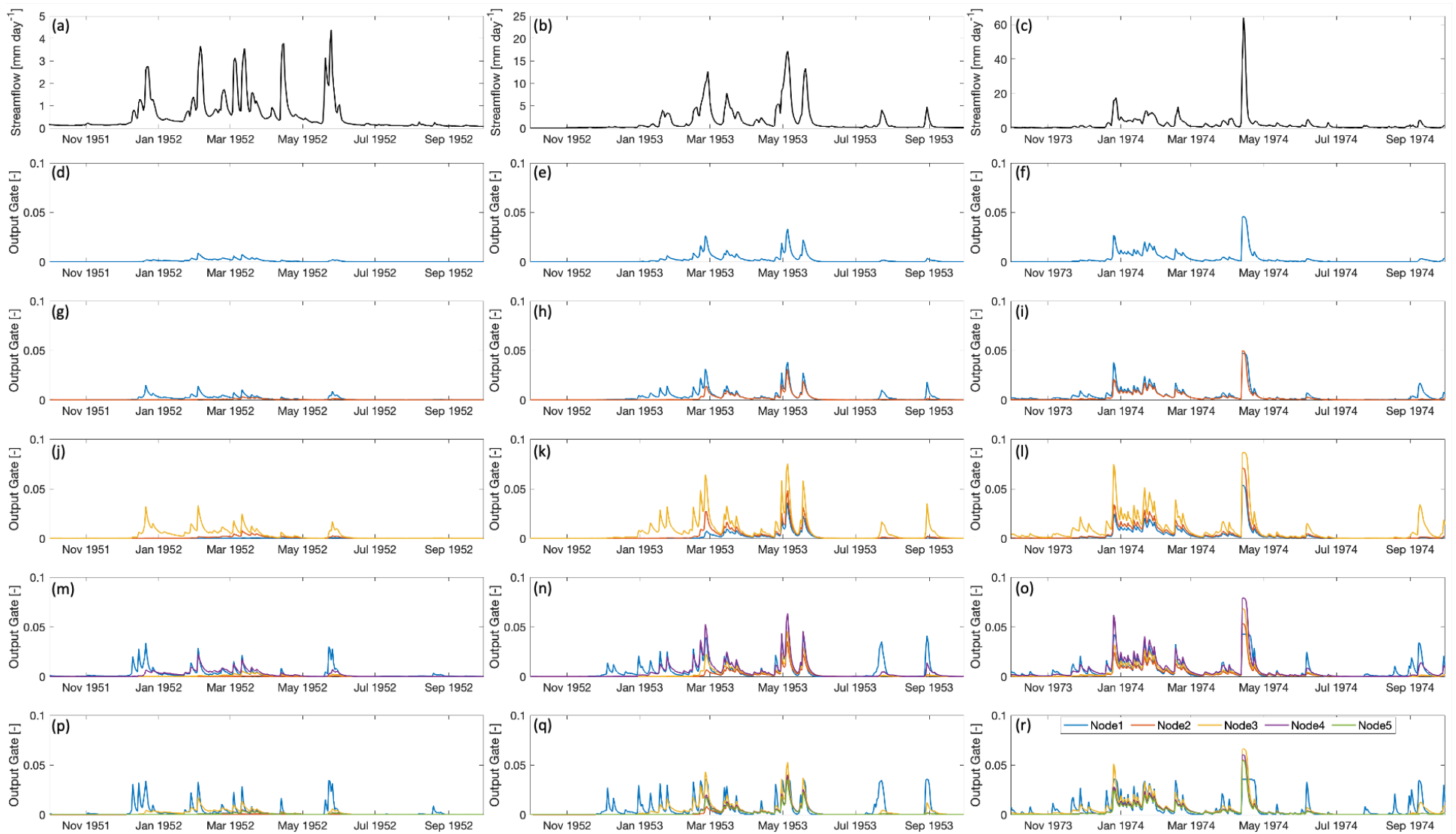


Figure S5: Time series plots of streamflow observations for dry, median, and wet years are shown in subplots (a) to (c). The output gate series for the distributed case (DS) are presented with 1-node in subplots (d) to (f) (dry, median, and wet years), 2-node in subplots (g) to (i), 3-node in subplots (j) to (l), 4-node in subplots (m) to (o), and 5-node in subplots (p) to (r).

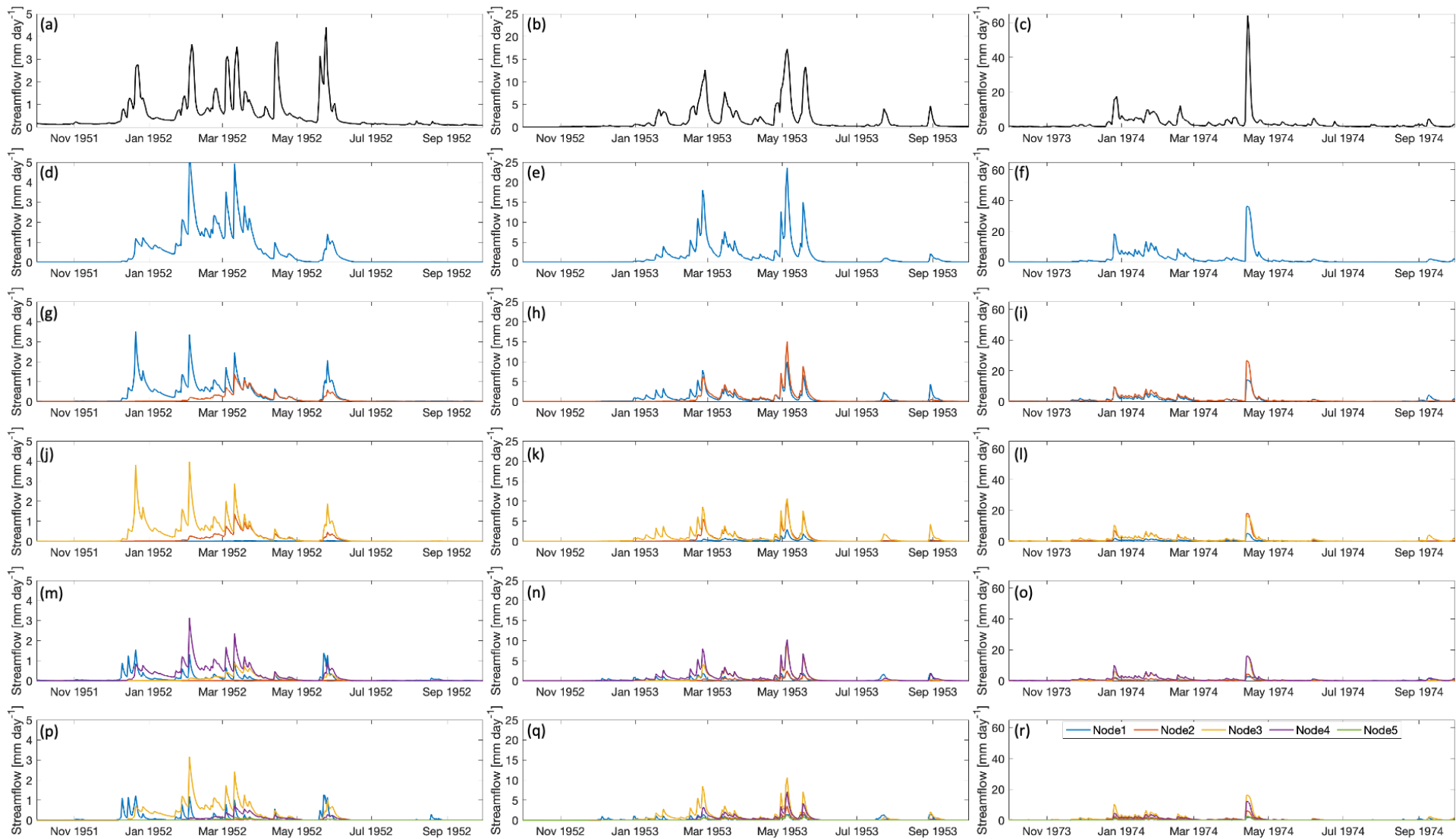


Figure S6: Time series plots of streamflow observations for dry, median, and wet years are shown in subplots (a) to (c). The streamflow components for the distributed case (DS) are presented with 1-node in subplots (d) to (f) (dry, median, and wet years), 2-node in subplots (g) to (i), 3-node in subplots (j) to (l), 4-node in subplots (m) to (o), and 5-node in subplots (p) to (r).

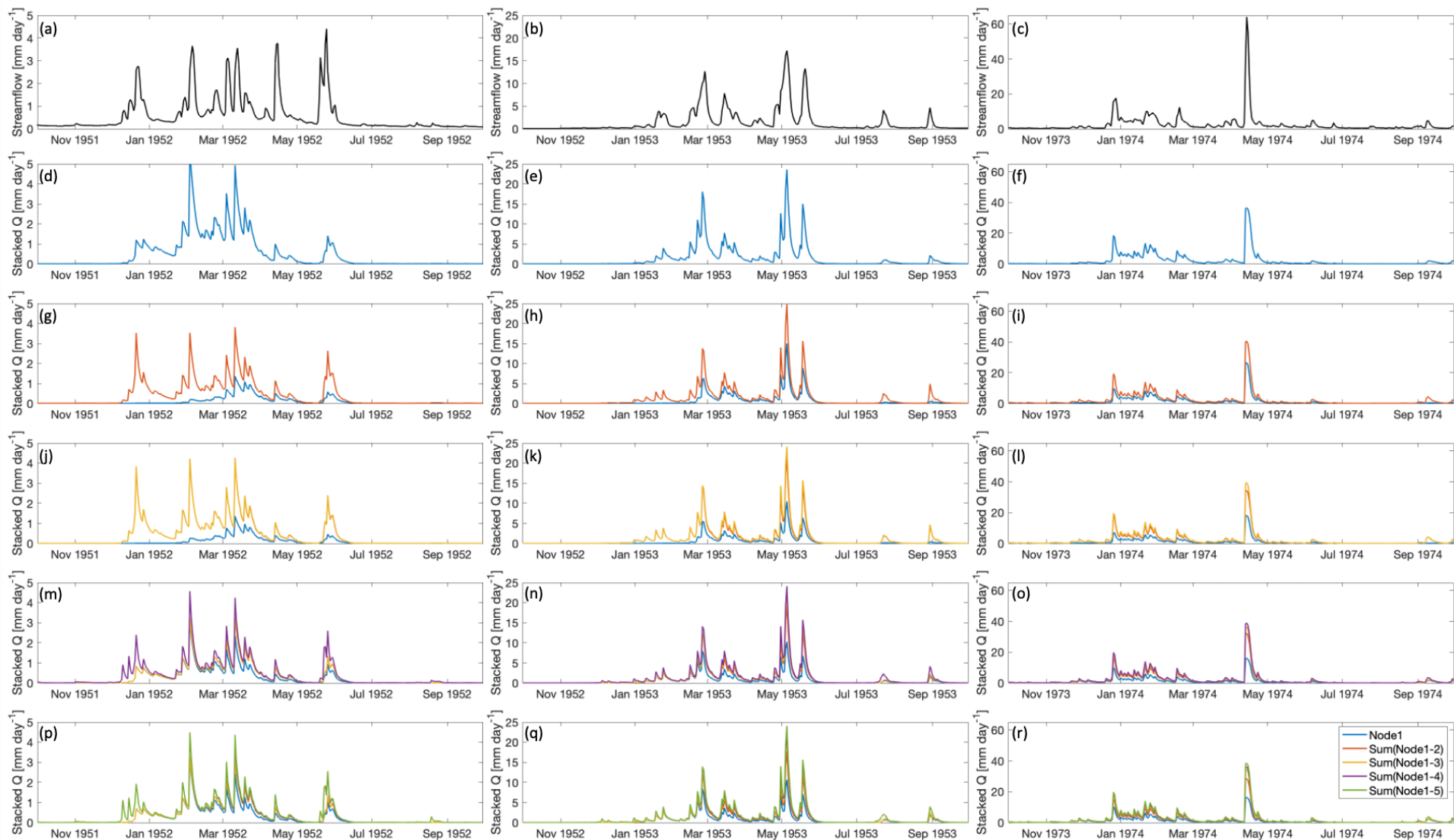


Figure S7: Time series plots of streamflow observations for dry, median, and wet years are shown in subplots (a) to (c). The cumulative streamflow components for the distributed case (DS) are presented with 1-node in subplots (d) to (f) (dry, median, and wet years), 2-node in subplots (g) to (i), 3-node in subplots (j) to (l), 4-node in subplots (m) to (o), and 5-node in subplots (p) to (r). Q=streamflow

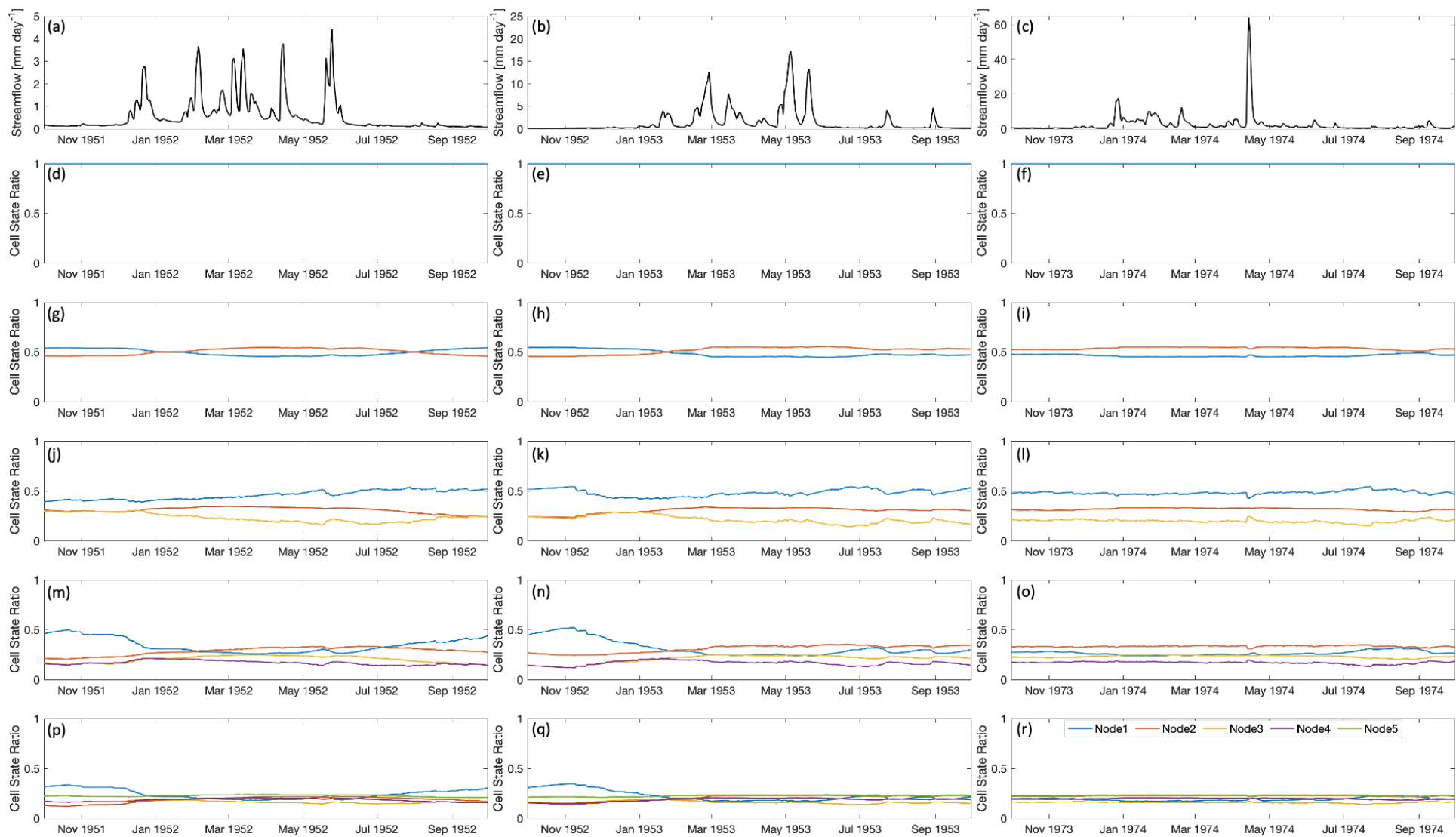


Figure S8: Time series plots of streamflow observations for dry, median, and wet years are shown in subplots (a) to (c). The cell states ratio for the distributed case (DS) are presented with 1-node in subplots (d) to (f) (dry, median, and wet years), 2-node in subplots (g) to (i), 3-node in subplots (j) to (l), 4-node in subplots (m) to (o), and 5-node in subplots (p) to (r).

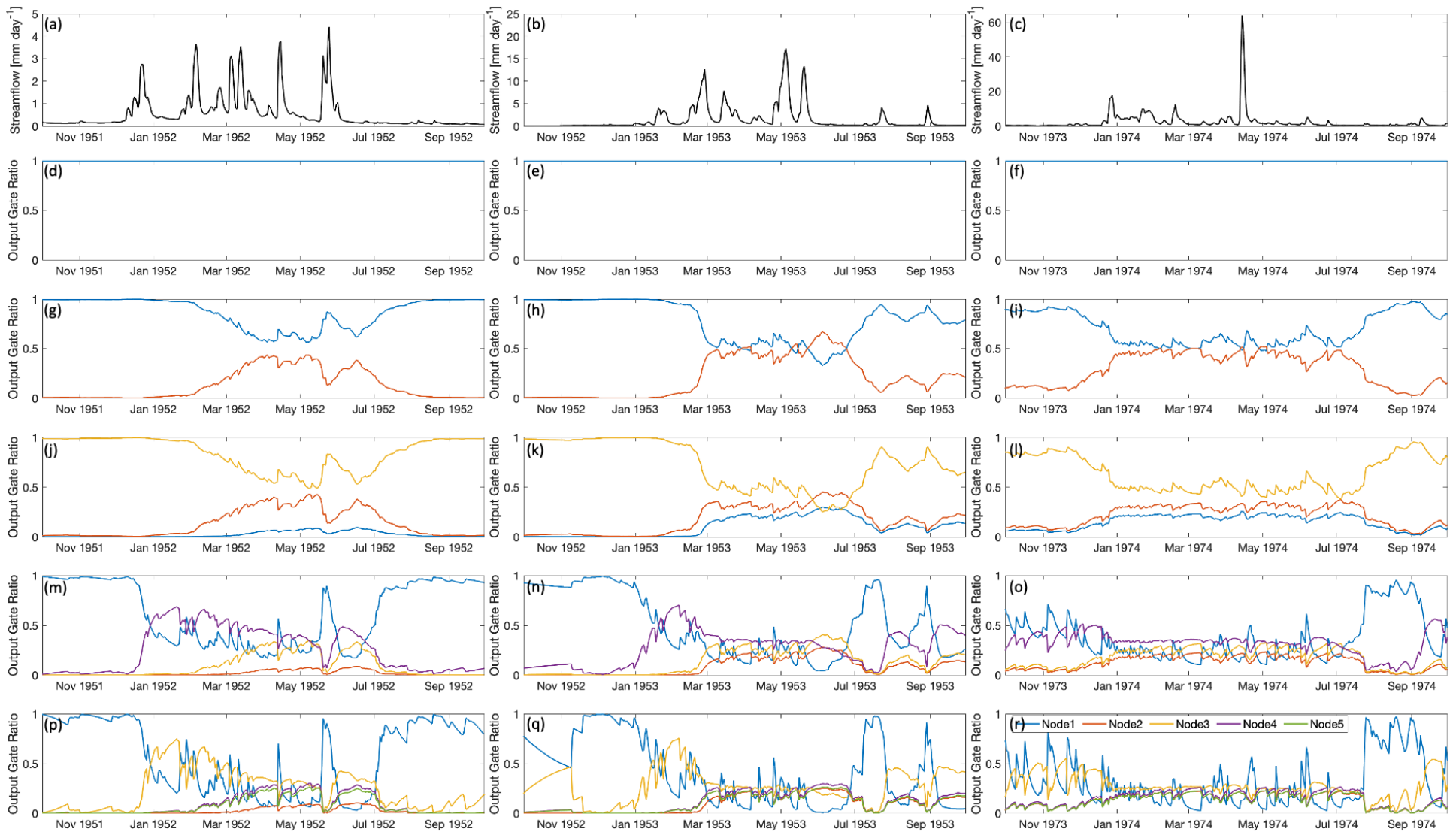


Figure S9: Time series plots of streamflow observations for dry, median, and wet years are shown in subplots (a) to (c). The ratio of output gate series for the distributed case (DS) are presented with 1-node in subplots (d) to (f) (dry, median, and wet years), 2-node in subplots (g) to (i), 3-node in subplots (j) to (l), 4-node in subplots (m) to (o), and 5-node in subplots (p) to (r).

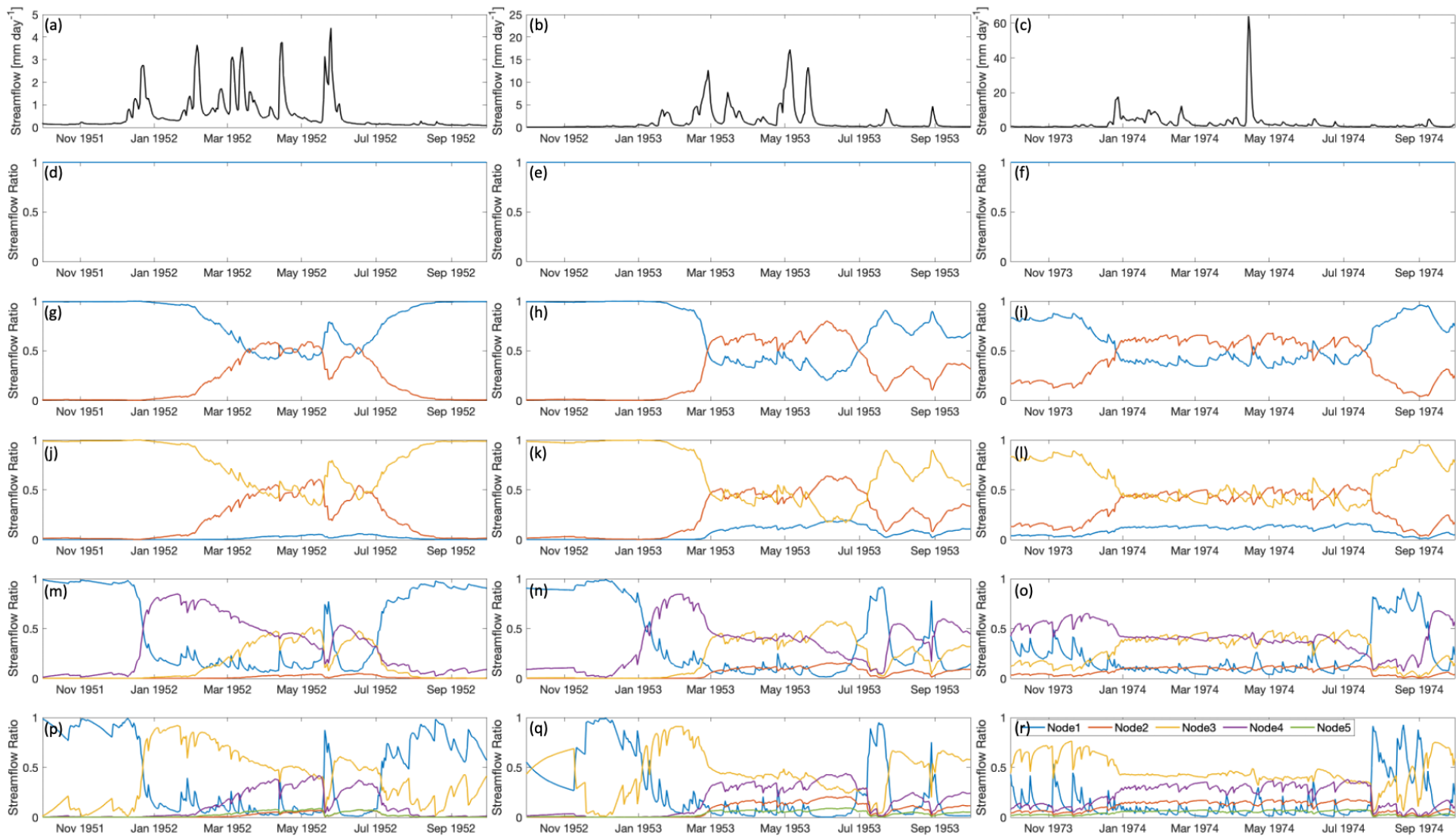


Figure S10: Time series plots of streamflow observations for dry, median, and wet years are shown in subplots (a) to (c). The ratio of streamflow components for the distributed case (DS) are presented with 1-node in subplots (d) to (f) (dry, median, and wet years), 2-node in subplots (g) to (i), 3-node in subplots (j) to (l), 4-node in subplots (m) to (o), and 5-node in subplots (p) to (r).

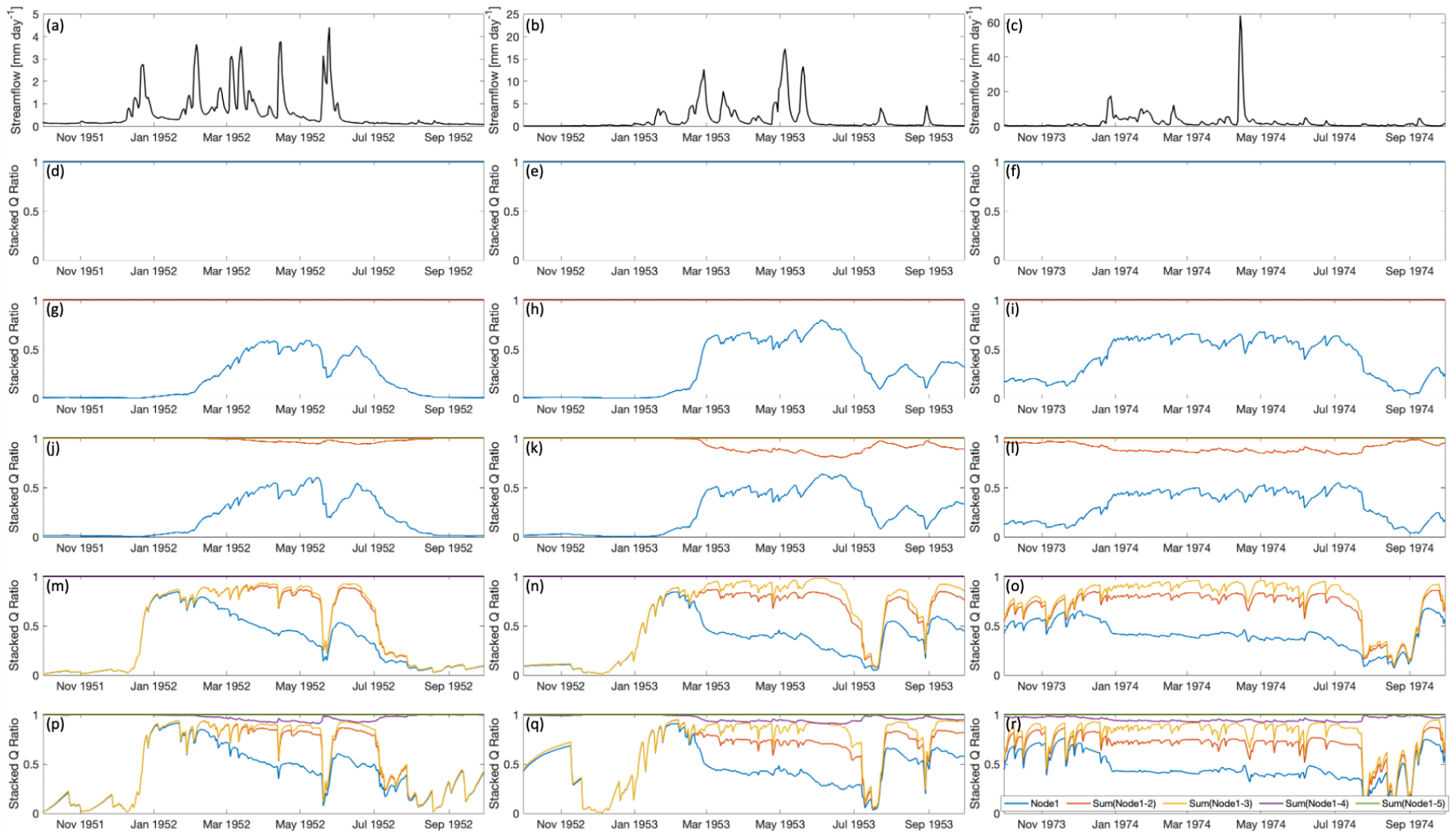


Figure S11: Time series plots of streamflow observations for dry, median, and wet years are shown in subplots (a) to (c). The ratio of cumulative streamflow components for the distributed case (DS) are presented with 1-node in subplots (d) to (f) (dry, median, and wet years), 2-node in subplots (g) to (i), 3-node in subplots (j) to (l), 4-node in subplots (m) to (o), and 5-node in subplots (p) to (r). Q=streamflow